UNIVERSITÀ DEGLI STUDI DI MILANO

DEPARTMENT OF PHYSICS

PHD SCHOOL IN
PHYSICS, ASTROPHYSICS AND APPLIED PHYSICS
CYCLE XXXIII

KINETICS OF NUCLEIC ACIDS HYBRIDIZATION AND OF COMPLEX DNA STRUCTURES FORMATION ON A BIOSENSING SURFACE

Disciplinary Scientific Sector FIS/07

PhD Thesis of:
Luka Vanjur

Director of the School: Prof. Matteo Paris
Supervisor of the Thesis: Prof. Marco Buscaglia

A.Y. 2020-2021

This page intentionally left blank.

Abstract

Use of DNA-based molecular probes on a biosensing surface enables unprecedented designs, with finely tuned responsive structures. Furthermore, cost and production of DNA, in addition to its overall ability to interact with various biological molecules, make DNA the ideal candidate for biosensing surface functionalization. However, all DNA based biosensing relies at some point on the pairing of to single stranded DNA molecules, namely DNA hybridization. I utilized a label-free, optical, multiplexed, biosensing platform to study probing capabilities of surface grafted DNA, from simple short sequences to highly ordered complex nanostructures. My PhD research started with the study of kinetics of simple oligo hybridization on surface. DNA hybridization on surface is usually treated under the well established Langmuir model, used to treat majority of surface adsorbtion phenomena. However, electrostatics of DNA phosphate backbone in addition to high denstiy of DNA monolayer on sensing surface, prevents this model to be applied in all it's potency. We observed strong suppression in binding kinetics even at concentrations below the K_D. Moreover, this suppression correlated positively with DNA probe density, indicating a possible electrostatic influence. Based on the electrostatic theory of DNA monolayers I developed a simple model accounting for the electrostatic penalty associated with entry of DNA molecule into charged DNA monolayer. Moreover, in addition to electrostatic repulsion hampering, steric effects arising from such high density areas also affect the overall sensitivity and rapidity of surface nucleic acids sensing with DNA. We proposed different strategies to combat this obstacles, including varying salt concentrations to counter electrostatic repulsion, grafting DNA probes on hydrogel, effectively reducing charge density. Use of multiple strands was also proposed considering the observed high affinity towards DNA hybridization to partially double stranded probes, that provide further stacking stabilization, and decrease the dissociation events. DNA as a sensing probe was also successfully utilized in sensing micro-RNA (miRNA), a widely acknowledged and used biomarker for early-disease diagnostics. MiRNA molecules, like any other RNA molecule, readily hybridizes with DNA, forming a RNA/DNA hybrid, however, miRNAs specifically are very scarcely and non-uniformly distributed in sera, blood and tissue, this inhibits the availability of miRNAs, despite their potential as biomarkers. We grafted various DNA strands with complementary sequences to 5 different known miRNAs. Our multiplexed assay was able to detect as low as 0.5 pM miRNA while yielding 30x fold mass amplification 90 minutes after the sample injection. Amplification was achieved by a specific antibody (Ab1) targeting DNA-RNA hybrids, polyclonal secondary antibody (Ab2) targeting primary antibody and careful system optimization. A simple numeric model was developed accounting the formation of DNA/RNA hybrids, Ab1 binding to hybrid and formation of Ab1-Ab2. Last interaction was treated as a competitive system, since the Ab pairs also tend to form in solution as well as on surface. System was optimized for amplification factor while keeping the miRNA concentration and total assay duration fixed. The amplification signal was shown to be sequence dependent, since the kinetics of DNA/RNA hybridization depends on the sequence and predictive models are not available. DNA microarrays are often employed to study the binding and kinetics of various transcription factors. We investigated binding yeast gene regulator Gal4, on spots containing consensus and non-consensus sequence both in the form of simple DNA strand and DNA hairpin structure. Through the experimental observations, we found that the initial binding step is charge mediated and can be therefore fine tuned through ionic conditions. A Two-step nested well model was built, to explain these observations. First encounter is a non-specific interaction, followed by conformational adjustment until the consensus sequence is reached. Finally, potential of DNA to self-assemble into structure with higher complexity and perform specific functions was explored. Hybridization Chain Reaction (HCR) is nowadays well established isothermal reaction based on self-assembly properties of DNA. This nucleic acid triggered isothermal reaction shows great promise in biosensing applications, primarily as a means for enzyme-free signal amplification. We observed the formation of HCR filaments in real time by grafting trigger DNA sequence on surface and releasing interacting hairpins in solution. Observed binding curves were cleary different from simple DNA hybridization, indicating multiple reaction occuring on the surface. We modelled this behaviour similarly to protein-DNA binding. Binding of first hairpin is fast, due to oligo-like hybridization by the hairpin overhang. This recognition step is followed by slow hairpin opening which ends in exposition of overhang, or binding site for second hairpin. Two relaxation model thus accounts for first hairpin binding to trigger strand on surface and to hairpin unzipping. Fluorescence confocal microscopy investigation was performed on HCR spots with dye-conjugated first hairpin. Direct visual comparison with DNA monolayer shows dramatic difference in intensity profile of the spot, which confirms the presence of HCR filaments on surface. In the last part of the thesis work I explored the functionalization of the biosensor surface with large-scale a complex structure enabling control of probes with nanometer precision. Highly ordered DNA origami rectangles were developed and functionalized with sticky ends (tethers) for adsorbtion on DNA grafted surface. Investigation was carried out on the number of 40bp long sticky ends required to bring the structure to the surface, as well the kinetics based on the number of tethers. For this purpose, 2, 4 and 6 legged rectangles were produced, their stability and proper folding was verified directly via AFM. Observations of origami binding revealed: despite the large size and net charge of the origami, rectangles with at least 4 tethers complementary to DNA probes readily bind to the biosensor surface; number of tethers primarily affects the stability through lowering the dissociation rate, which was interpreted as probability of all available tethers being simultaneously detached - which directly correlates with number of tethers.

Contents

List of Figures

List of Tables

Chapter 1

Introduction

In the first chapter I will give a general introduction to the subjects of this thesis. Nucleic acids, DNA and RNA, are discussed first, following with a brief overview of the physical principles governing the structure of DNA. This is followed by an introduction to functional DNA nanotechnology (structural is adressed in Chapter 2). Finally, Chapter 1 ends with an introduction to biosensors, with emphasis on DNA microarrays, largely used throughout this thesis, and Surface Plasmon Resonance due to its similarity with Reflective Phantom Interface, the technique used throughout this thesis.

1.1 Nucleic acids

Nucleic acids, ribonucleic acid (RNA) and deoxyribonucleic acid (DNA), are the central substance of all life on Earth, serving as information carriers and storages for every living cells. Most of this nucleic acids is found in cells; in the case of DNA: condensed in chromosomes in nuclear membrane. Structurally, nucleic acids are biological polymers (biopolymers), made up of four different monomers, called nucleotides. These nucleotides consist of three components: negatively charged phosphate group, five-carbon sugar that define the orientation of the polymer and four distinct nucleobases (or just bases): adenine (A), guanine (G), cytosine (C) and thymine (T) in the case of DNA, or uracil (U) in the case of RNA. Periodical repetitions of these nucleobases are what we call a DNA or RNA sequence. In nature, we find DNA in single-stranded (ssDNA) form and double-stranded (dsDNA) form. In the later case, the DNA molecule consists of two strands wounding around a common axis in antiparallel orientation and are connected through so called base pairs via hydrogen bonding. This process of hydrogen bond formation is called base pairing or hybridization. Furthermore, it is important to notice that this base pairing follows a specific rule, i.e. among four distinct bases, only two[a] different base pairs are allowed, i.e. adenine (A) can only pair with thymine (T) and vice versa, and guanine (G) can only pair with cytosine (C) and vice versa. These rules are known as Watson-Crick rules, and these pairs as Watson-Crick pairs, named for James Watson and Francis Crick who discovered the double helical structure of DNA in 1953 [1]. Figure 1.1 shows the structure of RNA (left) and dsDNA (right), and corresponding bases with colored Watson-Crick pairs. G-C pairs when formed

---

[a] Four if counting symmetric combinations

are held together by three hydrogen bonds, whereas A-T pairs are conncted with two — G-C pairs are stronger, i.e. sequences with higher %CG content are usually more stable. It is estimated that genome consits of $3 \cdot 10^9$ base pairs, organized in 23 chromosomes [2]. This means that every human cell contains $\approx 7 \cdot 10^{10}$ base-pairs of DNA.

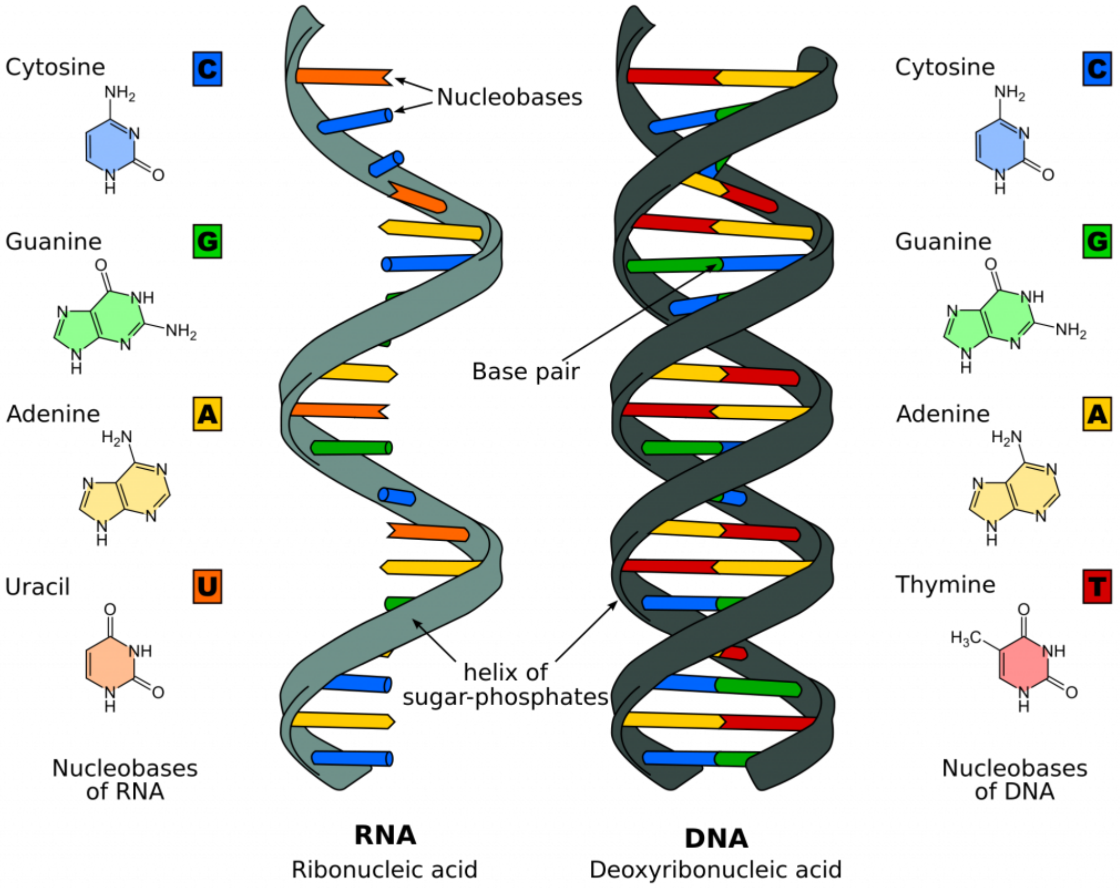

Figure 1.1: Structure of RNA (left) and dsDNA (right). RNA in nature is found in single strand form, in principle it is often folded onto itself in a type of structure called hairpin. This will be discussed later in this chapter. DNA on the other hand, can be found either as a single strand, in which case can also fold onto itself to form a hairpin, or as a stable double stranded helix, like in the picture. Each nucleic acids is shown with it's corresponding bases, notice that Uracil appears only with RNA, whereas for DNA it is replaced by Thymine. Sugar-phosphate backbones are colored in different shade of grey to emphasize the different sugars present in DNA and RNA, deoxyribose and ribose sugar, respectively. Furhermore, base pairs in DNA are connected according to Watson-Crick base pairing rules, i.e. Adenine binds with Thymine to form A-T (or T-A) pairs, and Guanine pairs with Cytosine to form G-C (or C-G) pairs. In the picture above, DNA strands are complete complements, i.e. both sequences are fully compatible with regards to Watson-Crick rules. In fact, for the molecule to fold onto itself, in the case of single strand, it is necessary that the molecule posses a certain degree of self-complementarity. Adopted from: Khan Academy. Accessed October 10, 2020. https://www.khanacademy.org.

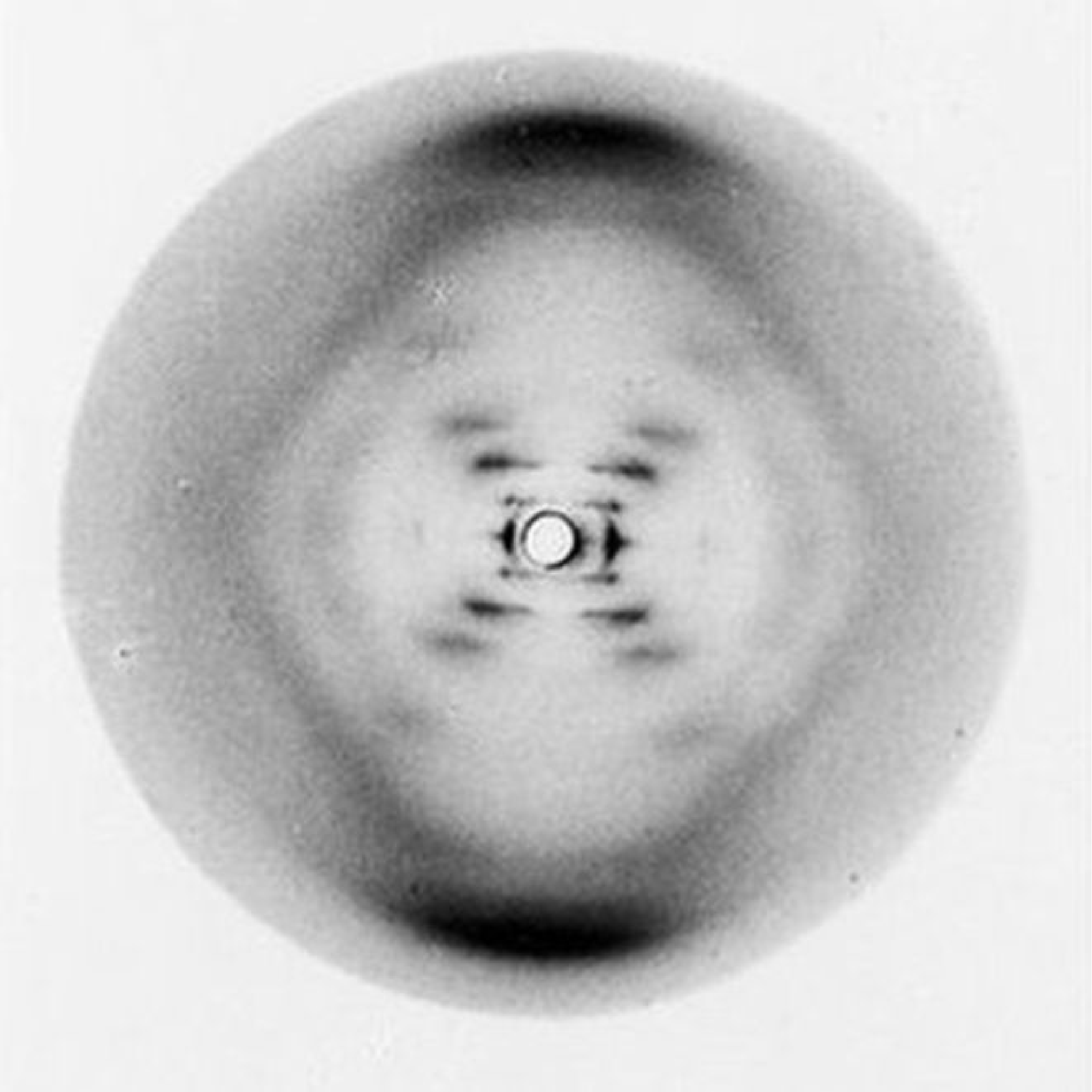

Figure 1.2: Legendary Photo 51, adopted from [3]. X-Ray diffraction pattern of DNA in gel. This image was crucial in deciphering the structure of DNA.

Structure of DNA

Figure 1.3 shows the structure of DNA in more detail. Watson-Crick base pairs are shown with corresponding number of hydrogen bonds. Each base is connected to sugar and phosphate backbone. This particular arrangement of molecules in DNA, the fact the bases are pointing inward, towards each other, while sugar-phosphate backbone is left exposed is the result of hydrophilic nature of these components. Phosphate and sugars, are easily dissolved in water, while bases are not dissolving in pH neutral medium. So, in order to avoid water, the bases orientate themselves inward, towards each other. Furthermore, we know the distance between two adjacent bases equals 6 nm. However, considering the thickness of the bases is 3.3Å, we are left with 2.7Å of space between the bases. In order to avoid the entry of the water molecules in this space, dsDNA is further stabilized by minimizing this distance while keeping the distance between phosphates 6nm. One way to achieve this is by simple tilting of the molecule, however, if the DNA is simply tilted, the atoms in the molecule would collide, so this stabilization is achieved by twisting the molecule, resulting in famous helical structure, where bases are now 3.3 Å apart, and protected from water, and phosphates are 6 nm from each other vertically and 18Å apart in plane. Furthermore, angle between two neighbouring phosphates can be calculated to be 32.3°, i.e. the molecule makes a full turn every 360° / 32.3° = 11 bases.

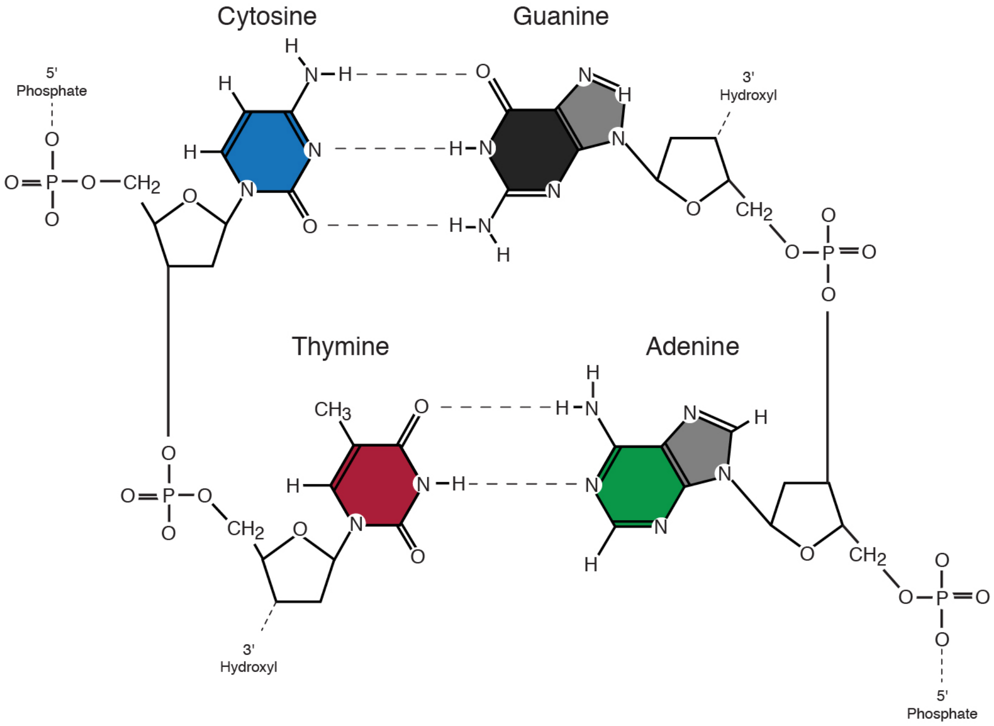

Figure 1.3: Watson-Crick base pairs and sugar-phosphate backbone.

1.2 DNA nanotechnology

Because of the unique selectivity the ssDNA has toward it's complementary sequence, and reliable programmability, DNA molecules are largely investigated as a nanotechnological tool. In particular, there are two main goal defined branches of DNA nanotechnology:

- Structural DNA nanotechnology - building complex nanoscale, bioresponsive objects with high degree of precision and functionalization potential
- Functional DNA nanotechnology - fine control of spatial and temporal structure of matter; design of biomimetic nanoscale machines that perform predictable and tunable actions

Indeed, DNA is an ideal candidate for the listed objectives. Whole story started with the realization of immobile Holliday junctions by Ned Seeman in his breakthrough paper from 1982 [4]. Holliday junction is realized by two dsDNA molecules with mutually complementary subdomains, Figure 1.4. In fact, Seeman's motivation for this was the assembly of protein holding cage that could be used in X-ray crystallography, for determining the protein structure.

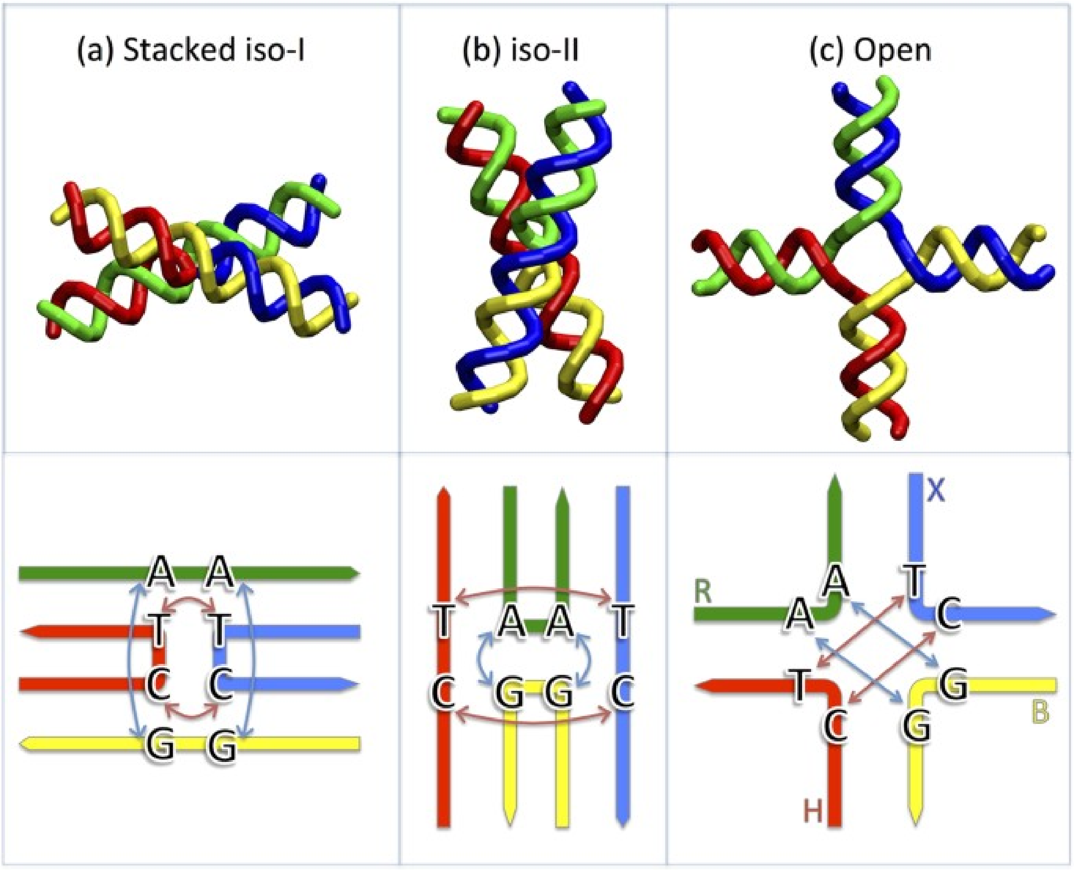

Figure 1.4: Three conformations of Holliday junction. These conformations are salt dependent, i.e. Stacked iso-I and iso-II (a and b) are more probable at higher salt concentrations, while Open conformation (c) is observed under weaker ionic conditions. Colors represents different ssDNA strands. Adopted from [5].

In order to build more complex structures, it is necessary that the mixture of DNA sequences assembles into highly ordered and designed structure. It is therefore necessary that the entropic loss resulting from such change is compensated by the gain in the energy of binding, i.e. the system needs to go to a state of minimal energy. Furthermore, during this self assembly process, it is possible that the kinetics of the energetically favourable state is too slow compared to kinetics of energetically unfavourable state. When this occurs, system is in a metastable state, or kinetically trapped. For DNA nanostructures the rule of thumb is simple: the resulting structure has to have longer dsDNA domain than it had before the reaction occured, this difference should be larger than 3 bases. Besides stabilization forces, stacking interactions, vertical base-base interactions, offer additional stability for DNA molecules, and can be utilized for the purpose of building more complex DNA structures.

1.2.1 Structural DNA nanotechnology

In principle, we distinguish two basic schools of design in DNA nanotechnology, the "tile-based approach" developed by Nadrian Seeman, where multiple strands, each with one part complementary to other and more recent "scaffold-based approach", also called DNA origami, introduced by Paul Rothemund in 2006 [6]. Figure 1.5 shows the two schools of DNA design. In the Seeman's approach, multiple homologous strands are design and incubated to form a desired structure. In the scaffold based approach, multiple strands are incubated with long scaffold sequence. This approach is discussed in greater detail in Chapter 2.

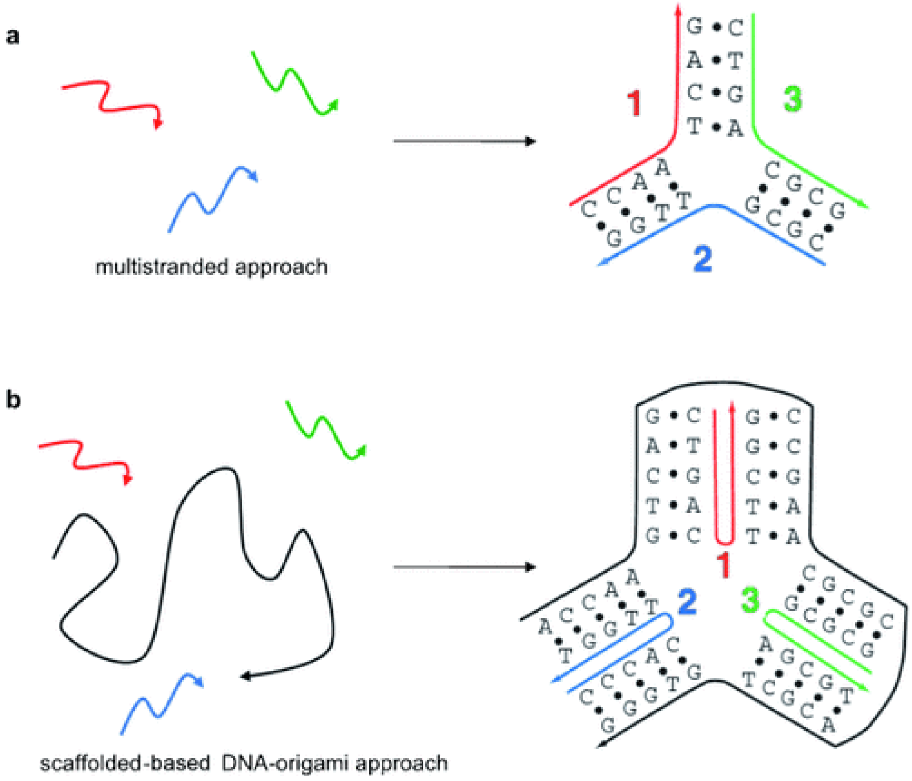

Figure 1.5: Tile based approach; three different strands, sharing some degree of complementarity (top) and scaffold based approach, scaffold strand is shown in black, staple strands in colors (bottom). Adopted from [7].

1.2.2 Functional DNA nanotechnology

Programmability of DNA strands allows the design of dynamic DNA systems which can operate in predictive behaviour. Functional DNA nanotechnology can be understood as focused on the mediate steps in formation of DNA structures. Where structural DNA nanotechnology cares about the final product of DNA interactions, and doesn't care about the steps taken during the assembly, functional DNA nanotechnology doesn't care about the final architecture, since the focus is on the specific steps undertaken while system is going towards the minimum of energy. First such system was designed by Mao et al in 1999 [8]. They were able to sense the B $\leftrightarrow$ Z transition in DNA molecule by designing a DNA machine that would perform a screw motion in the presence of cobalt ions, which induce the transition. Dye molecule was attached to the nanodevice, upon transition, screwing would quench the molecules, and transition is detected. Kinetic traps are also often utilized when building dynamic DNA motifs. Indeed, one such naturally occuring motif, is the hairpin structure, found in ssDNA or RNA. Hairpin sequence in general consists of self-complement domains at each end and non interacting part in middle. The structure folds onto it self into two domains, hybridized stem formed by complementary ends which are further connected by non interacting loop. Figure 1.6 shows randomly generated 32bp long ssDNA that folds into itself to form the hairpin. Hairpin was designed and visualized with NUPACK [9]. In their extensive study of the design and kinetics of DNA hairpins, Green et al. proposed DNA hairpins as an ideal candidates for fuelling autonomous DNA nanomachines [10]. One such autonomous DNA machine, fueled by DNA hairpins, is the basis of Hybridization Chain Reaction, which can be understood as a nanomachine capable of performing signal amplification [11][12]. Recently, reusable logic circuits based on DNA hairpins were also achieved [13].

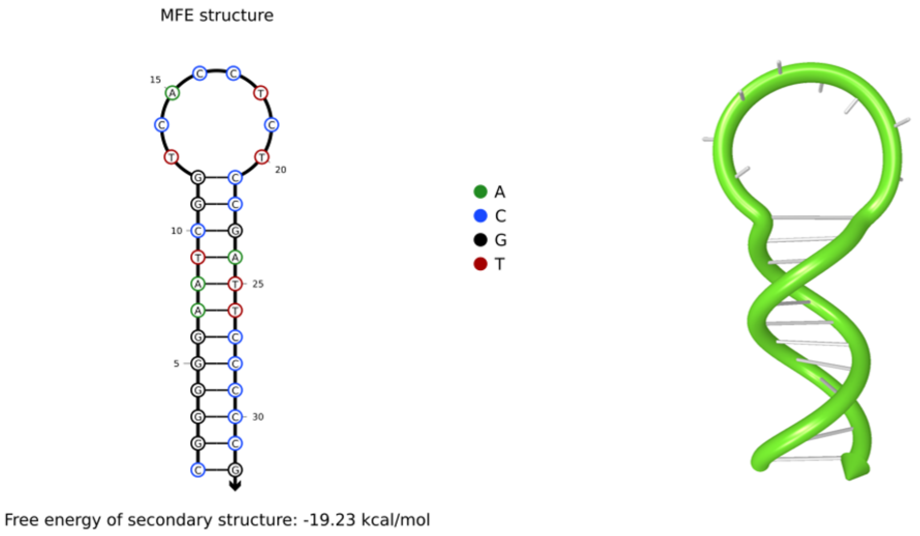

Figure 1.6: Left — Random generated DNA hairpin showing also the sequence. Complementary ends fold to form 12bp long stem connected by 8bp long non-interacting loop. Right — approximate model of the harpin showing also the average orientation of the bases and the helical twist. Arrow denotes the 3' end in both cases.

Lee et al designed a DNA nanoparticle capable of delivering small interfering RNAs (siRNA) to cells, and control the expression of targeted genes [14]. Furthermore, in vivo, these nanoparticles were able to survive in blood 8x longer than parent siRNA. Another remarkable example of use of DNA nanotechnology in nanobiotechnology came from de Puig et al who were able to tune blood clotting on and off by designing a mechanism capable of releasing thrombin binding aptamer to inhibit blood clotting, and releasing complementary DNA to bind to aptamer and initiate blood coagulation cascade [15]. Gain in energy in DNA self assembled systems is ensured by the toehold mediated strand displacement, enzyme-free mechanism for sequence exchange, first utilized by Yurke et al [16]. They developed a system exhibiting predictable conformational transition based on recognition of fueling DNA strand, Figure 1.7.

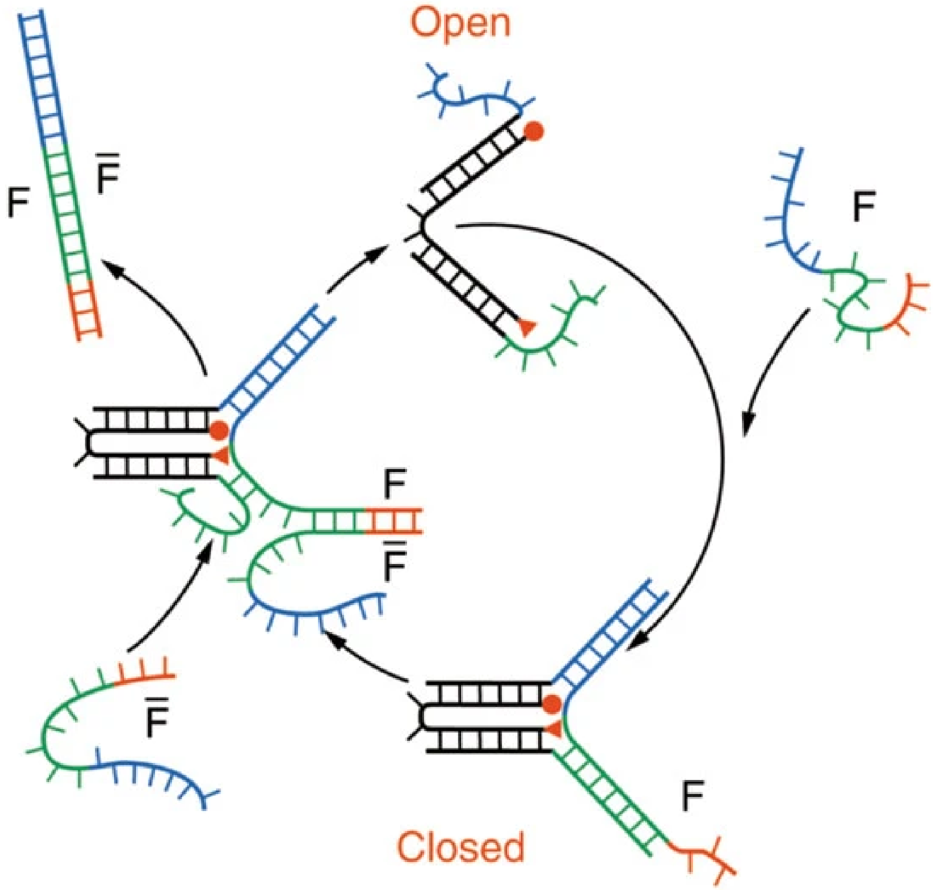

Figure 1.7: Molecular scissor and toehold mediated strand displacement mechanism. Nicked DNA molecule with conjugated with fluorescent dyes is initially in open conformation. Overhangs are colored with blue and green color. Incubated fuel strand F binds to overhangs and closes the dyes, resulting in closed conformation. Closing is made possible by nicking which ensures additional flexibility. Fuel strand also carries additional overhang (red), which allows the fuel strand to be stripped away with remover strand $\bar{F}$. This ensures the reversibility of the reaction because the conjugated complex prefers to be in open conformation without the presence of fuel strand. Adopted from [16].

Cost of DNA nanotechnology

Field of DNA nanotechnology was greatly expanded by recent advances in DNA synthesis, which additionally decreased the cost of producing short synthetic DNA strands. In fact, in the last 30 years, the per-base cost of short DNA sequences has dropped by more than one order of magnitude, and more than two orders of magnitude for longer DNA sequences. At the same time, sequencing human genome in late 80s costed millions of U.S. dollars, nowadays it's on the order of 1000$. However, despite obvious financial advancements in recent decades, producing some concentration of particular origami structure for example is still considered to be somewhat expensive. Origami structures usually, based on complexity, require hundreds and more different staple strands, each of which is 30-50 bp long, meaning that price of just staples will be around €2000 [b], when scaffold strand is added, the price for the single type of origami can easily reach €3000.

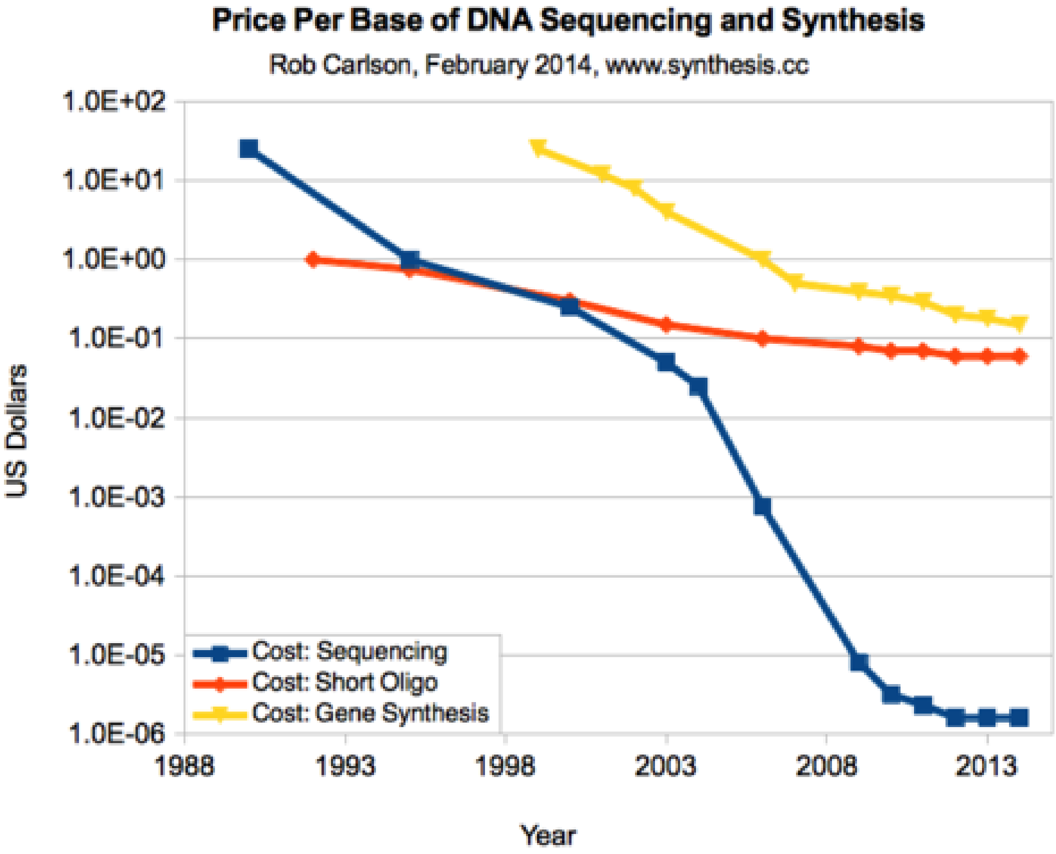

Figure 1.8: Carlson curve, Moore's law for biotechnology. Price evolution of DNA manipulation, writing and reading, from 1990 - 2013. Sequencing technology went through remarkable breakthroughs at the beginning of the millenium, dropping in price 1 000 000 times (blue). Cost of DNA synthesis also dropped during the same period, long gene synthesis (yellow) and short DNA oligomers (orange). Adopted from [17].

---

[b] Assuming smallest production scale and no additional purification nor functionalization from the manufacturer

1.3 DNA based biosensors

Biological sensors, or biosensors, are small analytical devices capable of detection and characterization of various biological analytes. In addition to detection and characterization, biosensors can also be build to allow the characterization the interactions between or with specific biological molecules. In principle, biosensors are devices used both for commercial purposes and in research studies. There are several key parameters defining the overall perfomance of the biosensor:

- Sensitivity - minimum analyte concentration required to generate signal
- Selectivity - sensor ability to distinguish from target analyte and environment, usually defined by Signal-to-Noise ratio (SNR)
- Sample volume - overall volume required for the sensor to be operational (connected to sensitivity)
- *Ease-of-use*
- *Time-to-results*

There are three main features of the biosensor: (i) a receptor site, or probe, (ii) transducing element and (iii) signal processing unit. General layout of a biosensor is shown in Figure 1.9.

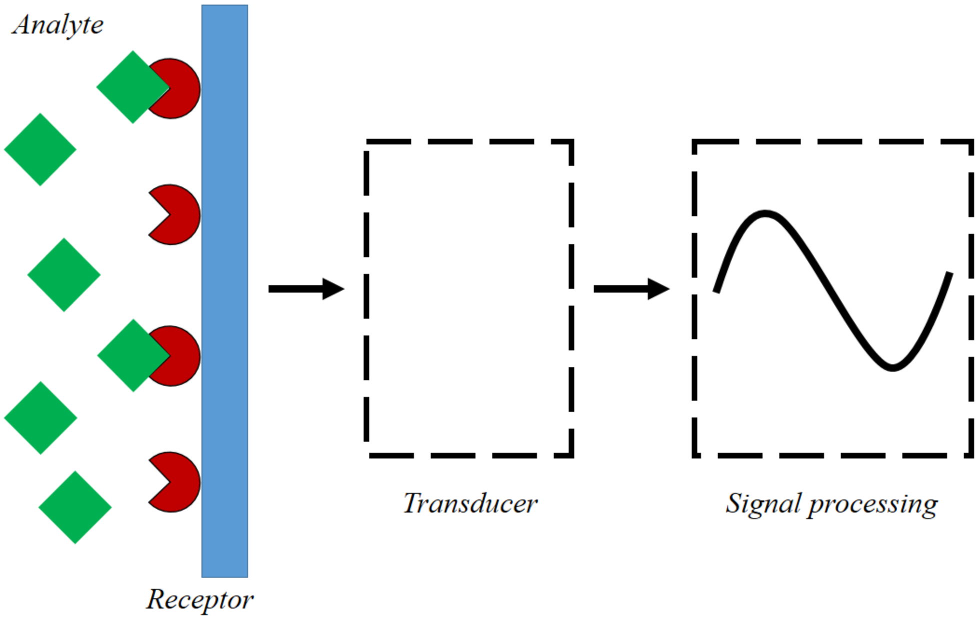

Figure 1.9: Biosensor typically consists of three main components: a bio-recognition sensing site or a bioreceptor, a transducer component, and an readout processing system. The recognition site can utilize specific biomolecule or specific surface to interact with the analyte of interest. The transducer translates this interaction and generates a signal proportional to the amount of analyte at the sensing surface. This signal is received by the electronic system, where is eventually displayed.

Based on the signal processing unit, we can distinguish equilibrium from real-time biosensors. For equilibrium biosensing, readout can be done only after the steady state is reached, whereas real-time biosensors allow the readout at any point. Moreover, real time biosensors have the advantage of kinetic analysis in addition to equilibrium. Transducing element offer another layer of biosensor classification, depending on the nature of transducing, i.e. optical, electrical, magnetic or thermal, of which optical is most widely used. Transducing can be further supported by labelling probes and analytes. Depending on the presence of labels, we distinguish label and label-free biosensors. Finally, at the front of the biosensor we have the probes (receptor area) as the first layer of the device. Depending on the sensing analyte, sensing probes can be biomolecules or special functionalized surface that can adsorb the analyte. It's worth nothing that sensor parameters listed at the beginning of the chapter are also affected by the sensing probe (bioreceptor) used, not just the type of the sensors, as we shall see in the following chapters. Considering the scope of this thesis, following discussion on the biosensing will be constrained to DNA biosensors, i.e. sensors where DNA was used as on sensing surface.

1.3.1 DNA microarrays

Ever since their creation, 40 years ago [18], DNA microarrays have become most widely employed types of DNA biosensors. DNA microarrays owe their widespread use to the great success these DNA chips showed in gene expression analysis [19][20], transcription factor binding analysis [21][22] (See also Chapter 3, section 1.3) and genotyping [23][24]. Recently, we showed that our optical biosensing technique, Reflective Phantom Interface, more about it in Chapter 2, Materials and Methods, is sensitive down to one base mismatches in DNA hybridization, thus could be used to study the detection of single nucleotide polymorphs (SNPs) [25]. Typical DNA microarray consists of DNA bundles grafted on surface, usually glass, silicon or plastic, and organized in patterned array of spots. Each spot usually contains between 10^{11} - 10^{13} probes per cm^{2}[c]. Typical probe lengths used in microarray investigations are between 10 and 300 bases. Based on the probe size, we distinguish oligonucleotide arrays (up to 50mer probes) and cDNA arrays, with longer probes. Figure 1.10 visualizes the DNA microarray.

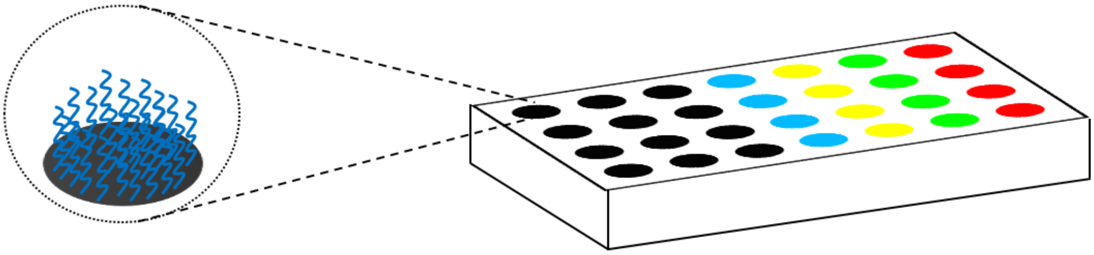

Figure 1.10: DNA microarray illustration. Bundles of DNA probes are deposited in ordered fashion, as array of spots. Colored spots are here to indicate the multiplexing potential of DNA microarrays. In principle, those spots could hold bundles of protein or different DNA probes (different sequence, concentration, etc...).

---

[c] This corresponds to area per probe of 800 nm^{2} to 8 nm^{2}

Biggest advantage of microarray biosensors comes from it's multiplexing ability and parallel reading. Because the sensing surface of DNA microarrays can contain thousands of spots that are exposed to the sample holding solution, DNA microarrays offer the possibility of sensing multiple different biological analytes simultaneously. In fact, typing and subtyping of Influenza viruses is a quite common practice nowadays and is carried out on DNA microarrays [26][27]. However, despite it's obvious advantages, DNA microarrays are still analyzed using bulky instrumentation and require time-consuming preparation after which DNA array can only detect molecules it was designed to detect, it is a single-use sensor in that sense. Furthermore, DNA arrays achieve stronger response, and thus higher sensitivity, at higher probe densities. This gives rise to new problems regarding DNA microarrays. Because ssDNA are highly flexible polymers, they can explore very large area, once grafted onto surface, this combined with high grafting density results in steric effects that further hamper the hybridization efficiency and kinetics of DNA microarrays.

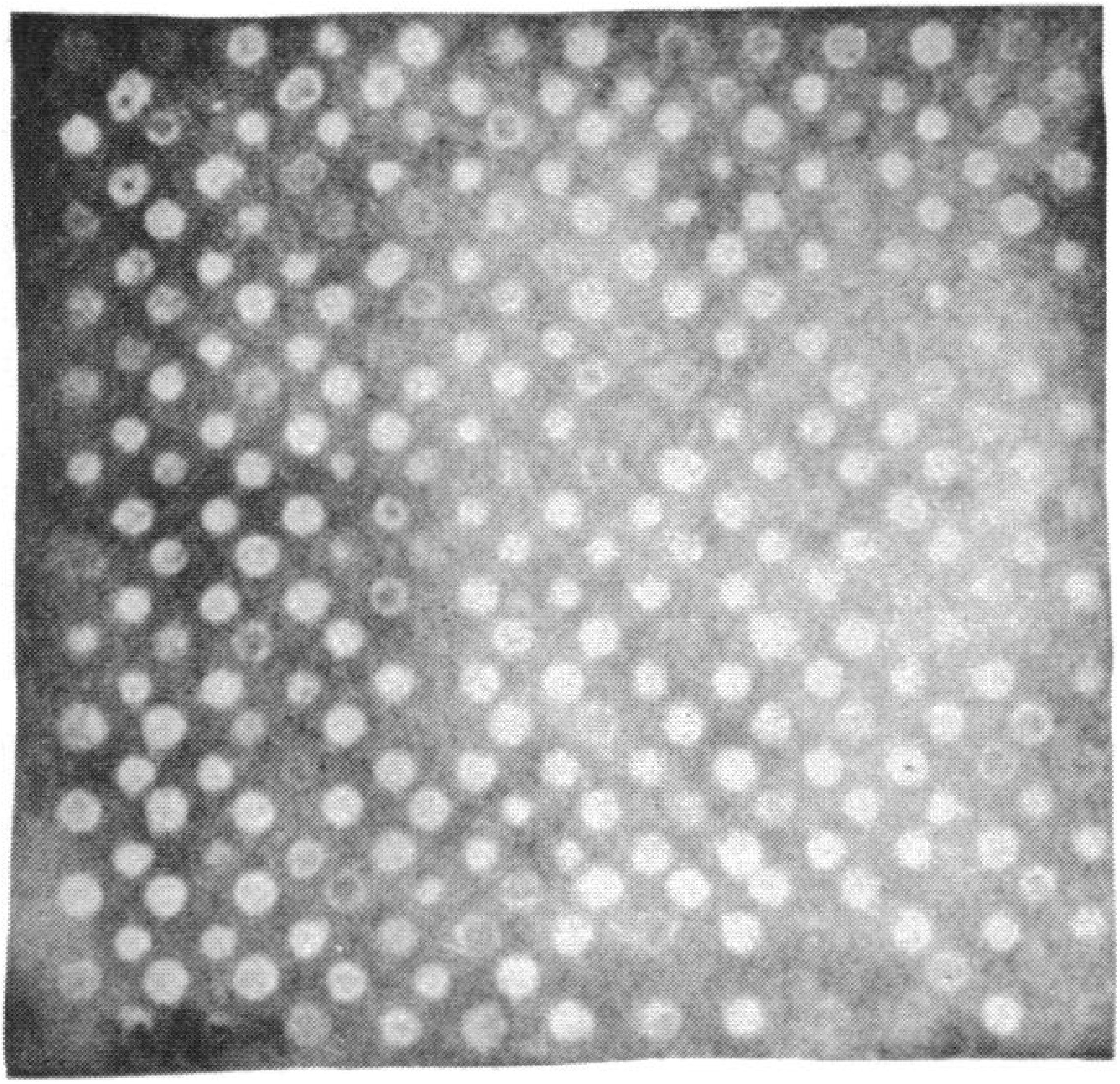

Figure 1.11: Recombinant DNA plasmids extracted from Drosophila Melanogaster genome. DNA was stained with ethidium bromide and imaged under UV light illumination. Original DNA microarray image from [18].

In addition to forementioned steric effects, high density of ssDNA probes, combined with charged nature of DNA molecules, produces high electrical fields that further hamper DNA microarray sensitivity and rapidity. In fact, several approaches have been proposed to minimize these effects. Qamhieh and Pettitt proposed increasing the distance between the probe and the surface by the use of so-called linkers, and adding external surface electrostatics to reduce the electrostatic repulsion [28]. In their work, they showed an average increase of hybridization yield by 20% for probe densities between $4 \cdot 10^{12}\,\mathrm{cm}^{-2}$ and $8 \cdot 10^{12}\,\mathrm{cm}^{-2}$ by changing from dielectric to metallic substrate. Increasing the probe distance from the metallic substrate further increases the hybridization efficiency by 90%, on the probe density of $6 \cdot 10^{12}\mathrm{cm}^{-2}$. Peterson et al showed a 4-fold increase in amount of immobilized ssDNA when salt concentrations was increased from 0.1M NaCl to 1M NaCl [29]. Dandy et al considered morphological profile of DNA microarray spots while studying the hybridization of 20-mer sequences on gold surface and argued that hybridization efficiency can be optimized by transitioning from diffusion limited regime to reaction limited regime, which was regulated by assay miniaturization [30].

Chapter 2

Materials and methods

The following chapter will cover some details into experimental and theoretical concepts relevant to the research discussed later. The chapter starts with electrostatic theory of DNA hybridization [31][32]. I will give the derivation of the modified Langmuir isotherm and explicit form for electrostatic penalty, which was the basis of the model described in Chapter 3.1. This is followed by the section on experimental technique, Reflective Phantom Interface (RPI), used in all experiments throughout this thesis is discussed. Finally, details of our DNA origami structure and folding protocol, based on the rectangle designed by Paul Rothemund are discussed at the end [6].

2.1 DNA array models

Widely used approach, when analyzing biosensor data, is the well known Langmuir model [33]. Even though the model was originally developed having surface adsorbtion of gas molecules in mind, the model proved effective in other areas as well, such as biosensors. In the language of microarrays, this model relies on the following assumptions [34]:

1. All probes within the spot are same, i.e. in the case of DNA probes, all probes in the spot have the same exact sequence.
2. Each probe can only bind to one specific target, i.e. one probe cannot bind multiple targets, at different times.
3. Targets are mutually non interacting, i.e. there is no target-target hybridization happening in solution (in the case of NA targets).
4. Upon binding, target is bound only to one specific probe, i.e. one target cannot occupy multiple binding sites at once.
5. There is no interaction between probes, irrespective of their hybridized state.

Upon closer examination, we realize that all these requirements are somewhat difficult to satisfy when considering DNA microarrays, for longer probe and target strands, points (2)-(5) present serious obstacles, as DNA has limited choice for bases it can recognize, non-interaction rule imposed above becomes practically impossible. However, charged nature of DNA molecules presents another layer of problems when analyzing DNA microarray binding curves. Indeed, a well known experimental fact is that there are substantial differences between DNA hybridization in solution and on surface [35]. This can be understood in terms if local charge densities within the sensing chip. Typical DNA microarray consists of bundles of DNA grafted in small spots. Each spots has 10^{10} - 10^{12} DNA molecules per mm^2. In addition, typical DNA probe is 10-50 nucleotide long, and carries that much charges - one nucleotide carries charge of -1e. This fact results in high local electric fields arising from high density bundles of DNA probes on surface. Furthermore, as hybridization proceeds, DNA layers are adsorbing more and more DNA, which in fact increases the number of charges and overall electrostatic repulsion, meaning that insertion of new DNA target into a charged layer of DNA probes requires more and more energy, therefore hybridization efficiency must depend on the overall number of duplexes already formed in the layer. This was not accounted for in the Langmuir binding isotherm:

$$\phi = \frac{1}{1 + c_t^{-1} exp(\Delta G/kT)} \tag{2.1}$$

where $0 < \phi < 1$ is the hybridization yield (or fraction), c_t is the target concentration, ΔG is the Gibbs free energy and kT is the product of the Boltzmann constant and temperature. One model where interaction between adsorbing species is considered is covered within the Frumkin isotherm [36]:

$$\frac{\phi}{1-\phi} exp(-2a\phi) = c_t exp\left(\frac{-\Delta G}{kT}\right) \tag{2.2}$$

where a is the so-called attraction constant, which takes negative values when interaction between adsorbed species is repulsive, and positive values when the same interaction is attractive. Setting c_t to relative concentration at half the surface coverage, we obtain the analytical form of the surface coverage y:

$$y = \frac{\phi}{1-\phi} exp(a - 2a\phi) \tag{2.3}$$

which allows the calculation of the attraction constant a.

Vainrub and Pettit developed a hybridization binding isotherm for surface DNA hybridization by introducing the Gibbs free energies for DNA interactions [31]:

$$\Delta G = \Delta G_0 + V_{pt} - V_p - V_t \tag{2.4}$$

where ΔG_0 is the free energy of the formation of single dsDNA, V_{pt}, V_p and V_t are the free energies for the ds duplex, probe and target, respectively. Another effect of this layer-target repulsion is the formation of the so-called "depletion zone", where targets near to layer area either bind on the surface or are repelled back in solution. The concentration profile of the targets near the surface decreases exponentially towards the solution as:

$$c_t(z) = c_{t,0} exp(-V_t(z)/kT) \tag{2.5}$$

where z is the coordinate along the distance from the DNA layer into solution. Combining Equations 2.5 and 2.4 with Equation 2.1 we obtain the hybridization binding isotherm modified for electrostatic interactions:

$$\frac{1-\phi}{\phi} = c_t exp\left(\frac{\Delta G}{kT}\right) exp\left[\frac{V_s N_p \sigma_p (1+\phi)}{kT}\right] \tag{2.6}$$

where N_p is the number of bases in the probe sequence, σ_p is the surface probe density and V_s corresponds to change in free energy associated with the duplex formation. For more details on this please refer to [28][31]. Overall, $V_s N_p \sigma_p / kT$ corresponds to the electrostatic penalty associated with insertion of charged DNA molecule into already charged layer of DNA probes. This electrostatic was derived in specific form by Halperin et al [32]. The equilibrium state of the dsDNA formation on the surface can be written in terms of potentials as:

$$\mu_{pt} = \mu_p + \mu_t \tag{2.7}$$

specifically, for condition where target concentration c_t does not change with ongoing adsorbtion, i.e. $c_t >> c_p$, we can write:

$$\mu_t = \mu_t^0 + kT \ln c_t \tag{2.8}$$

Furthermore, at equilibrium, in probe layer there are $\phi\sigma_p$ hybridized probes and $(1-\phi)\sigma_p$ unhybridized probes. Thus, we can treat the spot as a mixture of two distinct molecules, hybridized probes *pt* and unhybridized probes *p*, therefore, for free energy per probe site, we write:

$$\gamma_{site} = \gamma_0 + \phi\mu_{pt}^0 + (1-\phi)\mu_p^0 + \Sigma\gamma_{el} + kT\left[\phi \ln \phi + (1-\phi)\ln(1-\phi)\right] \tag{2.9}$$

where Σ corresponds to surface are per probe γ_0 is the free energy density of the surface of area Σ, μ_{pt}^0 and μ_p^0 are the free energies of single hybridized and unhybridized probe, respectively. Rewriting Equation 2.6 in terms of exchange chemical potential, we obtain:

$$\mu_{pt}^{ex} = \mu_{pt}^0 - \mu_p^0 + N_p \frac{\partial \gamma_{el}}{\partial \sigma_p} + kT \ln \frac{\phi}{1-\phi} \tag{2.10}$$

where $N_p \partial\gamma_{el}/\partial\sigma_p$ is the electrostatic free energy penalty associated with insertion of charged DNA target into probe layer to reach the hybridization fraction ϕ. Equilibrium condition $\mu_{pt}^{ex} = \mu_t$ leads to Equation 2.6, obtained from [31]:

$$\frac{\phi}{1-\phi} = c_t exp\left(\frac{-\Delta G^0}{kT}\right) exp\left(\frac{N_p}{kT} \cdot \frac{\partial \gamma_{el}}{\partial \sigma_p}\right) \tag{2.11}$$

where now $N_p(\partial\gamma_{el}/\partial\sigma_p)$ is the electrostatic penalty, as in Equation 2.6. To obtain the electrostatic penalty in specific expression we need to compute the $\gamma_{el}(\sigma_p)$. Solving for the free energy of a capacitor with thickness H, we get:

$$\frac{\gamma_{el}}{kT} = 4\pi\sigma_p^2 l_B \frac{r_D^2}{H} \tag{2.12}$$

and finally, $N_p(\partial\gamma_{el}/\partial\sigma_p)$ leads to specific expression for dimensionless electrostatic penalty associated with insertion of charged DNA molecule into the like-charged DNA probe layer, Γ:

$$\Gamma = 8\pi N_p N_t \sigma_p l_B \left(\frac{r_D^2}{H}\right) \tag{2.13}$$

where N_p and N_t are probe and target length in nucleotides, respectively, σ_p is the number probe density, l_B is the Bjerrum length and r_D/H corresponds to Debye length divided by layer thickness.

2.2 RPI

All DNA-analyte interactions were measured with Reflective Phantom Interface (RPI). RPI is a reflectance based, label-free, optical biosensing technique which is based on increase of reflected light intensity upon mass adsorbtion on a surface with initially very low reflectivity [37]. This low initial reflectivity is made possible by anti-reflective layer of SiO2 with thickness of $\lambda/4$, where $\lambda = 455$ nm is the wavelength of the light source used, which is coated on the glass surface. Anti reflective layer can further be coated with various surfactants that are designed to bind and form layers of specific sensing probes. Figure 2.1 shows cross section of the sensing chip in the cuvette and illustrates the working principle of RPI.

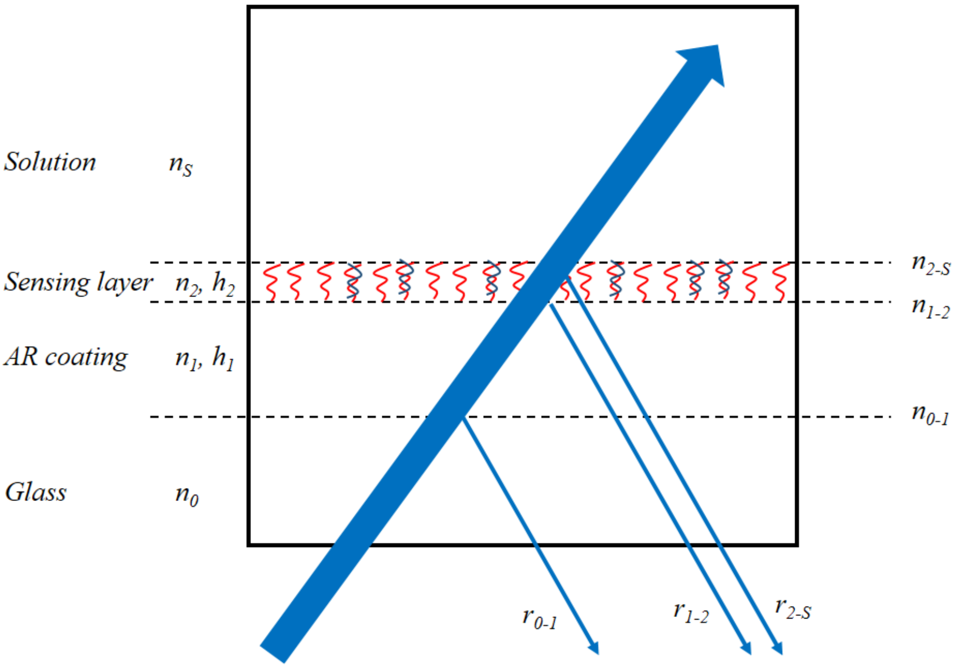

Figure 2.1: RPI working principle.

Model which allows us to quantify the molecules adsorbed on the sensing surface of the RPI is described in detail here [38]. Overall thickness increase h scales with increased reflectivity R:

$$R = \left(\frac{r}{1+r^2}\right)^2 (\beta^2 + \epsilon^2) \tag{2.14}$$

where r, β and ϵ are defined as:

$$r = (r_{1s} + r_{01})/2 \tag{2.15}$$

$$\beta = (r_{1s} - r_{01})/2 \tag{2.16}$$

$$\epsilon = (2hn_1\langle k\rangle - \pi)^2 + (2hn_1\Delta k)^2 \tag{2.17}$$

where r_{01} and r_{1s} are the reflections from glass-coating and coating-solution interfaces, respectively, h is the total effective thickness - sum of layers weighted by their respected refractive index, n_1 is the refractive index of the AR coating, $\langle k\rangle$ is the average wavenumber and $\Delta k^2 = \langle k^2\rangle - \langle k\rangle^2$ is the wavenumber variance. Explicit equation for thickness h as a function of reflectivity R is obtained for: $h_1 \approx h_0$ and $h_2 << \lambda$:

$$h_2 = \frac{1}{c_2}\left(h^*\sqrt{\frac{R_0}{R} - 1} - \delta h\right) \tag{2.18}$$

where $c_2 = (n_2^2 - n_s^2)/(n_1^2 - n_s^2)$, $\delta h = h_1 - h_0$ and $h^* = (\beta^2 + \sqrt{(\pi\Delta k/\langle k\rangle)^2})/(2n_1\langle k\rangle)$. Finally, we obtain the bound mass density:

$$\sigma = \rho\Delta h \tag{2.19}$$

where ρ is the density of the compact layer of biomolecules estimated from [39]. For full details of the previous derivation please refer to [38] and supplementary information therein.

2.3 DNA origami

DNA origami is a novel technique that allows bottom-up fabrication of functional biological nanostructures with sub-nm precision. DNA origami exploits intrinsic properties of DNA molecules, i.e. specific Watson-Crick selectivity and general DNA molecule geometry. Figure 2.2 shows some of the produced structures in the original paper.

Scaffold sequence, a long ssDNA, 10^3 bases, is folded into a fixed shape with the help of many smaller ssDNA sequences, staple strands (or just staples), 10^1 base long. Staples are designed in such a way that they bind one part of the scaffold with half of their length, and some other non-adjacent part of scaffold sequence with second half of the length. This results in bending of the scaffold sequence and the formation of the so-called crossover, where scaffold sequence is bridged via staple. Position of the crossovers defines the final structure. Origami structure is visualized in Figure 3.3. In general, folding of origami structure, assuming one has the structure designed, i.e. crossover sequences are designed, starts with preheating the mixture of scaffold sequence and staples in concentration excess. This preheating causes the scaffold structure to denaturate since innerstrand interactions and hairpins are broken by temperature. Following the preheating, the sample is then slowly cooled to room

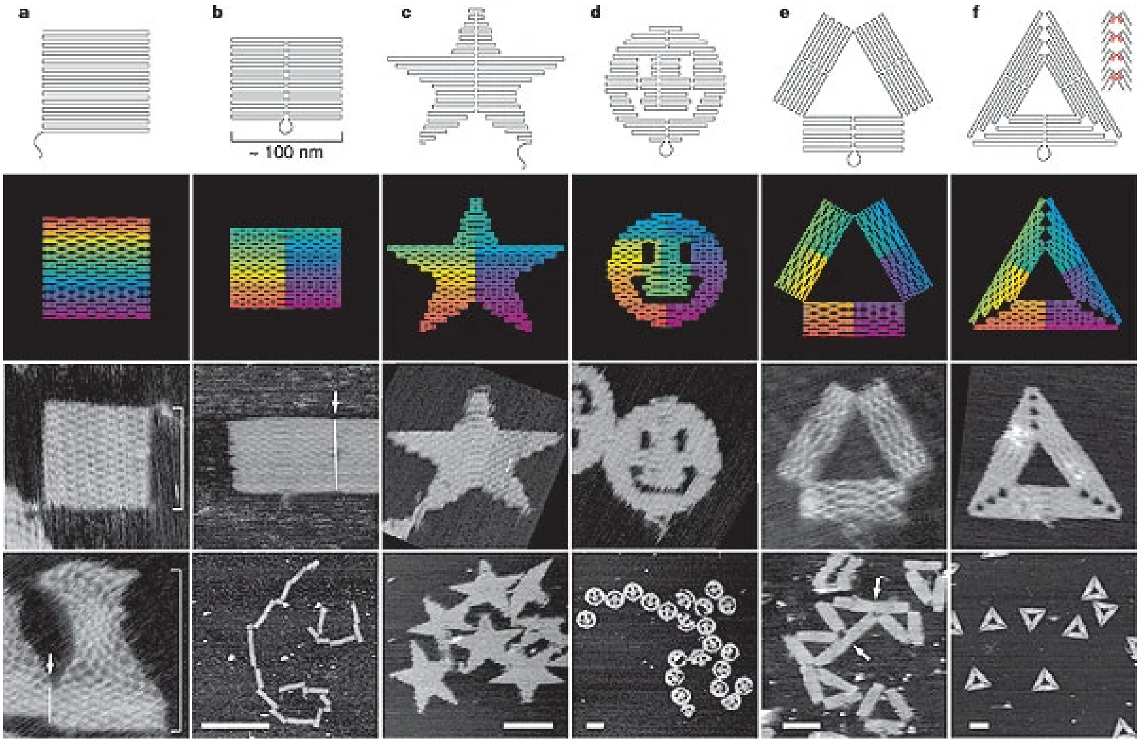

Figure 2.2: Various planar shapes, produced by Paul Rothemund in [6]. Rows from top to bottom show: Scaffold routing for square (a), rectangle (b), star (c), emoji (d), triangle with rectangular domains (e), triangle with trapezoidal domains (f); second row: colored by staple index along folding path; third and forth row: AFM images of forementioned structures.

temperature to allow the staple strands to bind on the scaffold complements. Structure design and folding protocol will be discussed in greater detail in the following chapters.

DNA origami designs

DNA origami structures were designed with caDNAno [40]. All designs are original rectangle structure designed by Paul Rothemund in [6]. Structure was corrected for the induced global twist, following a procedure from [41]. Skipped bases are shown as red 'x' in Figure 2.4. Rectangle structures were analyzed with CanDo [42] and tether placement regions were defined based on the overall structure stability, Figure 2.5. 40 bp tethers were designed manually and concatenated to original staples, extending from the 3'. Final location of the tethers is shown Figure 2.4, as red colored staples[a]. In order to obtain greater flexibility, tethers were further displaced from the structure via 6-A linker. Tether control was carried out by NUPACK [9] to ensure their stability and potential crosstalk.

---

[a] Green colored staples are intended for further functionalization, discussed in last chapter

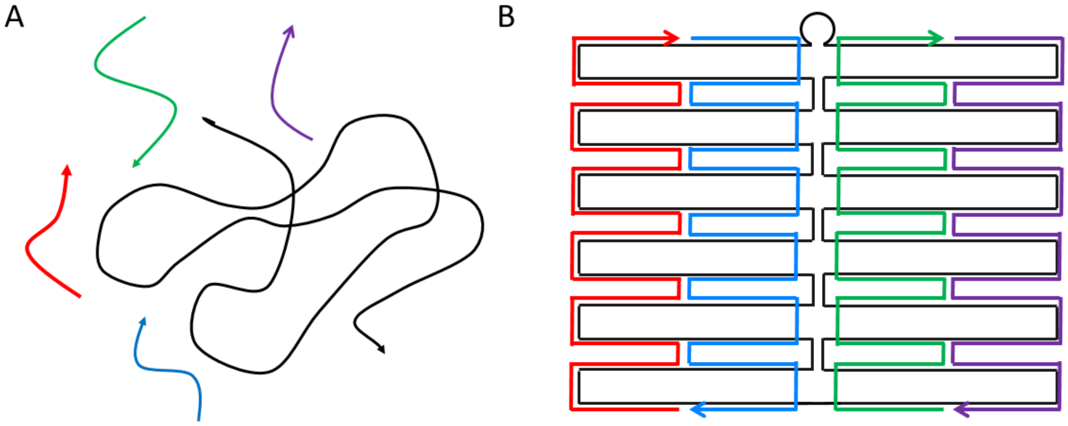

Figure 2.3: A - Scaffold strand (black) is incubated in the folding buffer with staple strands (colored according to sequence), in principle, staples are incubated at 5-10x higher concentration relative to the scaffold. B - following the thermal annealing, staple find the complementary counterparts on the scaffold and fold.

DNA origami folding protocol

Scaffold sequence from a bacteriophage M13mp18 was incubated at 50 nM with 300 nM staple sequences, yielding in 6x concentration excess, mixed with folding buffer, 1xTE (Tris-EDTA) + 12.5 mM MgCl2.linker sequences where added afterwards at 1000 nM each. To remove possible competitions, default origami staples produced with caDNAno superimposed with linker sequences where not incubated. Solution was brought to 100 µl with ddH2O. To denaturate the scaffold and expose the bases to staples, the solution was first heated to 75°C and kept at constant temperature for 15 min. After which the sample was cooled to 60°C with a -2°C/min rate. This was followed by slower cooling ramp between 60°C and 35°C at -0.5°C/min. Finally, solution was brought to room temperature (RT) at -2°C/min. Temperature ramp is shown in Figure 2.6. Excess staples were removed by mixing 1:1 volume ratio with 7.5%(w/v)PEG-8000 + folding buffer and ultracentrifugation for 30 min at 18000 rcf at RT as described here [43]. Supernatant solution was discarded and remaining sample was resuspended in folding buffer.

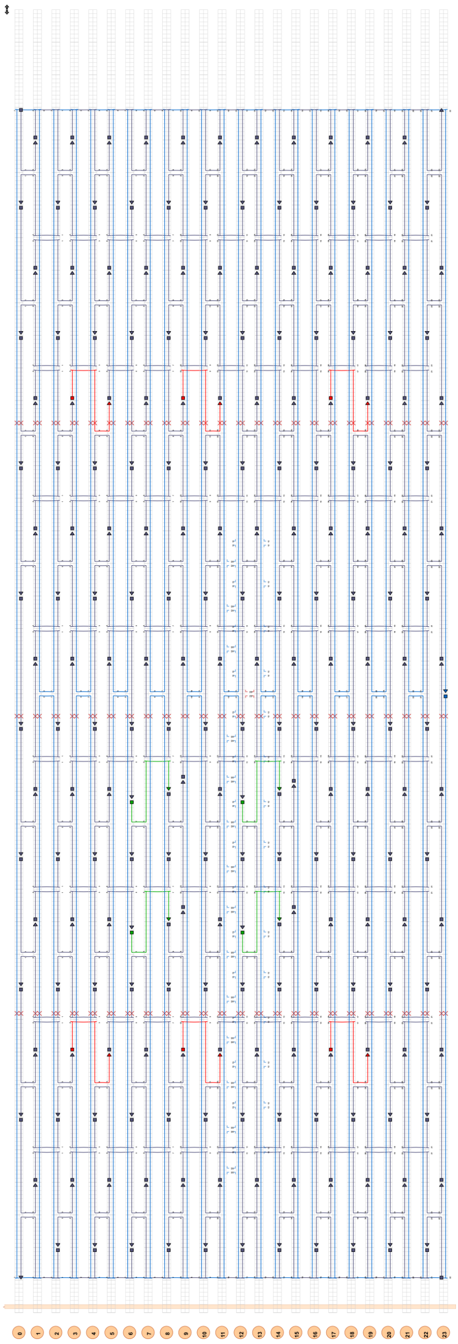

Figure 2.4: caDNAno origami design. Scaffold sequence is shown in blue, staples are colored grey. Specificaly, staples that were extended to bind the structure to the surface are colored red. Green staples are intended for extension in future experiments. Skipped bases are denoted with red 'x'.

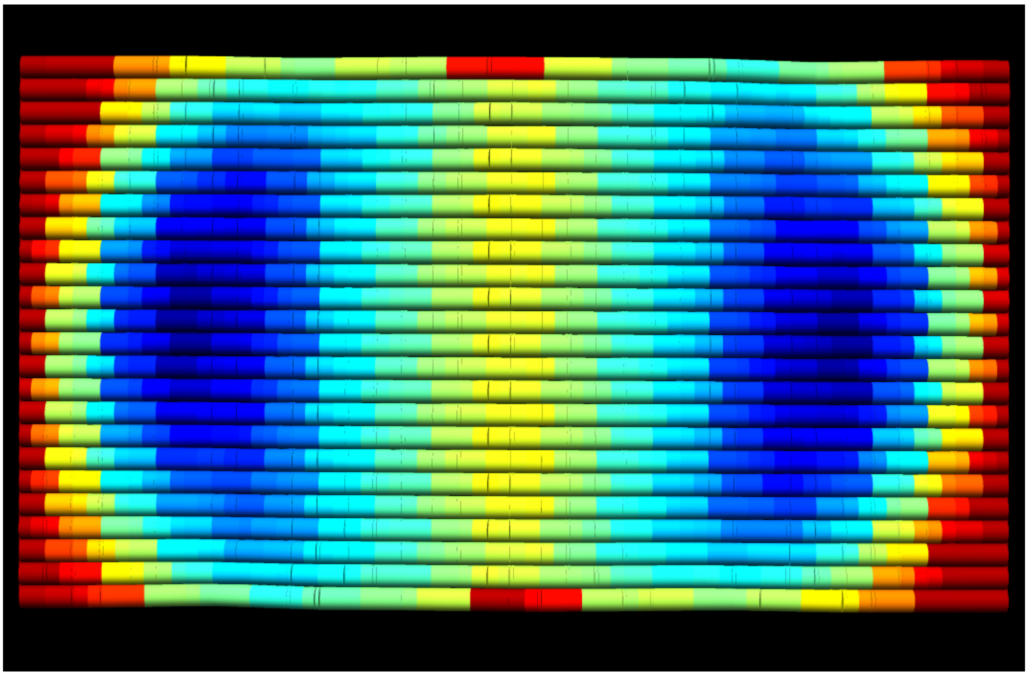

Figure 2.5: CanDo prediction of structural stability of DNA origami rectangle [42]. Heatmap indicates root-mean-square fluctuations (RMSFs), stability decreases from blue to red.

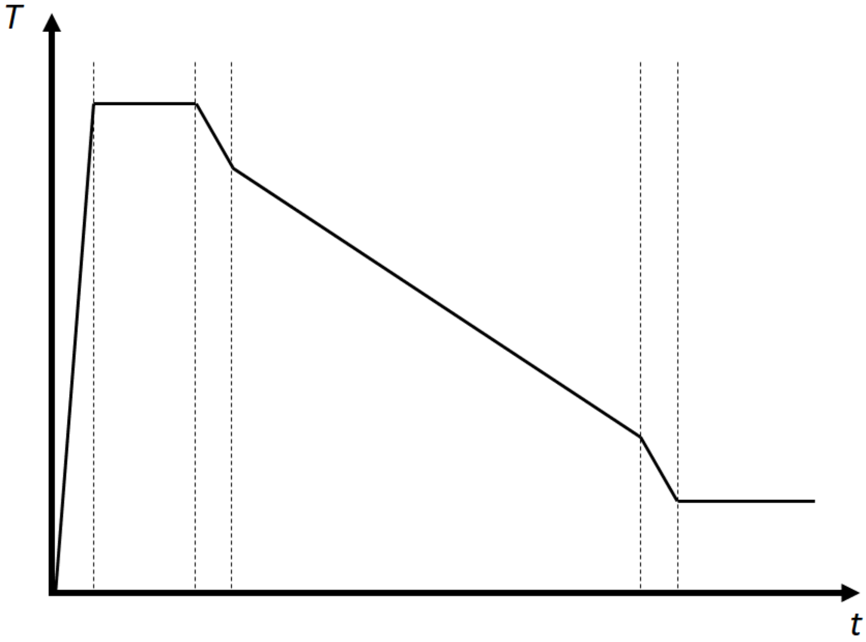

Figure 2.6: Generic origami folding ramp.

Chapter 3

Results

In the following chapter I will cover the relevant results obtained during my PhD fellowhsip. The first half of the chapter will be focused on papers where DNA was used simply as a biosensing probe. Section 3.1.1 is a copy of a paper published here [44]. In section 3.1.2 I will address the paper on miRNA detection and provide details of the assay optimization. Section 3.1.3 is focused on our paper on protein detection with DNA probe. Last half of the chapter will be focused on building more complex structures on surface. Section 3.2.1, is dedicated to our study of Hybridization Chain Reaction. Finally, last section, 3.2.2, is focused around ongoing study of binding DNA origami nanostructures on surface as means to achieving nanometer probe control.

3.1 DNA as a biosensing probe

3.1.1 Non-Langmuir kinetics of DNA hybridization on surface

Introduction

The formation of double-stranded DNA (dsDNA) from two complementary strands, called hybridization, is a fundamental process underlying DNA microarray technology [45], as well as the rapidly expanding field of DNA nanotechnology [46]. DNA microarrays (DNA chips) have proven to be a powerful tool in many biomedical applications, from detecting single-nucleotide polymorphisms to gene expression analysis [47]. DNA chips are comprised of singlestranded DNA (ssDNA) immobilized on a surface and acting as probes for complementary ssDNA in solution. Current research efforts in this field focus on two main goals: the development of novel physicochemical methods to improve the transduction of the sensor signal and the design of molecular mechanisms to enhance the sensitivity and specificity of probe-target recognition [48][49]. In particular, DNA nanotechnology offers the opportunity to control the structure and function of complex supramolecular systems and enables the design of programmable molecular machines [50]. A current limitation on the integration of DNA nanomachines on a biosensor surface is that the hybridization with a complementary strand immobilized on a surface generally displays a reduced affinity in comparison with the case in which both strands are freely diffusing in solution [51][52]. Interestingly, such difference between bulk and surface interactions is typically not observed for protein-protein binding (e.g., antibody-antigen) and appears to be a characteristic of the nucleic acid (NA) recognition process. Different possible causes of this phenomenon have been proposed [34][53][25]. More generally, the electrostatic repulsion plays an important role in the decreased hybridization strength on a surface. Indeed, ssDNA is a polyelectrolyte in which each repeating unit bears one negative charge. The accumulation of ssDNA probes on a surface has been reported to induce an effective repulsive potential on freely diffusing complementary strands [54][55], which shifts the equilibrium of hybridization in comparison to the same interaction in solution. Similar to equilibrium parameters, the kinetics of surface hybridization also significantly differs from the same process in the bulk [29][56][57][58].

Despite being fundamental to understanding the origin of the equilibrium features, the kinetics of surface-bound DNA hybridization is still poorly understood [59]. A direct access to real-time binding curves without interference from labeling moieties is provided by label-free biosensors. Since the first studies performed by surface plasmon resonance, it has been shown that the real-time binding curves for DNA hybridization can depend on a number of factors, including the probe surface density, the probe distance from the surface, and the presence of mismatches, and it can display nonexponential behavior, in contrast with a simple Langmuir interaction model describing independent binding events [29][60][61].

However, a general molecular interaction model to account for the kinetic curves for DNA hybridization on a surface is still missing. Indeed, the kinetics of hybridization is not fully understood even in the more standard case in which both complementary strands are freely diffusing in solution [59][62]. In this context, label-free biosensors not only represent a promising application field in which to exploit DNA nanotechnology, but they also provide an effective analytical tool to characterize DNA hybridization at molecular level. Several label-free biosensors have been exploited for sequence detection or quantification [63][64][65][66][67]. Among these, reflective phantom interface (RPI) measures the increase of intensity of light reflected by an interface with very low reflectivity upon binding of molecular targets on surface-immobilized probes. RPI has been demonstrated as a sensitive tool to characterize the kinetic and equilibrium parameters of biomolecular recognition process [37][38] and, in particular, of fully or partially complementary oligonucleotides [25].

Here, we show that the DNA hybridization kinetic curves acquired by label-free optical signals display marked deviations from a Langmuir behavior in a wide range of conditions. We explored different surface densities of complementary probes immobilized with or without a DNA linker, either ss or ds. We studied the hybridization at different concentrations of target strand in solution and ionic strengths.We found that both the equilibrium behavior and the kinetics of hybridization show discrepancies from an ideal Langmuir interaction in all explored conditions. The results support the primary effect of electrostatic repulsion originating in proximity of the surface because of NA accumulation. Moreover, close to saturation of the surface probes by complementary targets, we observed a marked decrease of the apparent kinetic constant for hybridization as a consequence of surface crowding.
The measured reduction of hybridization affinity at large local NA concentrations

strongly affects the results of DNA or RNA microarrays and biosensors and can play a biological role in the cellular environments rich in DNA, such as the nucleus. In general, the enhanced repulsion observed for the hybridization at large DNA local density could contribute to keeping a large specificity of pairing even in a DNA crowded environment.

Materials and methods

DNA strands and reagents

We studied the kinetics of hybridization of a 12-mer model sequence with different surface-immobilized complementary probes. As schematically shown in Fig 3.1, the simplest interaction with a 12-mer probe (no linker) was compared to that measured with probes having an additional ss-linker or ds-linker. The NA sequences used in this work are reported in Table 3.1. Probe strands p1 and p2 were immobilized on the RPI sensing surface, and t1 was used as a complementary target strand in solution. Strand cp2 was optionally used to make a dsDNA spacer at the base of p2. ssDNA were purchased from Integrated DNA Technologies (Leuven, Belgium) with high-quality Ultramer synthesis. Strands p1 and p2 were amine modified at the C6 carbon of 50 terminal (5AmMC6 in Table 3.1). The surface immobilization of amine-terminated ssDNA was achieved by coating the RPI sensing chip with MCP2 or MCP4 copolymers from Lucidant Polymers (Sunnyvale, CA). They are copolymers of dimethylacrylamide, N-acryloyloxysuccinimide, and 3-(trimethoxysilyl)propyl methacrylate, and they differ only in the comonomer molar ratio: 97:2:1 in MCP2 and 89:10:1 in MCP4. The fraction of amine-reactive sites of MCP4 is five times larger than that of MCP2. All buffers and reagents were purchased from Sigma-Aldrich (St. Louis, MO) and prepared according to common protocols using Milli-Q pure water.

Name	Bases	Sequence
p1	12	/5AmMC6/AGG TAA AAG TGA
p2	23	/5AmMC6/GCC CAC CTA TAA GGT AAA AGT GA
cp2	11	TAT AGG TGG GC
t1	12	TCA CTT TTA CCT

Table 3.1: DNA Sequences.

RPI sensor preparation and measurement

DNA probe strands were covalently immobilized on the surface of RPI sensing chips in spots with 150–200 mm diameter, following the procedure described in [38]. Briefly, 8 x 12 mm wedge-like chips of F2 optical glass (Schott, Mainz, Germany) coated with an antireflection layer of SiO2, were plasma cleaned and dip coated with MCP2 or MCP4 copolymer [68]. Droplets of spotting buffer (Na2HPO4 (pH 8.5) 150 mM) containing amineterminated DNA probes at concentrations from 1 up to 30 mM were deposited on the chip surface by an automated noncontact dispensing system (sciFLEXARRAYER S5; Scienion AG, Berlin, Germany). After overnight incubation, the chip surface was rinsed with blocking buffer (Tris-HCl (pH 8) 10

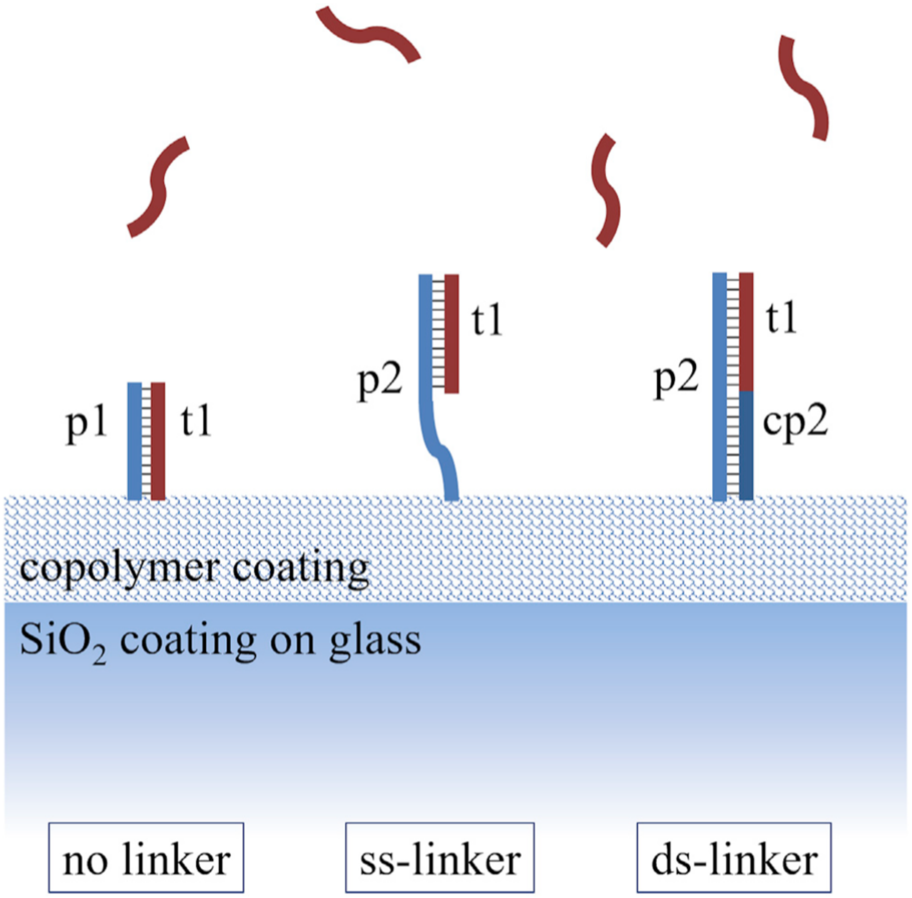

Figure 3.1: Schematics of surface probe types. The 12-mer target strand t1 (dark red) binds to a complementary probe strand (blue) immobilized on the RPI sensing surface by a 3D copolymer coating. Three types of DNA probes were investigated: a complementary 12-mer strand (p1, no linker scheme) and longer probes formed by an ss strand (p2, ss-linker) or a ds strand (p2 + cp2, ds-linker) terminated with the complementary sequence.

mM, NaCl 150 mM, ethanolamine 50 mM) and distilled water and then dried. The sensor cartridges were prepared by gluing the glass chips on the inner wall of 1 cm plastic cuvettes. The cartridges were stored at 4°C before use. Target ssDNA strand t1 and strand cp2 were suspended before use in measuring buffer (10 mM Tris-HCl, 0.02% NaN3 (pH 8.0) + NaCl at different concentrations depending on the measurement). The RPI measurements were performed by using the apparatus and the analysis algorithm described in [38]. The sensor cartridges were filled with 1.3 mL of measuring buffer. The ionic strength was adjusted by adding NaCl from 75 up to 220 mM. In the experiments performed with the dslinker probe, the strand cp2 was added at a concentration of 1.5 mM at least 1h before the measurement to keep the fraction of p2 probes hybridized with the cp2 strand as large as 99% or more during the measurement. The cartridges were kept at 23°C during the measurement through a thermalized holder, and rapid mixing of the solution was provided by a magnetic stirring bar. Sample spikes of target ssDNA were performed by adding 50 mL of measuring buffer containing different amounts of target molecules to a final concentration in the cartridge from 0.5 nM up to 1.5 mM. Time sequences of RPI images of the spotted surface were analyzed by a custom MATLAB program (The

MathWorks, Natick, MA) to obtain the brightness of each spot as a function of time t and convert it into the total mass surface density of molecules $\sigma(t)$ (Supporting Materials and Methods) and into the mass surface density of the target molecules $\sigma_t(t) = \sigma(t) - \sigma_p(t)$, where $sigma_p(t)$ is the mass surface density of immobilized probe molecules measured before the addition of the target ssDNA in solution. The analysis of the hybridization curves was performed on $\sigma_t(t)$ traces obtained by averaging at least six spots with identical composition. The number surface density of probe, s_p, and target molecules, s_t, were obtained by dividing σ_p and σ_t by the corresponding molecular mass, respectively.

Analysis of surface hybridization by Langmuir model

The hybridization kinetics curves $\sigma_t(t)$ measured by RPI were analyzed either assuming a standard Langmuir model [25][69] or the non-Langmuir kinetic model described in Non-Langmuir Kinetic Model with Electrostatic Repulsion. The main assumptions of the Langmuir model are that the surface provides a finite number of independent binding sites (probes) holding at most one target molecule each, the binding sites are all equivalent, their properties do not change during the binding process, and there are no interactions between target molecules bound on adjacent sites. Under these assumptions, the time evolution of the fraction of hybridized surface probes $\phi(t)$ is given by:

$$\frac{\partial \phi(t)}{\partial t} = k_{on} c_t (1 - \phi(t)) - k_{off} \phi(t) \tag{3.1}$$

where c_t is the concentration of target ssDNA in solution and k_{on} and k_{off} are the kinetic rate constants for association (hybridization) and dissociation, respectively. In the experimental conditions explored in this study, the total number of immobilized probes is always much lower than the number of added targets in solution. This condition is ensured by the small size of the surface spots of probes and by a large enough sample volume. Therefore, c_t is assumed constant during the binding after each addition of sample in the measuring cartridge. Accordingly, for a concentration jump to c_t at $t = 0$, the solutions of Equation 3.1 are exponential growth functions with the form

$$\phi(t) = (\phi_{eq}(c_t) - \phi(0))(1 - e^{-k_{obs} t}) + \phi(0) \tag{3.2}$$

where

$$\phi_{eq}(c_t) = \frac{1}{1 + \frac{K_d}{c_t}} \tag{3.3}$$

is the equilibrium plateau value, which depends on the dissociation equilibrium constant $K_d = k_{off}/k_{on}$ of probe-target hybridization, and

$$k_{obs}(c_t) = k_{on} c_t + k_{off} \tag{3.4}$$

is the observed hybridization rate. The mass surface density, $\sigma_t(t)$, or the number surface density of target, $s_t(t)$, at a given time t after an increase of concentration c_t and the asymptotic equilibrium values σ_{eq} or s_{eq} are given by $\sigma_t(t) = \phi(t)\sigma_\infty$ and $\sigma_{eq} = \phi_{eq}\sigma_\infty$ or by $s_t(t) = \phi(t)s_\infty$ and $s_{eq} = \phi_{eq}s_\infty$, respectively, where σ_∞ and s_∞

are the mass surface density and the number surface density of target at saturation reached at large c_t.

Results

Effect of probe surface density on strength and kinetics of hybridization

We studied the kinetics of the hybridization process of ssDNA oligomers in solution (targets) with complementary strands (probes) immobilized on the surface of the RPI label- free biosensor. We focused on target oligomers with a length of 12 bases because they are long enough to provide rather large hybridization strengths and label-free signals and small enough to observe a clear dependence of their interaction parameters on different experimental conditions. We explored both the equilibrium constant and the kinetic rate constant for complementary probes with no additional linker or with an ss- or ds-linker strand, as shown in Figure 3.1. The injection into the RPI measuring cell of target ssDNA provides an increase of signal corresponding to the surface density of targets $\sigma_t(t)$ binding to the immobilized probes. Figure 3.2 reports label-free hybridization curves measured for probes with no linker (probe p1 in Figure 3.1) after the addition of targets in solution at the concentration c_t of 100 nM. The curves correspond to different spot families on the same RPI chip produced with different probe concentrations in the spotting buffer, from 2.5 µM up to 30 µM. All curves reached a stable asymptotic value of target surface density seq at a long time. However, both the asymptotic amplitude and the time required to reach such asymptotic value depend on the spotting concentration of probes. Like other label free biosensors, the RPI DNA sensor enables a direct measure of the mass surface density of probes σ_p. This is derived from the brightness of the spots before the addition of target in solution, taking as reference the brightness of the region outside the spots (Supporting Materials and Methods). The number of captured target strands is roughly proportional to the number of surface probes, although it remains smaller (Fig. S1), indicating that a fraction of probe strands on the surface are not accessible to the target. In the experiment reported in Figure 3.2, the hybridization yield ψ—that is, the fraction of active surface probes—was 30%. More generally, considering all the measurements reported in this work, the obtained ψ was overall 50% ± 20%, with a tendency of copolymer coating MCP4 to provide values of ψ slightly larger than MCP2.

The binding curves reported in Figure 3.2 also show a marked dependence of the hybridization kinetics on the surface density of probes. Smaller probe densities not only yield smaller amplitudes but also shorter times to reach the equilibrium. Under the hypothesis of an ideal interaction described by the Langmuir model, the hybridization curves should be well represented by simple exponential growth functions (Equation 3.2). In contrast, the measured binding curves progressively deviates from an ideal behavior with increasing σ_p (Supporting Materials and Methods). The fit with exponential functions with constrained initial slope (blue curves) shows that the binding slows down after the initial stage of the hybridization curve. This behavior suggests that the Langmuir interaction model does not represent well the hybridization kinetics between 12-mers for large surface densities of probes. Binding curves that are not well fitted by single exponentials are commonly observed by label-free biosensors and their interpretation typically involves different causes,

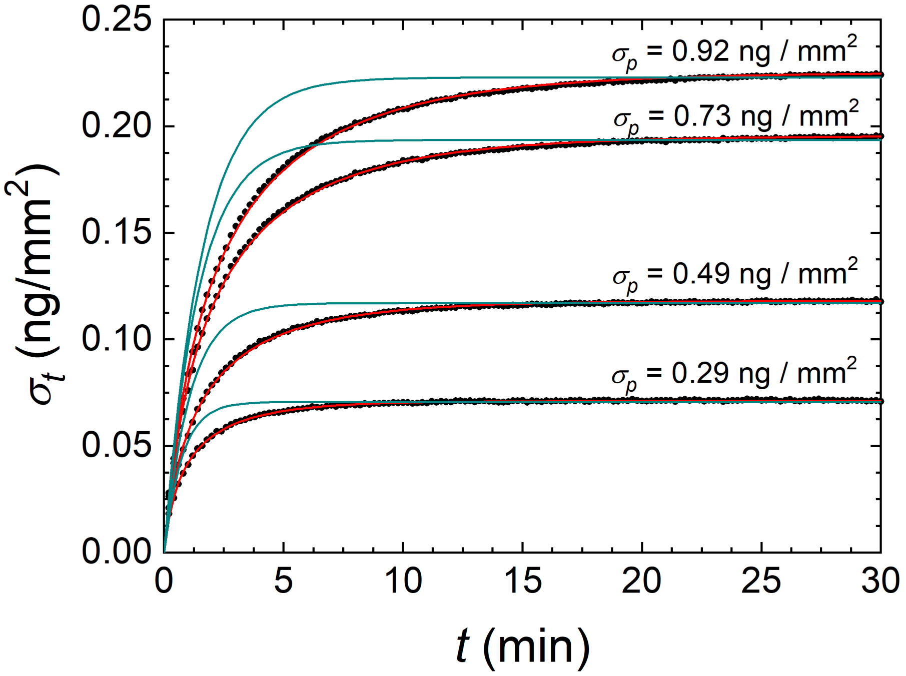

Figure 3.2: Hybridization kinetic curves measured by RPI. Binding curves (black dots) are expressed as mass surface density measured after the injection of 100 nM of target DNA in solution with 150 mM NaCl. The different curves refer to spots on the same RPI sensor with different surface density sp of DNA probes (no linker type), as reported in the figure. The DNA probes are immobilized via MCP2 copolymer. The continuous lines represent the fits with single exponential growth functions with initial slope constrained to that of the data points (blue) and numerical solutions of Equation 3.6 (red).

including heterogeneity of the surface binding sites or conformational changes of probes and targets [69]. A general approach is based on the assumptions of multiple Langmuir-like processes with different kinetics that sum up and yield multiexponential binding curves [70]. Here, we adopted a different strategy based on a deeper investigation of the scaling of the amplitudes and rates of the binding curves progressively increasing the concentrations c_t of target in solution. We performed sequential additions of target strands in solution, obtaining a target concentration c_t from 0.5 up to 1562.5 nM in the same RPI cell, and measured real-time hybridization curves for spot families with different spotting concentration of probes, hence obtaining a matrix of binding curves for different c_t and σ_p, as shown in Figure 3.3 a. The inspection of the data at intermediate target concentrations (central columns of plots in Figure 3.3 a) shows that the effect of σ_p on the amplitude and rates of the hybridization curves is qualitatively similar to that reported in Figure 3.2 . Remarkably, in this case all the measured hybridization curves are well fitted by exponential growth functions (black curves), even at large σ_p, because the dynamic range of each individual curve $\sigma_t(t)$ is typically smaller. This is equivalent to observing only a portion of the full curve $\sigma_t(t)$ from $\sigma_t = 0$ to $\sigma_{eq}(c_t)$, such as those in Figure 3.2 . The fit of the measured $\sigma_t(t)$ curves with exponential functions enabled us to extract amplitudes and rates as a function of c_t and for various values of σ_p. In this way, the matrix of binding curves of Figure 3.3 a was converted into two matrices, one for the asymptotic amplitudes $\sigma_{eq}(c_t, \sigma_p)$ and the other for the hybridization rates $k_{obs}(c_t, \sigma_p)$. The results are reported as plots at constant sp in Figure 3.3 , b and c (blue squares). All measured $\sigma_{eq}(c_t)$ (Figure 3.3 b) can be approximately fitted with a simple Langmuir model according to Equation 3.3 (continuous blue curves). The corresponding equilibrium dissociation constant K_d, indicated by the dashed lines in the figures, increases with the spotting concentration of probes, suggesting a weakening of hybridization strength with the increase of σ_p. However, at a closer inspection of the amplitude data, a small systematic deviation from the ideal behaviour can be observed: the fit tends to slightly underestimate the data points at concentrations c_t smaller than K_d and overestimate those for c_t larger than K_d. Residuals of the fit are reported in the Supporting Materials and Methods.

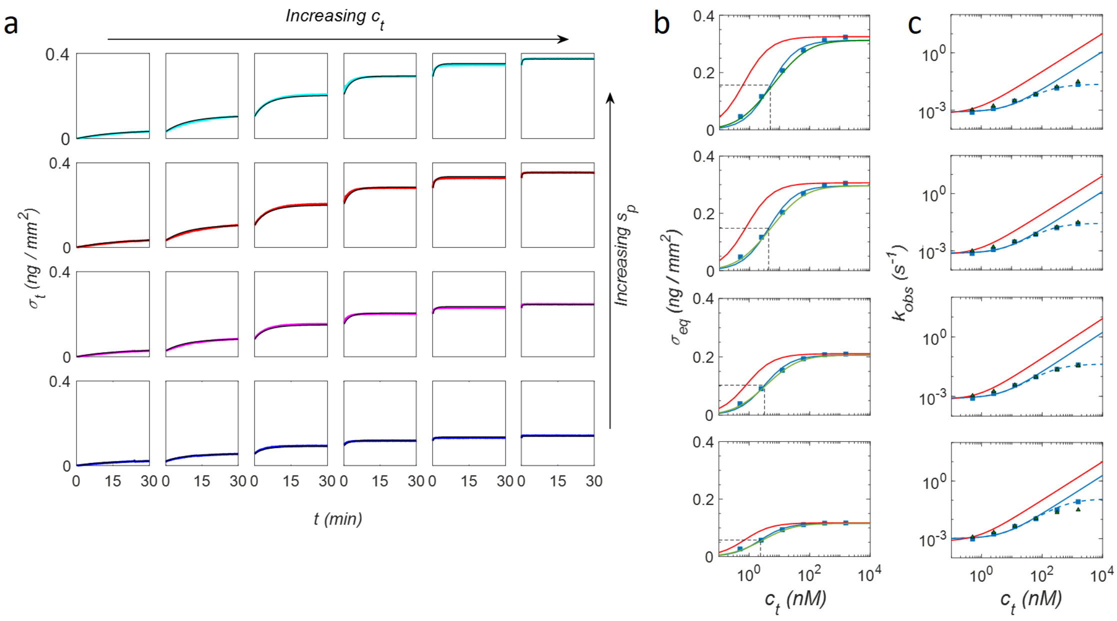

Figure 3.3: Hybridization kinetic curves at different target concentration and probe surface density. (a) RPI binding curves measured on the same sensor on spots with probe density $0.19 ng/mm^2$ (green), $0.24 ng/mm^2$ (purple), $0.38 ng/mm^2$ (red), and $0.41 ng/mm^2$ (cyan), for increasing concentrations of target strand in solution: (from left to right) 0.5, 2.5, 12.5, 62.5, 312.5, and 1562.5 nM. The black curves are fits to the data by single exponential growth functions. (b) Equilibrium asymptotic amplitudes and (c) kinetic rates obtained from exponential fits of the hybridization curves of panel a (blue squares). The blue lines are fits with amplitudes and rates obtained from a Langmuir model. The last two points at the largest concentrations are excluded from the fit of the rates. The green lines (b) and the green triangles (c) are the values obtained from the fit with the NLER model. The red lines represent the Langmuir behavior extrapolated from the NLER fit for $\Gamma = 0$. Average R^2-values for the equilibrium curves fits with Langmuir and NLER models reported in (b) are 0.987 ± 003 and 0.998 ± 0.001, respectively. The residual analysis is reported as Supporting Materials and Methods.

For what concerns the measured hybridization rates $k_{obs}(c_t)$ (Figure 3.3 c, blue squares and continuous curve), the analysis shows that the expected linear dependence on c_t (Equation 3.4) is confirmed up to about $c_t = 100nM$. The intercept of $k_{obs}(c_t \rightarrow 0)$, corresponding to k_{off}, appears to be constant and independent on σ_p, whereas the slope, corresponding to k_{on}, decreases with σ_p. The observed rates clearly deviate from the ideal linear dependence on c_t only for the largest concentrations of target, when the fraction of hybridized active probes ϕ is close to 1. Figure 3.3 c shows that the rates measured at $c_t > 100nM$ are smaller than the values extrapolated from the dependence of $k_{obs}(c_t)$ at smaller c_t, and the deviation from the linear scaling with c_t is progressively more pronounced at increasing σ_p. We assumed that, close to saturation, the remaining small fraction of available ss probes yield to a slower association kinetics, possibly because of their close proximity to other ss probes or hybridized duplexes [71]. This interpretation is consistent with the larger deviations from ideal linear scaling observed for larger σ_p and hence for smaller average probe-probe distance and is also consistent with the absence of this effect for the ds-linker probe type, in which a larger distance among neighbourhood probes is maintained by the larger volume and stiffness of the ds segment. It is worth noting that the inhomogeneous probe-probe distance obtained by random immobilization of DNA strands has been also proposed as the cause of the shape of the melting curves for surface-immobilized DNA [53]. To empirically describe the observed reduction of the apparent k_{on} at large c_t, we assumed a characteristic value of the fraction of hybridized probes $\phi = \phi*$ at which this phenomenon occurs. To estimate $\phi*$, the observed rate $k_{obs}(c_t)$ was fitted in the full range of concentrations with the following equation:

$$k_{obs}(c_t) = \frac{k_{on}C^*}{C^* + c_t} + k_{off} \tag{3.5}$$

where the parameter C^* represents the target concentration at which the apparent k_{on} displays a twofold decrease relative to the low concentration value. Equation 3.5 well fits the data reported in Figure 3.3 c (dashed lines).We converted C^* into the corresponding values of ϕ^* through Equation 3.3. Figure 3.4 a shows that ϕ^* decreases as a function of the saturation value of the number surface density of target strands s_∞ for the no linker and ss-linker hybridization types. The observed behavior is consistent with the interpretation of ϕ^* as the fraction of probe strands with a large enough distance from each other on the surface to grant free accessibility to the target strand. In each condition, an average fraction ϕ^* of probes displays a kinetics of hybridization unaffected by surface crowding. Therefore, this effect is not expected to affect the hybridization parameters for concentrations much lower than C^*. The analysis of the amplitude and rate data of Figure 3.3, b and c by a Langmuir model (Equations 3.1 and 3.5) enabled us to quantify the interaction parameters for the hybridization at different values of the number density of probes s_p. We obtained the kinetic rate constant for association, k_{on}, and dissociation, k_{off}, by a global fit of the amplitude and rate dependence on c_t with the constraint $K_d = k_{off}/k_{on}$. We repeated the analysis for the different probe types sketched in Figure 3.1and for the two copolymer coatings, MCP2 and MCP4. No appreciable difference was observed for the hybridization kinetics measured from the two coatings at similar s_p. However, the use of both coating types enabled us to slightly extend the overall range of s_p.

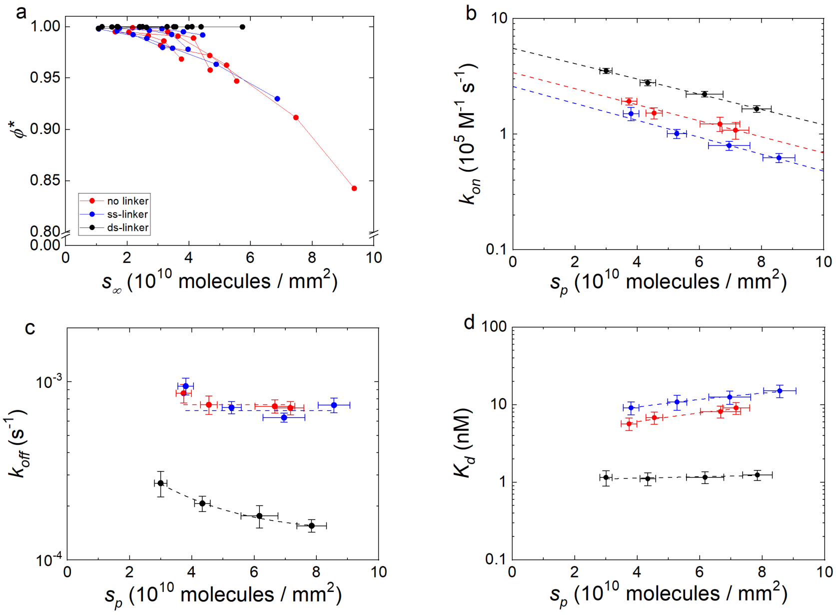

Figure 3.4: Dependence on DNA surface density of the equilibrium and kinetic parameters for hybridization. (a) Fraction of freely accessible probes ϕ^* as a function of target surface density s_∞ at saturation for all four experiments and all probe types. Kinetic rate for association (b) and dissociation (c) obtained for different probe types. The dashed lines represent fits to the data with the same color: constant values (c, red and blue) or exponential decays (all the curves of b and black curve in c). (d) Dissociation equilibrium constant for different probe types. The dashed lines are linear fits shown to guide the eye. In (b)–(d), the data points are average values of four experiments, and the vertical error bars are the standard deviations. Horizontal error bars are relative errors estimated from mutliple RPI experiments with the same spotting concentrations of probes. In all panels, the colors refer to different probe types, as indicated in (a).

As reported in Figure 3.4, b and c, we found similar values of the kinetic constants for no linker and ss-linker probes and larger k_{on} and much smaller k_{off} for ds-linker. We also observed a systematic decrease of k_{on} on increasing the surface density s_p for all probe types. In contrast, k_{off} is nearly constant in the case of no linker and ss-linker probes. Therefore, the increase of K_d with s_p, reported in Figure 3.4 d, primarily results from k_{on} in these cases. Differently, for the ds-linker probes, we obtained much smaller values of K_d and hence a stronger hybridization strength, weakly dependent on s_p. The k_{off} of the ds-linker slightly decreases with s_p, suggesting an increasing probability of rebinding of the target on the immobilized probes before diffusing away from the surface layer [72]). We ascribed the peculiar behavior of the ds-linker probes primarily to the presence of the additional coaxial base stacking interaction due to the double strand adjoining the probe sequence, which can be as large as 1.5 kcal/mol in the considered experimental conditions [73][74]. In contrast, the observed decrease of k_{on} with s_p reported in Figure 3.4 b is primarily ascribed to an additional effect originating from the electrostatic repulsion between NA strands, as discussed below.

Non-Langmuir kinetic model with electrostatic repulsion

The interaction between a target ssDNA and its complementary strand immobilized on a surface is known to be affected by electrostatic repulsion [54][55][58]. In particular, this effect is expected to increase with the overall surface density of NA. Consequently, the mean electrostatic repulsion in the proximity of the surface can increase during the hybridization, which brings more NAs, and hence more charges, onto the surface. This condition yields to an apparent reduction of the hybridization strength at equilibrium, which depends on the fraction of hybridized probes on the surface. Therefore, the hybridization process could show deviations from a simple Langmuir model even at small target concentrations c_t and fractional coverage of active probes ϕ.

A simple theoretical solution of the equilibrium condition has been proposed by Vainrub and Pettitt (VP) [31] introducing a meanfield free-energy penalty for hybridization proportional to the surface fraction of bound active probes ϕ and accounting for an effective electrostatic repulsive potential confined in a thin surface layer. The model has been further refined by Halperin, Buhot, and Zhulina (HBZ) [32], allowing for a variable thickness of the repulsive layer and hence also describing the hybridization at low ionic strength. The notion of a repulsive potential originating at the surface of DNA biosensors and DNA arrays enables computing more accurate equilibrium solutions for the hybridization process [34][54][75]. In contrast, an effective general model to account for the measured kinetics of hybridization is still missing. An influence of the surface probe density on the kinetics of DNA hybridization has been often observed in biosensor measurements [29], and a few studies have proposed theoretical frameworks accounting for electrostatic repulsion [58][71].

On the basis of the VP and HBZ equilibrium models and of the previous studies on kinetics modeling, we developed a simple approach to account for the effect of a repulsive potential in the proximity of the probe layer on the kinetics of hybridization. Figure 3.5 a shows a schematic representation of the model: the accumulation of negative net charge on the surface yields to a repulsive electrostatic potential, which, in a simple approximation, we assume to have a step-like profile with a characteristic thickness h. At a distance larger than h from the surface, the potential is that of the bulk solution. The model also comprises the notion of a dissociation constant k_{off} substantially independent from the probe surface density, as suggested by the experiments shown in Figures 3.3 and 3.4. Under these assumptions, the time evolution of the surface fraction of hybridized probes, for $\phi < \phi^*$, is described by

$$\frac{\partial \phi(t)}{\partial t} = k_{on}^{0} c_t e^{-\Gamma(1+n\phi)}(1-\phi) - k_{off}\phi \tag{3.6}$$

where k_{on}^{0} is the association kinetic rate in the ideal condition of negligible repulsive interaction and G represents the electrostatic penalty associated with entry of charged ssDNA target into the probe surface layer, as predicted in the VP and HBZ models. The parameter n is the ratio between the length of target and probe strands expressed in number of bases and accounts for the fact that, between the conditions of $\phi = 0$ (only probe strands) and $\phi = 1$ (all active probes hybridized with the target strands), the surface charge increases by a factor $1 + n$. We named this kinetic model non-Langmuir model with electrostatic repulsion (NLER). It must be noted that the equilibrium solutions of Equation 3.6 are formally identical to the surface hybridization isotherms predicted by both the VP and HBZ models and that the NLER model extends them with the treatment of kinetics. Equation 3.6 differs from a Langmuir kinetic model (Equation 3.1) only for the exponential term $e^{-\Gamma(1+n\phi)}$, which accounts for the electrostatic repulsion experienced by the target strands in the proximity of the surface with the immobilized probes. Remarkably, this exponential term can be considered either as a correction coefficient applied to k_{on}^0, hence reducing the effective association time because of the repulsive free-energy barrier, or equivalently as a term applied to the concentration c_t, hence reducing the amount of target DNA effectively entering the probe surface layer. Equation 3.6 also indicates that the effect of the repulsive interaction yields a behavior different from a simple Langmuir process for values of the product $\Gamma \cdot n$ close to or larger than 1, a condition in which the surface density of charges changes significantly with $\phi(t)$. Considering the probe schemes shown in Figure 3.1, the value of parameter n is 1 for the no linker type, 1/2 for the ss-linker, and 1/3 for the ds-linker. Notably, even if the kinetics becomes indistinguishable from a Langmuir process for small n, the repulsive interaction can still be relevant if Γ is non-negligible, and both the observed association rate constant and the equilibrium constant effectively incorporate the term $e^{-\Gamma}$.

Numerical solutions of Equation 3.6 well describe the measured hybridization curves with a minimal set of parameters. In particular, Equation 3.6 describes both the non-exponential shape of the hybridization kinetic curves for large c_t jumps, as shown in Figure 3.2 (red curves), and the dependencies of ϕ_{eq} and k_{obs} on c_t, like those reported in Figure 3.3. Figure 3.5 shows that $\phi(c_t)$ and $k_{obs}(c_t)$ calculated from Equation 3.6 differ from those obtained with the Langmuir model. The amplitudes $\phi_{eq}(c_t)$ of the simulated hybridization curves are shifted at larger c_t and increase with a smaller slope for larger values of Γ. Interestingly, a similar behavior can be also obtained by standard general models accounting for a distribution of interactions with different K_d or by the widely used Sips isotherm [60][76]. Analogously, the observed rates $k_{obs}(c_t)$ display a progressively weaker dependence on c_t for larger values of Γ. We used the numerical solutions of Equation 3.6 to perform a two-dimensional fit of the measured hybridization curves $\sigma_t(t)$ at different c_t and s_p (Figure 3.3 a) to extract the value of Γ, k_{on}^0, and k_{off}. The green curves in Figure 3.3 b and the green triangles in Figure 3.3 c report the fits to $\sigma_{eq}(c_t)$ and $k_{obs}(c_t)$, respectively. As a comparison, the red curves in Figure 3.3, b and c report the amplitudes and rates extrapolated to the absence of repulsive potential at the surface, hence for $\Gamma = 0$.

In this ideal condition, Equation 3.6 describes a Langmuir process with kinetic rates k_{on}^0 and k_{off} and thus with $K_d^0 = k_{off}/k_{on}^0$. The behavior of both the equilibrium amplitudes and the observed rates become increasingly non-Langmuir as the surface density of probes increases. The shift at larger concentrations either for the amplitude plots (Figure 3.3 b) or the rates (Figure 3.3 c) provides the value of the term G in this process. The values of Γ are consistent with a liner scaling with s_p (Fig. S2; [32]). Therefore, we assumed

$$\Gamma = \gamma s_p \tag{3.7}$$

and for each experiment, we fitted the amplitude and rate data at different c_t and s_p

with only one value of k^0_{on} and one value of γ. In the case of the no linker and ss-linker probe types, koff was also assumed to be independent of s_p, whereas it was assumed to provide a linear dependence on s_p for the ds-linker probes. The average values of the kinetic parameters obtained from four experiments for each of the three probe types considered are reported in Table 3.2. The obtained kinetic rate constants are very similar for the no linker and the ss-linker probes and show a larger k^0_{on} and a smaller k_{off} for the ds-linker case. The value of Γ at a standard surface density of $s_p = 10^{11} mm^2$ is of the order of 1 for all probe types and shows a minimal value for the dslinker type. Indeed, the value of Γ is expected to primarily depend on different physicochemical variables affecting the charge interactions between NAs. A deeper insight on this dependence is provided by the study of the hybridization at different ionic strengths.

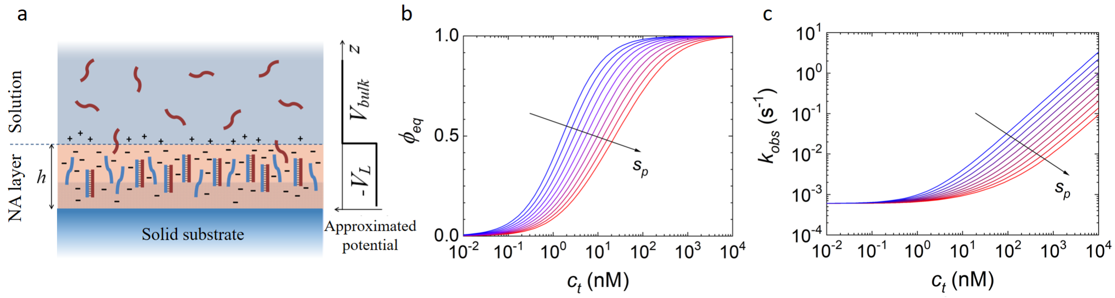

Figure 3.5: Schematic representation and numerical solution of the NLER model. (a) The surface region is rich in NA probes (blue) immobilized on the copolymer coating (shaded area) and hence provides a negative net charge, which further increases upon hybridization with the target strands (dark red). The electrostatic potential is approximated by a step function having a value lower than that of the bulk solution up to a distance h from the RPI solid surface. (b) Fraction of hybridized probes at equilibrium and (c) kinetic rate computed for different surface densities of probes, from $10^{10} mm^2$ (blue) to $10^{11} mm^2$ (red). The curves were computed with fixed kinetic parameters $k^0_{on} = 2.3 \cdot 10^4 nM^{-1} s^{-1}$ and $k_{off} = 7.2 \cdot 10^{-4} s^{-1}$ and for $\Gamma = \gamma s_p$, with $\gamma = 2 \cdot 10^{-11} mm^2$.

Probe type	Probe sequence	Γ	$K^0_d (nM)$	$k^0_{on} (10^5 M^{-1} s^{-1})$	$k_{off} (s^{-1})$
No linker	p1	1.2 ± 0.1	2.2 ± 0.6	3.7 ± 0.7	7.7 ± 0.6
ss-Linker	p2	1.3 ± 0.3	3.0 ± 1.0	3.0 ± 1.0	6.5 ± 0.8
ds-Linker	p2 + cp2	0.8 ± 0.3	0.3 ± 0.1	6.4 ± 0.7	1.7 ± 0.5

Table 3.2: Measured Parameters for DNA Hybridization at 150 mM NaCl. Γ values obtained Obtained for $s_p = \cdot 10^{11} mm^{-2}$.

Effect of ionic strength on the hybridization kinetics

The role of ionic interactions can be in general modulated by changing the solution concentration of salt, which provides the counterions that screen the chain ions. In particular, the hybridization can be partially or totally inhibited at large surface densities of probes and low concentrations of salt in solution [55]. To quantitatively account for the influence of ionic strength on binding kinetics, we investigated the hybridization curves for solutions containing different salt concentration, ranging from below to above the value of ionic strength $I_s = 150mM$, which best approximates the physiological conditions. In general, we observed an increase of the hybridization rates with I_s, and such dependence is more pronounced at low surface density of probes. Figure 3.6 reports the observed hybridization rates k_{obs} as a function of s_p obtained by exponential fits of the hybridization curves $\sigma_t(t)$ measured for different ionic strengths at the same target concentration $c_t = 12.5nM$.

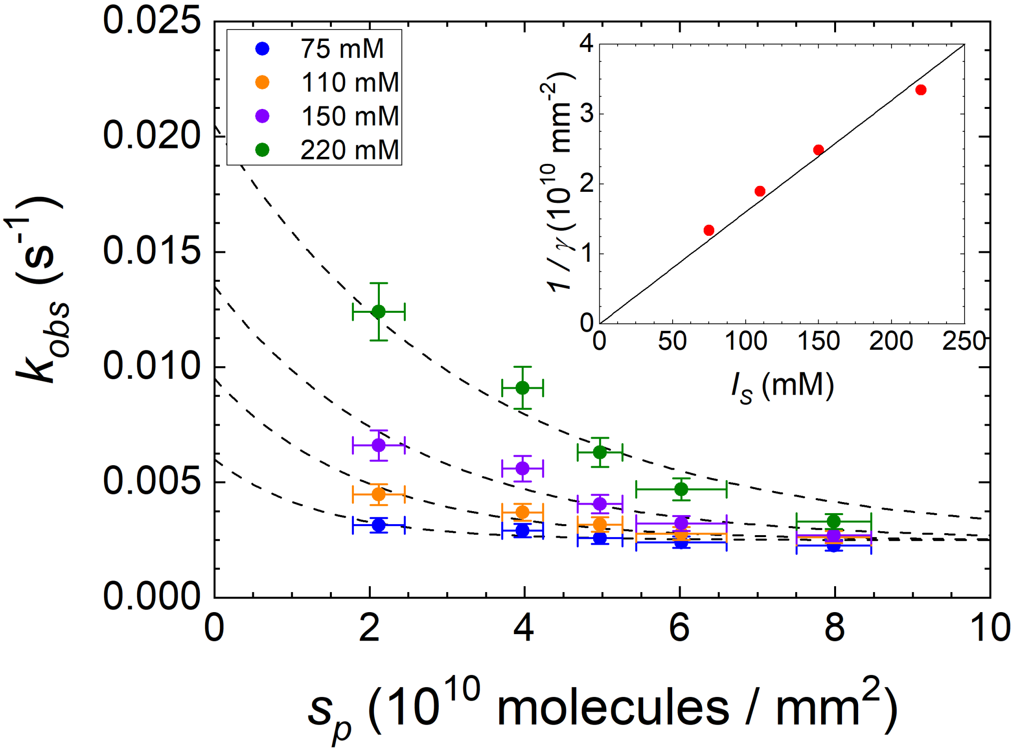

Figure 3.6: Dependence of the measured kinetic rates for hybridization on the ionic strength. RPI binding curves were measured at a target concentration of 10 nM for different surface densities of probes (no linker type) and for different ionic strength, as indicated in the figure legend. The vertical error bars represent the standard deviation of observed rates calculated from three experiments at 150 mM NaCl. Horizontal error bars are relative errors estimated from multiple RPI experiments with the same spotting concentrations of probes. The dashed curves are fits with exponential decay functions, constrained to the same asymptotic value at large s_p and to an initial value at $s_p = 0$ linearly increasing with the ionic strength. Inset: scaling of the reciprocal of the characteristic surface γ with the ionic strength obtained from the exponential decay fit of k_{obs} (red dots) and linear fit with slope $16 \cdot 10^{-10} mm^{-2} M^{-1}$ (black line).

For all salt concentrations, the measured rates constantly decrease with s_p and tend to converge to similar values at large s_p. In the explored regimes, the values of k_{obs} span about one order of magnitude, from the smallest values measured at large probe density and small salt concentrations up to those extrapolated for small s_p and large I_s. This confirms that the hybridization kinetics can be controlled by either the surface density of probes or the salt concentration. The observed behavior of k_{obs} as a function of surface probe density at different Is is compatible with Equation 3.6. The data reported in Figure 3.6 were fitted with curves $k_{obs}(s_p)$ obtained for Equation 3.6 assuming a linear dependence of k^0_{on} as a function of I_s. Considering the range of salt concentrations explored in this study, the linear dependence of k^0_{on} is consistent with previous measurements of kinetic rate constants for hybridization of oligomers [77][78]. The obtained dependence of the characteristic value of probe density $1/\gamma$ as a function of I_s is shown in the inset of Figure 3.6. The values are compatible with an inverse proportionality between γ and I_s, in agreement with the expected dependence of the free-energy barrier with ionic strength. A deeper insight on the origin of the electrostatic repulsive barrier at the surface functionalized with ssDNA probe is given by the analysis of the dependence of the parameter γ on the physical features of the probe layer. According to the HBZ model, the electrostatic penalty γ takes the following form [32]

$$\gamma = 8\pi N_p N_T l_B \frac{r_D^2}{h} \tag{3.8}$$

where N_P and N_T are number of bases for probe and target strand, respectively; l_B is the Bjerrum length; r_D is the Debye length; and h is the estimated layer thickness. Given the proportionality of r_D with $I_s^{-1/2}$ [79], the value of γ is expected to scale with I_s^{-1}, in agreement with the measured values reported in Figure 3.6 (inset).

Discussion

Strength of the electrostatic repulsion

The analysis of hybridization kinetics measured by RPI confirms the relevant role of electrostatic repulsion in the observed reduction of hybridization strength on a surface. This effect is ascribed to a free-energy barrier between the free solution state and the bound state of ssDNA targets. In agreement with the VP and HBZ models, the proposed NLER kinetic model adopts a single parameter, Γ, to account for such surface repulsion effect. According to our analysis based on Equation 3.6, the value of Γ can be experimentally extracted through suitably designed experiments in a range of probe and target lengths, probe surface densities, and ionic strengths in which the surface repulsion provides a modification of the hybridization kinetics relative to a simple Langmuir model.

However, according to the proposed NLER model, the electrostatic free-energy barrier can be relevant even in conditions in which the surface hybridization is indistinguishable from an ideal Langmuir process, hence contributing to the observed weakening of the hybridization strength on a surface [51][60]. The quantification of the electrostatic repulsive barrier originating at the surface of a DNA biosensor has been addressed in previous works. In [32], it was shown that the data from [60], taken for a 25-mer hybridization at 1 M NaCl, are consistent with a value of $\Gamma = 3$ at $s_p = 10^{11} mm^2$, whereas a value of about $\Gamma = 11.6$ would be expected from Equation 3.7 and 3.8. In our study, we obtained a value of $\Gamma \approx 1.2$ for 12-mer hybridization at 150 mM NaCl and $s_p = 10^{11} mm^2$ (Table 3.2). Considering only the expected scaling of Γ with $N_P N_T$ and with I_s^{-1} (Equation 3.8), which in this case roughly compensate, our values of Γ remains from 3 to 10 times smaller than those estimated in [32]. Different hybridization regimes were proposed in [55] depending on the strength of the surface repulsion: pseudo- Langmuir (PL), suppressed hybridization (SH), and no hybridization. In [58] it was estimated that for a 20-mer directly immobilized on a surface the PL-SH and the SH-no hybridization borders can be placed at $\Gamma = 2.5$ and $G = 13$, respectively. The results of our study are coherent with the conditions between an apparent Langmuir behavior at small s_p (PL) and a more complex non-Langmuir kinetics (SH), in which the repulsive barrier changes significantly during the hybridization. Therefore, a value of Γ around 2.5 would be expected. We explored a range of s_p from 2 to $15 \cdot 10^{10} mm^2$, corresponding to a range of Γ of 0.2–1.8 for the no linker and ss-linker probe types (Table 3.2), which are thus similar to the estimated threshold, although slightly smaller. A major difference between our experiments and those of [60] and [55] is that we immobilized the DNA probes on a three-dimensional (3D) copolymer coating forming a thin hydrogel layer [80], instead of a compact monolayer obtained by direct binding of DNA to the sensing surface. Therefore, from Equation 3.8, the apparent discrepancy in the value of Γ can be attributed to a larger thickness h of the probe surface layer in our case.

Thickness of the surface NA layer

Because all other parameters in Equation 3.8 are known or can be easily estimated, we can derive the value of the effective thickness h of the region in which the repulsive potential is confined (Figure 3.5 a). In the NLER model, the profile of the repulsive potential along the z coordinate perpendicular to the surface is simply approximated by a step function that remains constant within a thickness h and then decreases sharply to the bulk value of the solution. It must be noted that the actual potential will instead change gradually with the distance from the surface [58]; hence, the parameter h represents the effective thickness of the step-like potential providing the same behavior of the real system. For ionic strengths around physiological conditions, the potential is expected to decrease to the bulk solution value within a few nanometers above the NA layer thickness [58][78].

In contrast, if the NAs are immobilized on a 3D polymer coating, the z-profile of the repulsive potential is expected to be smoother. In the experiments performed in this study, the ssDNA probes were immobilized on the biosensor surface through a multifunctional polymeric coating capable of swelling in aqueous buffer, forming an hydrogel layer with a thickness of 10 nm when hosting ss- or dsDNA [80]. Therefore, h is expected primarily to depend on the polymer thickness h_c and on the NA layer thickness h_p as $h = h_c + h_p$. The characteristic size of the 12-mer ssDNA can be estimated assuming a persistence length of 2.5 nm and a self-avoiding polymer scaling yielding $h_p \approx 5nm$ [81]; hence, h is expected to be within 15 nm. In contrast, the value of h obtained from Equation 3.8 for $N_p = N_t = 12$ is 125 nm[a], hence much larger than the expected thickness of the 3D probe layer on the surface. Notably, a similar discrepancy between the measured values of Γ and those estimated by Equation 3.8 was mentioned also in [32], as discussed above. Here, we propose two corrective factors to reconcile the experiments and the theoretical model. A first correction is performed considering that not all the phosphate groups of the ssDNA

---

[a] Compared with Debye length of ¡1 nm for this system

bring a unitary negative charge. This effect is accounted by the so-called Manning condensation [58] and yields to an effective ssDNA charge of 55% of the fully ionized molecule. Remarkably, in [58] it was reported that this charge renormalization provided the best agreement of a modified Poisson-Boltzmann model with experimental data, hence implying a complete exclusion of mobile counterions from the DNA surface layer. Because the number of charges enters Equation 3.8 through the length of both probe and target DNA, this correction yields a 30% reduction of the calculated Γ for a given h. A second correction that further reduces the apparent value of Γ is obtained considering that in our experiments, not all the surface DNA probes are available for hybridization, as indicated by the yield ψ extrapolated from the saturation of the probes at large concentration of target strands. Therefore, only that fraction of probes undergoes a twofold increase of charge, whereas all the probes, not just the hybridized fraction, are responsible for the overall electrostatic repulsion at the surface.

From the inspection of Equations 3.6 and 3.8, a constant additive term in s_p that is not multiplied by $(1 + n\phi)$ accounts for an increase of the experimentally observed value of Γ by a factor $1/\psi$, corresponding to a threefold increase for $\psi = 30\%$ as for the data in Figure 3.2. Coherently, the value of h in Equation 3.8 yielding such larger values of Γ is three times smaller. Together with the first correction, an overall reduction of h of about a factor of 10 is obtained, hence leading to a thickness of the copolymer layer of $h_c = h - h_p = 8$ nm, in agreement with previous measurements [37][**?**]. Interestingly, this result suggests that smaller values of Γ, hence a reduction of the surface repulsion, can be theoretically obtained for much larger thickness of the 3D functional layer. However, in optical- label-free biosensors, distributing the probe molecules at constant s_p along a large thickness can yield to a decrease of signal response upon hybridization; hence, an optimal intermediate condition can be preferred.

Origin of the surface weakening of hybridization

The analysis of the hybridization at different surface probe densities enables to extrapolate the expected kinetics and equilibrium strength at very low values of s_p, when the repulsive electrostatic barrier vanishes, according to Equation **??**. In this case, the kinetic rate constant for association is given by k^0_{on}, whereas k_{off} is found to have a much weaker dependence on s_p, for the no linker and ss-linker probe types. Accordingly, the dissociation equilibrium constant at very low s_p is given by $K^0_d = k_{off}/k^0_{on}$. Table 3.2 reports these values for the studied hybridization schemes. It is interesting to compare the obtained values of K^0_d with those for both probe and target ssDNA freely diffusing in solution that can be computed by standard thermodynamic approaches [82][9][83]. Estimates for p1-t1 and p2-t1 hybridization in solution are very similar and lie around -15 kcal/mol, corresponding to K_d of 0.01 nM at the temperature of 23°C used in our experiments. The available algorithms do not explicitly include the stabilizing effect of coaxial stacking present in the ds-linker probe type. Nonetheless, reported values for this effect [74] can account for an additional 10-fold reduction in K_d, in line with our observations. Therefore, the estimated dissociation constant for the 12-mer hybridization in solution overall remains much lower than K^0_d reported in Table 3.2. As regards kinetics, theoretical treatments are much less developed. On the basis of a set of FRET experiments

[59], the predicted hybridization rate in solution for similar experimental conditions is equal to $7 \cdot 10^6 M{-}1s^{-1}$, hence about one order of magnitude faster than what obtained for the surface probes measured in our work. Remarkably, as discussed above, a hybridization yield $\psi < 1$ suggests the presence of a constant additive term in s_p, which provides an equivalent correction factor $e^{\Gamma(1-\psi)/\psi}$ to the apparent association constant k^0_{on} obtained from the fit of the binding curve with Equation 3.6. For $\Gamma = 1.2$ and $\psi = 30\%$, this correction factor is more than one order of magnitude, hence leading to values of k^0_{on} and K^0_d more similar to those estimated for hybridization in solution. Despite the major role of electrostatic repulsion in surface hybridization, other factors can contribute to the weakening of the hybridization strength relative to the same interaction in solution. The possible sources include strand-surface interaction and interstrand interaction [34]. We observed a significant non-Langmuir behavior even in the case of immobilized strands at a distance larger than their expected lateral occupancy, hence confirming that the origin of the non-Langmuir behavior is not the interstrand interaction and that the extrapolation of the hybridization strength at low s_p is not affected by possible interstrand interaction.

In a previous work, we showed that a very weak interaction with the surface can induce a strong decrease of affinity for hybridization because of a simple competition effect [25]. The copolymer coating used in this work is highly hydrophilic and nonionic. Therefore, electrostatic or van der Waals interactions are not expected to play a major role. However, we cannot exclude the formation of transient hydrogen bonds. Previous works have shown that immobilized DNA remains largely oriented on this copolymer coating, in agreement with the notion of negligible interactions [84]. A large effect of very weak interactions with the surface on the affinity and kinetics of hybridization is a peculiar feature of the pairing between complementary NAs, in which the binding sites are spread along the entire molecular length. The temporary unavailability of a single base of the probe strand does not prevent the hybridization but provides a strong effect on hybridization kinetics. Accordingly, on the one hand, the presence of a polymeric coating with a 3D distribution of conjugation sites can increase the thickness h and hence reduce Γ; on the other hand, it can provide more chance of weak interactions, even simply steric, with the immobilized DNA probes, hence reducing the hybridization strength with the target in solution. On the basis of these arguments, an optimal surface functionalization with DNA probes can be achieved by combining the ds-linker probe type with a conjugation layer providing suitable thickness, 3D distribution of conjugation sites, and minimal interaction with the ssDNA probe.

Conclusions

The results of this study confirm that the electrostatic repulsion is a major source of the well-known weakening of DNA hybridization on a surface in a wide range of conditions. Despite the strong effect on the equilibrium and kinetics of hybridization, a standard analysis of the binding curves can show only small deviation from an ideal Langmuir behavior. However, a two-dimensional analysis of the hybridization curves as a function of both c_t and the surface probe density s_p more easily reveals a non-Langmuir dependence coherent with a repulsive potential proportional to the overall density of NA bases on the surface, according to Equation 3.6. These results have direct consequences on the design of DNA arrays. In practice, in the explored conditions, the label- free signal due to hybridization is always found to increase with the surface density of probes. Therefore, for the purpose of assay design, larger values of s_p enable us to achieve larger signals at equilibrium for any concentration of target c_t. However, the kinetics of hybridization can be strongly reduced at large s_p by two phenomena: the surface electrostatic repulsion and the crowding of immobilized probes. The latter effect only occurs for large enough fractional coverage ϕ of probes, hence typically close to saturation, whereas the electrostatic penalty can be effective at any values of ϕ and c_t and directly contributes to reduce the observed equilibrium constant for surface hybridization. Accordingly, a correct absolute quantification of target concentration derived from the assay response should necessarily account for the weakening and slowing down of hybridization, which both depend on the surface density of probes.

Interestingly, the large net charge of NA can be considered as functional to preserve a large specificity of hybridization even at large concentrations. The electrostatic repulsion between two NA strands in solution effectively increases the threshold of the attractive strength required to form a stably paired complex, hence the minimal number of consecutive complementary bases. Indeed, uncharged DNA mimics such as peptide NAs or phosphorodiamidate morpholino oligomer, although they may provide larger affinities for hybridization with DNA in controlled conditions, also typically display the lower solubility and larger nonspecific binding that brings to relevant background signals when used in assays applications [52]. Analogously, it can be argued that the enhanced repulsion originating in surface- based DNA biosensors favors the specificity of molecular recognition at the cost of sensitivity relative to DNA probes freely diffusing in solution.

From the results of this study, we can estimate a DNA concentration in solution at which the electrostatic repulsion starts inducing non-negligible effects on the hybridization kinetics. From Equation 3.6, we can assume that the hybridization behaviour deviates from a Langmuir model for $\Gamma > 0.1$. This corresponds to s_p on the order of $10^{10} mm^{-2}$ for the probe strands used in this work. Considering a 3D distribution of the probes over a thickness of 13 nm, the corresponding volume density is $8 \cdot 10^{17}$ molecules in 1 mL or 5 mg/mL for a 12-mer DNA probe. As a comparison, the average concentration of DNA within the nucleus is of the order of 10 mg/mL [85], with large density fluctuations in space. Therefore, the conditions achieved on the surface of DNA biosensors and the corresponding effects on hybridization can be rather common in nature and can play a biological role in the cellular nucleus. Overall, the kinetic modelling of these elementary DNA-based interactions is expected to guide the design of more complex functional structures immobilized on a surface and provide a pathway for kinetic optimization of DNA nanomachines. The results of this work are also expected to stimulate further studies aimed at extending the modelling to a wider range of conditions, e.g., including the effect of divalent cations and DNA structures.

Conversion of reflected intensity into surface density of molecules

The apparatus and the analysis algorithm of the RPI method was described in[38]. Briefly, the spotted surface of the glass sensor was illuminated by collimated LED light at 450 nm and sequences of images of the reflected light were acquired by a CCD camera. The conversion of the brightness of the RPI image pixels of the spot region, u_s, and outside the spots, u_0, into surface density was performed according to:

$$\sigma(t) = \sigma^* \sqrt{\frac{u_s(t)}{u_0} - 1} - \delta\sigma \tag{3.9}$$

Amount of hybridized DNA target strands at equilibrium

Single strand DNA oligomers with a length of 12 bases (probe type p1 in Table 3.1 and Figure 3.1) were immobilized on the surface of a RPI label-free sensor. The injection into the RPI measuring cell of complementary target ssDNA provided an increase of the measured surface density of molecules due to hybridization of the surface probes with the targets. The real-time hybridization curves were acquired from spots with different number surface density of probes s_p, after the addition of targets in solution at the concentration c_t =100 nM. The measured curves are reported in Figure 3.2. All curves reached a stable asymptotic value of target mass surface density σ_{eq} at long time. The asymptotic amplitude of each curve, converted from σ_{eq} into the number surface density of target at equilibrium s_{eq}, is reported in Figure 3.7 as a function of s_p. The number of captured target strands was roughly proportional to the number of surface probes. The hybridization yield ψ, that is the fraction of surface probes hybridized with the target, was about 30%, indicating that a fraction of probe strands on the surface were not accessible to the target.
In the framework of the NLER kinetic model described by Equation 3.6, the asymptotic amplitude reached at saturation of the probe sites, i.e. at large c_t, remains proportional to the surface density of probes. However, increasing the surface density of probes, the apparent equilibrium constant for dissociation also increases (see Figure 3.5b), hence the saturation is reached at larger values of c_t. Accordingly, at constant c_t, the observed asymptotic amplitude deviates from a linear scaling with s_p, as shown by the dashed line in Figure 3.7, obtained from the numerical solutions of Equation 3.6.

Fit of the hybridization kinetic curves with free exponential growth functions

The increase of surface density of targets $\sigma_t(t)$ binding to the immobilized probes can show a non-ideal behaviour at large surface density of probes σ_p. Figure 3.8 reports $\sigma_t(t)$ measured for probes with no linker (probe p1) after the addition of targets in solution at the concentration c_t of 100 nM. Under the hypothesis of an ideal interaction described by the Langmuir model, we fitted the hybridization curves with simple exponential growth functions without constraints (Equation 3.2). As shown in Figure 3.8, only the binding curve corresponding to the spots with the smallest σ_p was rather well fitted by an exponential growth (blue curves), and the deviation progressively increases with increasing σ_p. This behaviour suggests that the Langmuir interaction model does not represent well the hybridization kinetics between 12mers for large surface densities of probes.

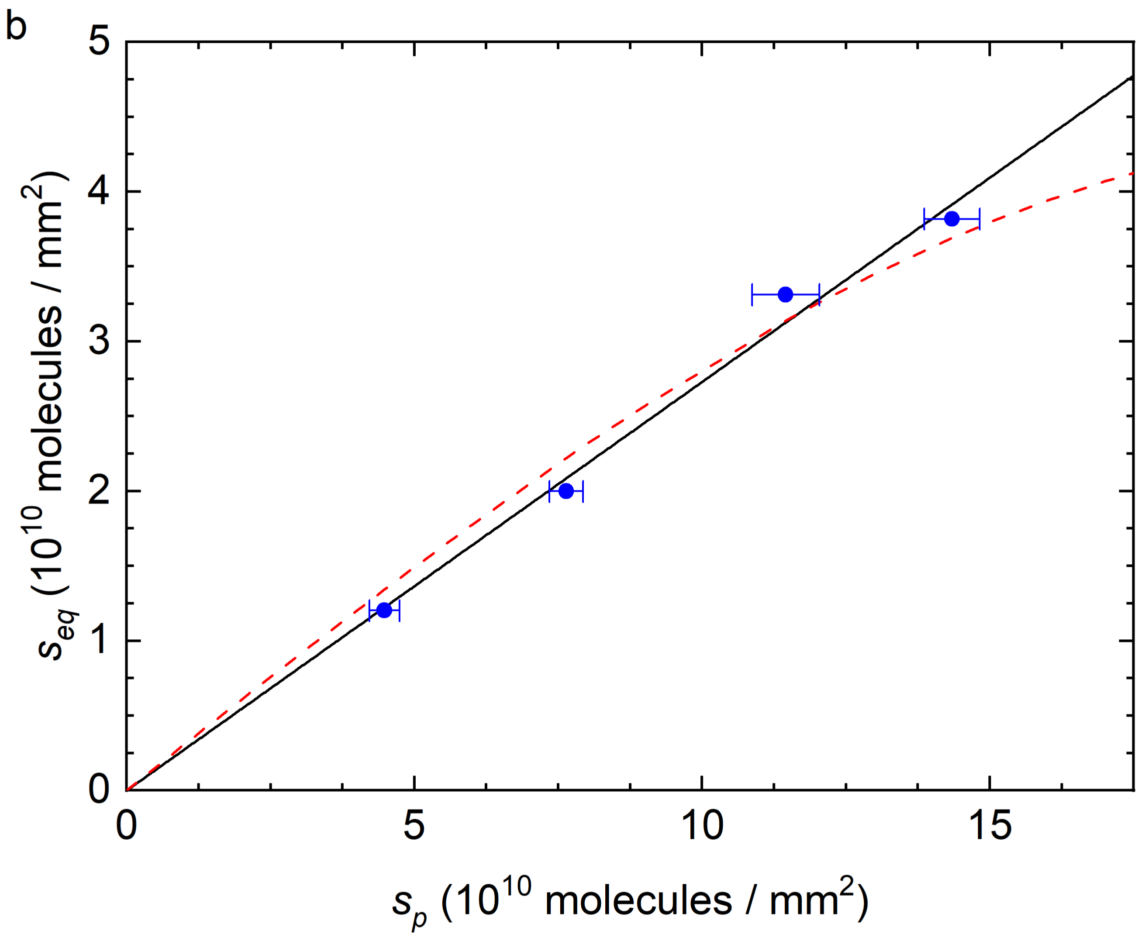

Figure 3.7: Scaling of hybridization equilibrium amplitude with surface probe density. The blue dots represent the equilibrium amount of DNA target strands measured from spots with different surface density s_p of probes (no linker type). The corresponding binding curves are reported in Figure 3.2. The black line is a linear fit with slope 0.27. The dashed line is the dependence computed from the numerical solution of Equation 3.6 with $\Gamma = 0.9$.

Increase of electrostatic repulsion with probe surface density

Coherently with previous models describing the equilibrium behaviour of DNA surface hybridization [32][31], the NLER kinetic model also accounts for an electrostatic repulsion increasing with the surface density of probes. The hybridization process becomes progressively non-Langmuir as the surface density of probes increases. This behaviour is accounted for by the parameter Γ in Equation 3.6. If large enough, the value of Γ can be estimated from the dependence of the amplitudes and rates of the hybridization curves with c_t at constant probe density s_p. Figure 3.9 shows the values of Γ extracted from the fit of the hybridization curves measured for the no linker probe type, which is the case with larger n and hence larger observable deviations from a Langmuir model. The values of Γ are consistent with a liner scaling with s_p, as $\Gamma = \gamma s_p$ (Equation 3.7). On the basis of this observation and on the analogous dependence predicted in [32], for each experiment we fitted the amplitudes and rates of the hybridization curves as a function of both c_t and s_p, assuming a linear dependence between Γ and s_p.

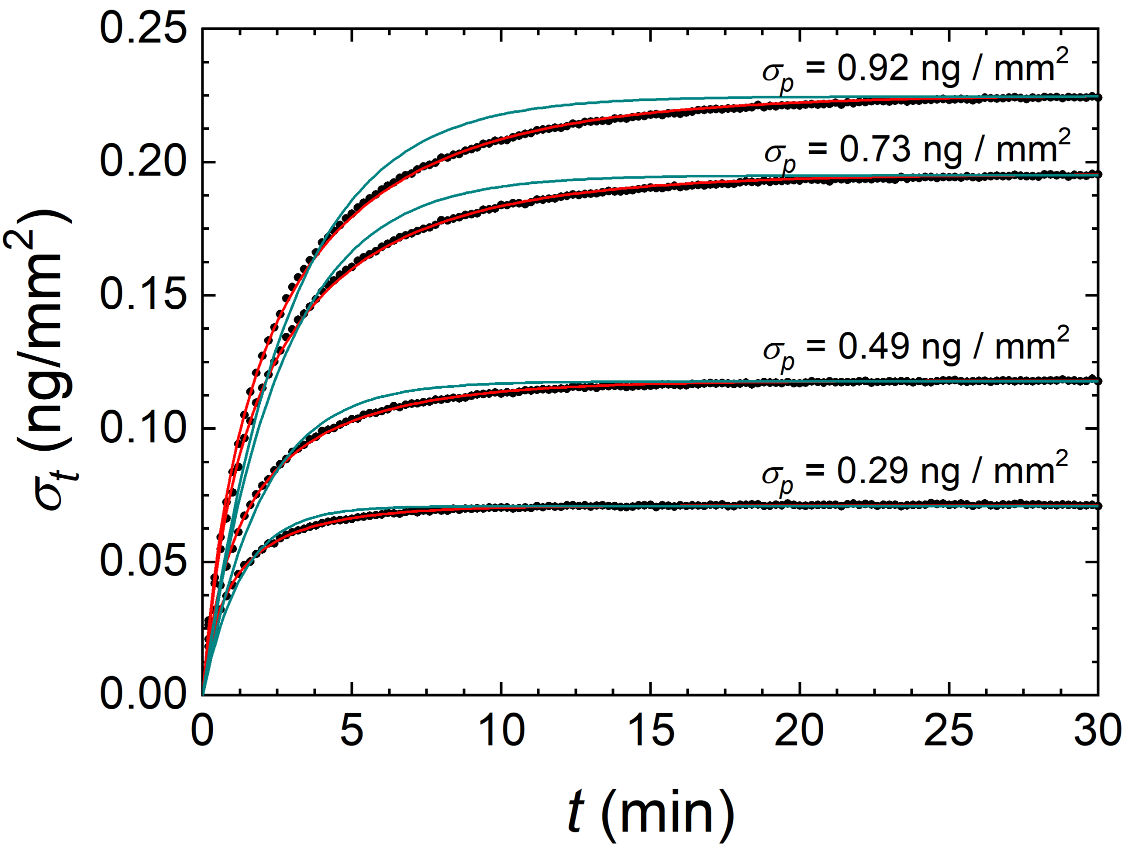

Figure 3.8: Free exponential fit of the hybridization kinetic curves measured by RPI. The black dots and the red curves are mass surface density data and NLER model fits shown in Figure 3.2 of the main text, respectively. The binding curves refer to spots on the same RPI sensor with different surface density σ_p of DNA probes (no linker type) and are measured after the injection of 100 nM of target DNA in solution with 150 mM NaCl. The light blue curves represent the best fits with single exponential growth functions without constraint.

Fit quality of equilibrium curves

The equilibrium data reported in Figure 3.3b of the main text are better fitted by the NLER model then by the Langmuir model. In Table 3.3, we report the R^2 values and the residual sum of squares values (RSS) for both fits shown in Figure 3.3b (blue and green lines for the Langmuir and NLER model, respectively). The R^2 values for NLER model are constantly larger than those for the Langmuir model, whereas the RSS are constantly smaller. This means that the NLER model produces fits that represent the data more accurately, as also clear by visual inspection of Figure 3.3b. Additionally, the fit quality of the Langmuir model decreases with the increase of probe density, indicating that the DNA hybridization equilibrium data deviate more from the Langmuir model at larger probe densities. This observation is coherent with the results reported in this work.

The residual analysis of fits in Figure 3.3b is shown in Figure 3.10. Results indicate that the NLER model is both more precise and more accurate than the Langmuir model, as indicated by the vicinity of the red dots to the zero line and their reduced spread. The larger residuals at the lowest target concentrations ($c_t = 0.5$) is ascribed

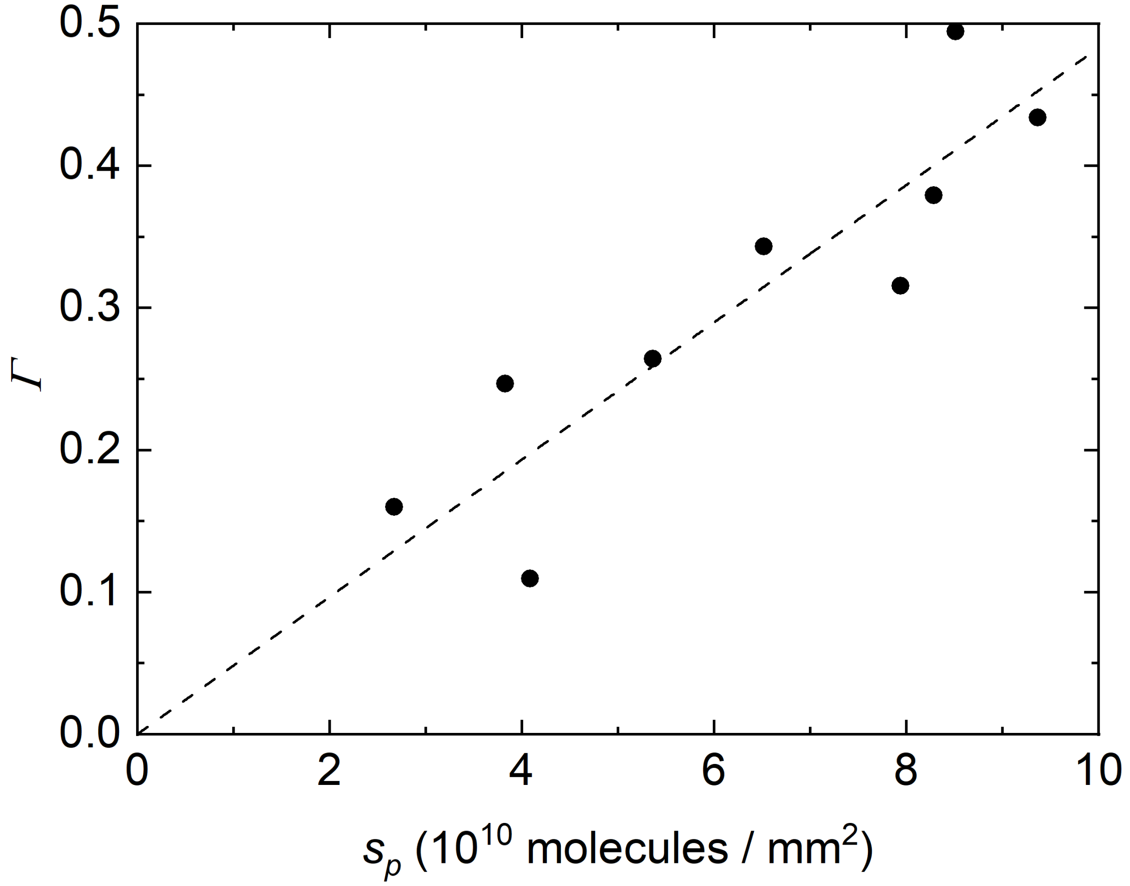

Figure 3.9: Measured dependence of electrostatic repulsion parameter Γ on the surface density of probes. Values of Γ obtained from the fit of the hybridization curves with the solutions of Equation 3.6 for different surface density of probes (no linker type). The line is a linear fit with slope $\gamma = 0.48 \cdot 10^{-10} mm^2$.

to a lower accuracy in determining the equilibrium amplitudes of the binding curves. Overall, the difference in the fit quality between the two models increases with probe density, suggesting that the Langmuir model indeed does not represent well DNA hybridization on a surface at large probe densities.

	Langmuir model		**NLER model**	
σ_p(ng/mm^2)	R^2	RSS	R^2	RSS
0.19	0.9904	$6.6 \cdot 10^{-5}$	0.9964	$2.5 \cdot 10^{-5}$
0.24	0.9887	$2.8 \cdot 10^{-4}$	0.9986	$3.3 \cdot 10^{-5}$
0.38	0.9853	$8.1 \cdot 10^{-4}$	0.9989	$6.2 \cdot 10^{-5}$
0.41	0.9836	$1.0 \cdot 10^{-3}$	0.9993	$4.5 \cdot 10^{-5}$

Table 3.3: R^2 values and residual sum of squares (RSS) for fits to equilibrium curves in Figure 3.3b.

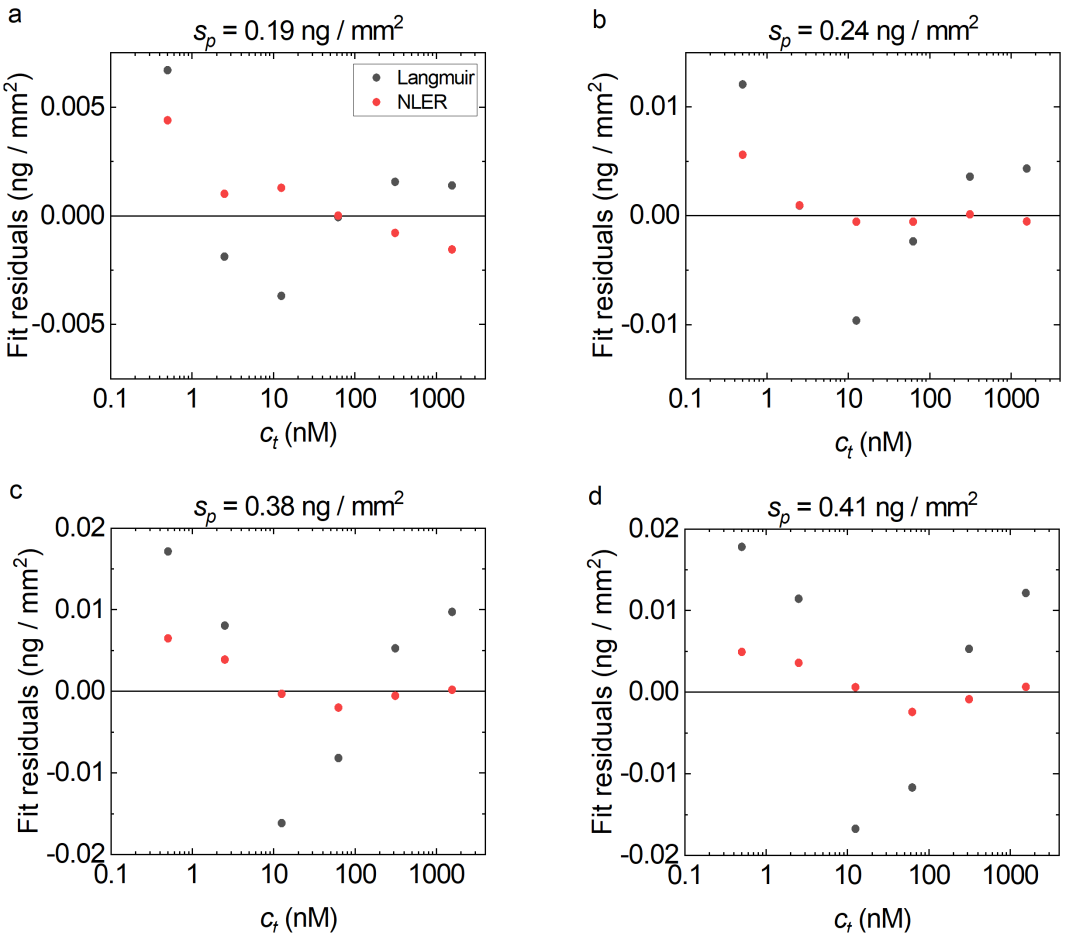

Figure 3.10: Fit residuals for the equilibrium data of Figure 3.3b. The residuals are calculated as the difference between observed value and predicted value, from the fits of both Langmuir and NLER model. NLER model fit residuals are shown as red dots, Langmuir model fit residuals are shown as grey dots. NLER model is systematically more accurate than the Langmuir model across all observed target injections, as seen in the distance from the zero line. Smaller deviation of red dots indicate that the NLER model is also more precise than its Langmuir counterpart.

3.1.2 Optimization of miRNA assay and competitive antibody-antigen hybridization

Introduction

MicroRNA's are small non-coding pieces of RNA, about 20 bases long that function in post-transcriptional regulation of gene expression. They are usually found inside of cells, or in the case of circulating miRNA, outside of the cell. Due to their role in regulation of protein levels, fine tuning of many physiological procesess and high accesibility, specificity and sensitivity, miRNA are considered as a highly promising biomarkers for the future [86][87]. Alles et al estimated that there are about 2000 distinct miRNA sequences in human body [88]. However, despite the great promise as a biomarker, the distribution of specific miRNA targets across body fluids varies greatly. It has been estimated that the concentration of specific miRNA targets in serum or plasma can be as low as 0.1 fM [89]. This still presents a serious challenge for biosensing and inhibits it's widespread use. We developed a three-stage biosensor based assay, capable of sub-picomolar detection of miRNA. The assay is based on the capture of miRNA target with a surface bound DNA probe, resulting in the formation of RNA-DNA hybrid. This first stage is followed by two-step mass amplification, in which the hybrid is first recognized by hybrid specific antibody, and second, target specific antibody is recognized by specific secondary antibody. Three stage assay therefore involves following interactions:

1. NA - NA interaction; i.e. formation of surface hybrid via RNA - DNA hybridization
2. Protein - DNA interaction; i.e. hybrid recognition by hybrid specific Ab1
3. Protein - protein interaction; i.e. Ab1 is recognized by specific Ab2

Three stage assay is visualized in Figure 3.11. It is important to notice that for the Ab1 to bind on the surface, it is crucial that the hybrids are formed, Ab1 is hybrid specific, therefore it will not interact with miRNA in solution nor with ssDNA probes on the surface. However, specific Ab2 recognizes Ab1, and for them to interact it is not of much importance whether one of them in freely diffusin in solution or bound to surface. Furthermore, from the previous considerations, we can see that the total signal amplification will depend on the kinetics of all the involved interactions. Therefore, for the stage I of the assay, the amplification governing factor will be the different sequence of miRNA and it's translation to kinetcs of hybridization. For the stage II and III, the amplification factor will be largely influenced by the availability of Ab1 in solution, which in turn again depend on the kinetics of hybrid formation, since hybrids present the probes for Ab1. Selected miRNA sequences are shown in Table 3.4.

Target	Sequence	Length / nt
miRNA-16	UAGCAGCACGUAAAUAUUGGCG	22
miRNA-21	UAGCUUAUCAGACUGAUGUUGA	22
miRNA-125	UCCCUGAGACCCUUUAACCUGUGA	24
miRNA-210	CUGUGCGUGUGACAGCGGCUGA	22
miRNA-223	UGUCAGUUUGUCAAAUACCCCA	22

Table 3.4: Target miRNAs and their sequences and lengths in bases. Sequences are written in 5' → 3' direction.

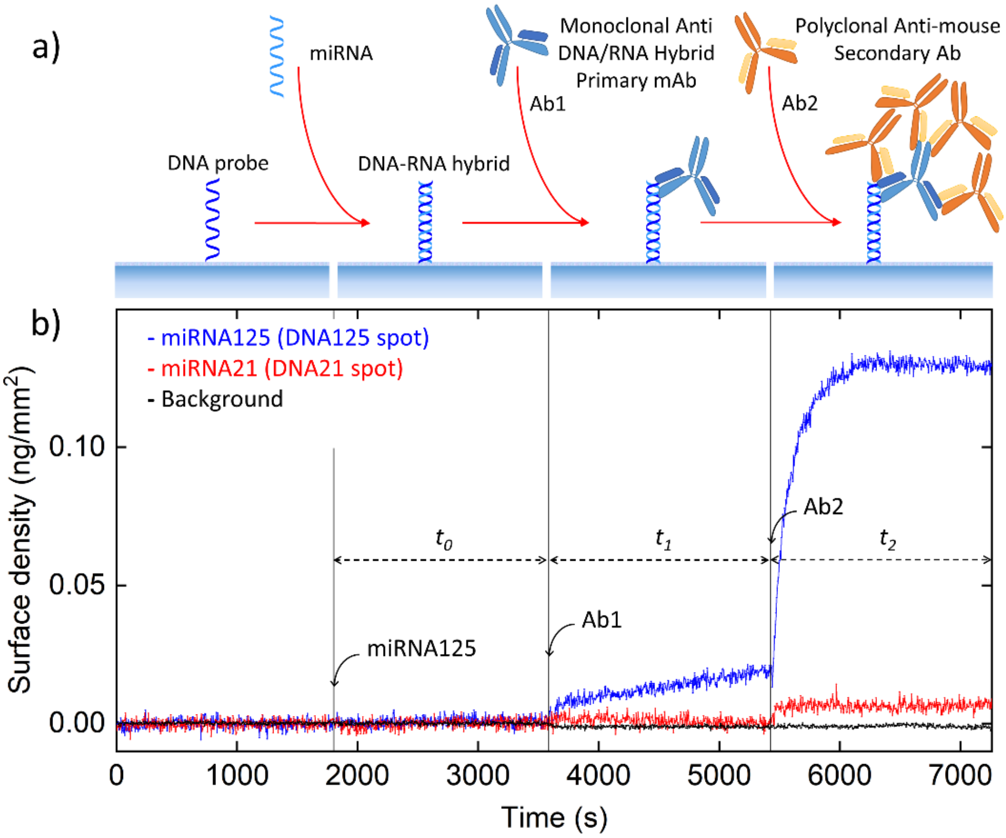

Figure 3.11: (A) Three stage assay: DNA probe carrying a complementary sequence of miRNA target is grafted on the surface. Solution incubated miRNA targets diffuse to the surface and bind the probe. In the second stage, Ab1 is added to the solution, Ab1 diffuses and binds only on the probes carrying the miRNA target. Because the mass of the Ab1 is much greater than the miRNA, this binding results in non-zero output from the biosensor. Further amplification is achieved in third stage by adding a secondary Ab2 that recognizes only the surface bound Ab1 and free Ab1 diffusing in solution (this will be adressed later on). (B) Preliminary curve showing virtually no response fromt the sensor after the injection of miRNA target. Following the addition of Ab1, only spots initially carrying complementary sequences of miRNA (and therefore able to bind the miRNA) respond. Because each Ab1 has seven binding sites that bind Ab2, on roughly equal mass, the addition of secondary Ab2, the signal of the sensor is even more amplified.

In order to optimize the assay parameters we built a simple kinetic model of three bound differential equations, each describing the binding of one stage. Based on the solutions to these equations we were able to find the best time distribution for three incubations, i.e. how long to incubate miRNA, when to inject Ab1 and when to inject Ab2. For the sake of consistency and practicality, we decided to keep the total assay duration fixed at 1.5 hours. The starting equations are shown below:

$$\frac{\partial \phi_0}{\partial t} = k_{on,0} c_0 (1 - \phi_0(t)) - k_{off,0} \phi_0(t) \tag{3.10}$$

$$\frac{\partial \phi_1}{\partial t} = k_{on,1} c_1^* (\phi_0(t) - \phi_1(t)) - k_{off,1} \phi_1(t) \tag{3.11}$$

$$\frac{\partial \phi_2}{\partial t} = k_{on,2} c_2^* (\phi_1(t) - \phi_2(t)) - k_{off,2} \phi_2(t) \tag{3.12}$$

where, indices 0, 1, 2 correspond to each stage, index 0 correspond to binding of miRNA to DNA probes, 1 corresponds Ab1 binding on surface hybrids, and index 2 is associated to the Ab2. Hence, $\phi_{0,1,2}$ correspond to bound fraction of miRNA, Ab1 and Ab2 respectively, $k_{on,0,1,2}$ and $k_{off,0,1,2}$ represent the association and dissociation constant respectively. Concentration is denoted as $c_{0,1,2}$. Specifically, unlike the RNA/DNA hybrid formation and Ab1-hybrid interactions, which occur in stoichiometric ratio of 1, i.e. one DNA binds one RNA, Ab1 has seven binding sites for Ab2 (note that this is the why of the aditional amplification, since their masses are roughly equal), solution to Equation 3.12 was also multiplied by $n_1 = 7$, where n_1 denotes the number of binding sites for Ab2 on Ab1. The model neglects the steric effects of large Abs on the surface, and is therefore limited to small values of ϕ_0, i.e. small concentrations of miRNA targets. As mentioned before, solutions to the equations are infected fractional values, meaning that $\phi_{0,1,2}$ has values from 0 to 1, therefore, to convert the solutions to physically meaningful values, all solutions were multiplied by the asymptotic values of surface density Σ_∞, where asymptotic surface density for miRNA $\Sigma_{\infty,0}$ was observed experimentally, asymptotic surface densities for Ab1 and Ab2, $\Sigma_{\infty,1}$ and $\Sigma_{\infty,2}$ were obtained considering mass and stoichiometric ratios. Considering that mass of Ab1 is much greater than mass of miRNA, i.e. $m_{Ab} = 21 m_{miRNA}$, and that Ab1 will bind to formed hybrids in 1:1 ratio, we can conclude that maximum possible asymptotic value for Ab1 will relate to asymptotic surface density of miRNA as 21:1. In contrast, to obtain the asymptotic surface density of Ab2, we have to consider the stoichiometric ratio of the reaction, since their masses are roughly equal, i.e. $m_{Ab1}/m_{Ab2} = 0.993 = 99.3\%$, but one Ab1 can hold seven Ab2, as mentioned before, we can conclude that maximum possible asymptotic value for Ab2 will relate to asymptotic surface density of Ab1 as 7:1. Therefore, our asymptotic surface density conversion are all given by experimentally observed asymptotic surface density of miRNA, and we can write:

$$\Sigma_{\infty,1} = 21 \Sigma_{\infty,0} \tag{3.13}$$

$$\Sigma_{\infty,2} = 7 \Sigma_{\infty,1} = 147 \Sigma_{\infty,0} \tag{3.14}$$

Former equations allow us to give some estimation of maximum possible amplification factor. Considering the whole amplification is given by mass amplification of Abs pairing on target carrying DNA probes, we define the amplification factor as:

$$Amplification factor = \frac{Total\ output\ signal}{Signal\ due\ to\ the\ bound\ miRNA} \tag{3.15}$$

or in a more strict way:

$$A = \frac{\Sigma_{\infty,0}\phi_0 + \Sigma_{\infty,1}\phi_1 + \Sigma_{\infty,2}\phi_2}{\Sigma_{\infty,0}\phi_0} \tag{3.16}$$

Putting aside the steric constraints and letting the system go into complete saturation, i.e. $\phi_0 = \phi_1 = \phi_2 = 1$, and considering Equations 3.13 and 3.14, we obtain the maximum theoretical amplification factor, $A_{max} = 169$. However it should be noted that this amplification factor is practically unachievable, as it is calculated on complete hybridization yield between DNA probes and miRNA targets, all hybrids decorated with one Ab1, and all binding sites on all surface bound Ab1 occupied with Ab2. Aditionally, Equation 3.16 can be written in terms of masses as:

$$A = 1 + \frac{m_{Ab}}{m_{miRNA}} \frac{\phi_1 + n_1\phi_2}{\phi_0} \tag{3.17}$$

where $m_{Ab} = m_{Ab1} + m_{Ab2}$ is the mass of both Abs. Note that concentrations of Ab1 and Ab2 are marked with small star, this is because of their interaction happening also in solution, and not exclusively on the surface. In order to account for as many interactions as possible, we also considered that some Ab pairs will form in solution, leading to smaller number of available Abs that can bind to the surface hybrids. This also leads to a disturbed equilibrium for Ab1 which is already bound on the surface with some concentration, prior to the injection of Ab2. We call this corrected concentration - effective concentrations. Considering that Abs in solution are free to diffuse, where instead on the surface one is inhibited in space and in principle awaits the binding partner to reach specific (x,y,z) in order to bind, we assumed a bimolecular interaction of Ab1-Ab2 in solution happening instantly, that is, solution equilibrium is reached much faster than the surface equilibrium, i.e. solution system reaches the equilibrium during within the experimental resolution time. Considering that each Ab2 has two binding sites for Ab1, for two antibody paratopes, that is $n2 = 2$, and, as before, each Ab1 can hold seven Ab2 at once, i.e. $n1 = 7$. The equilibrium condition is then given by concentrations of both Abs, i.e. for Ab1-Ab2 interaction we can rewrite the concentrations as:

$$c_1 = n_1 c_{1,0} \tag{3.18}$$

$$c_2 = n_2 c_{2,0} \tag{3.19}$$

where $c_{1,0}$ and $c_{2,0}$ are nominal concentrations injected in the cuvette. Accordingly, the concentration c_2^* of free Ab2 antibody available for the binding with Ab1 on the surface is given by:

$$c_2^* = \frac{(n_2c_2 - n_1c_1) - K_d + \sqrt{(n_1c_1 - n_2c_2 + K_d)^2 + 4K_dn_2c_2}}{2n_2} \tag{3.20}$$

where $K_d = 1.3$ nM is the equilibrium of Ab pairs in solution, and is determine so that the measured initial slope of the Ab2 binding curves $\sigma(t)$ show a linear dependence as a function of c_2^*. Analogously, the concentration c_1^* of available Ab1 in solution is also affected by the binding with Ab2 and is obtained as:

$$c_1^* = c_1 - \frac{n_2}{n_1}(c_2 - c_2^*) \tag{3.21}$$

Based on this model, the assay was optimized in terms of amplification factor in function of time distributions for all three injections, miRNA, Ab1 and Ab2, as well as concentrations of those injections. To collect all the necessary parameters for the simulation, kinetics and equilibrium for five different miRNA targets, Ab1 and Ab2, we first measured the assay response to all three stages in different concentrations. Five distinct DNA probes carrying complementary sequences to miRNA targets were grafted, and the binding was observed when miRNAs were added sequentially at increasing concentrations (0.1 nM was followed with 0.5, 2.5, 12.5, 62.5, 312.5 and finally 1562.5 nM), without any washing steps. The sensor response is shown in Figure 3.12.

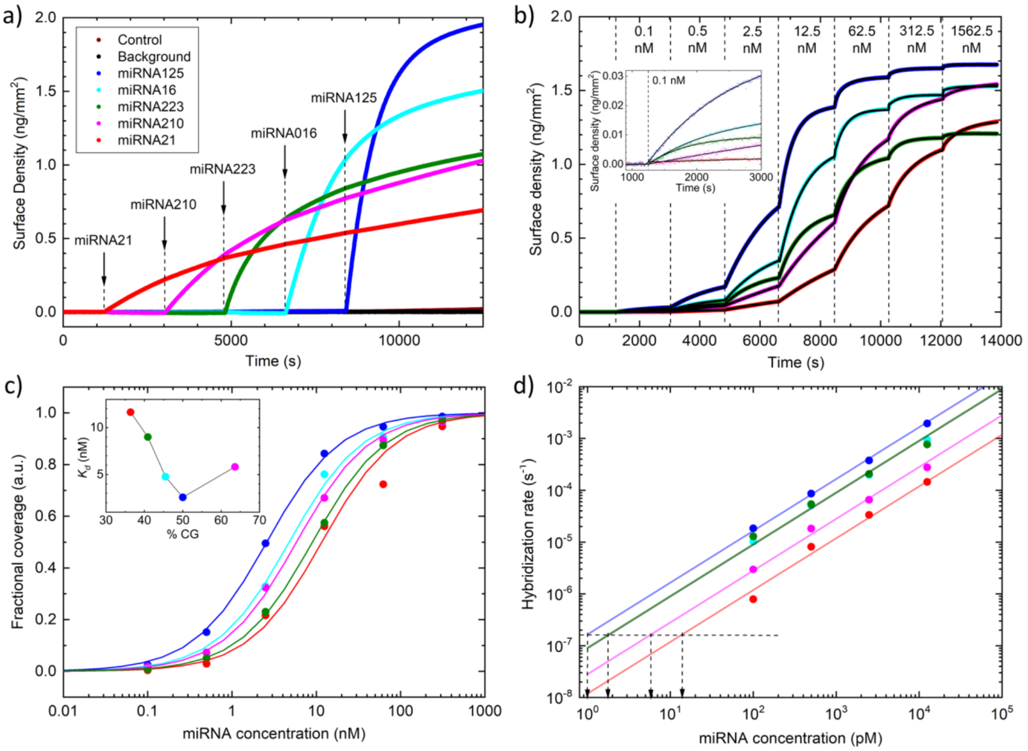

Figure 3.12: (A) Single injection of 12.5 nM of different miRNA targets. There is a clear difference in response based on selected target. Response observed from miRNA-125 can only partially be explained by different sequence length, however, the response varies among other miRNA targets, which differ only in sequence, not in length. (B) Full response from sequential additions, there is some response even as low as 0.1 nM. (C) Equilibrium curves of surface density based on sequential additions, K_d values as a function of %GC content are shown in the inset. (D) Kinetic rates as a function of miRNA concentration, continuous lines are linear fits $\Gamma = k_{on}c_{miRNA} + k_{off}$. Dashed lines represent the minimum concentration detectable based on practically observable rate.

Similar experiment was repeated to obtain kinetic and equilibrium parameters for Ab1 and Ab2. For Ab1 experiment, biosensor chip was prepared by incubating 12.5 nM miRNA for 30 minutes, to allow them bind on their specific spots, containing complementary DNA sequences. These newly formed hybrids presented probes for Ab1. After this preparation, Ab1 were sequentially added in increasing concentrations. Figure 3.13 shows the equilibrium and kinetics curves for Ab1 binding. Similarly, Ab2 kinetics parameters were estimated by sequentially adding Ab2 to cuvette in increasing concentrations. Before this incubation, chip was prepared by incubating 12.5 nM of miRNA for 30 minutes, followed by 45 min long incubation of 2.5 nM Ab1 to form the probes for Ab2. Ab2 was injected into cuvette without washing steps, thus allowing the injected Ab2 to interact with leftover Ab1 in solution, from previous injection. This results are shown in Figure 3.14. Kinetic and equilibrium parameters for all miRNAs and Abs are summarized in Table 3.5.

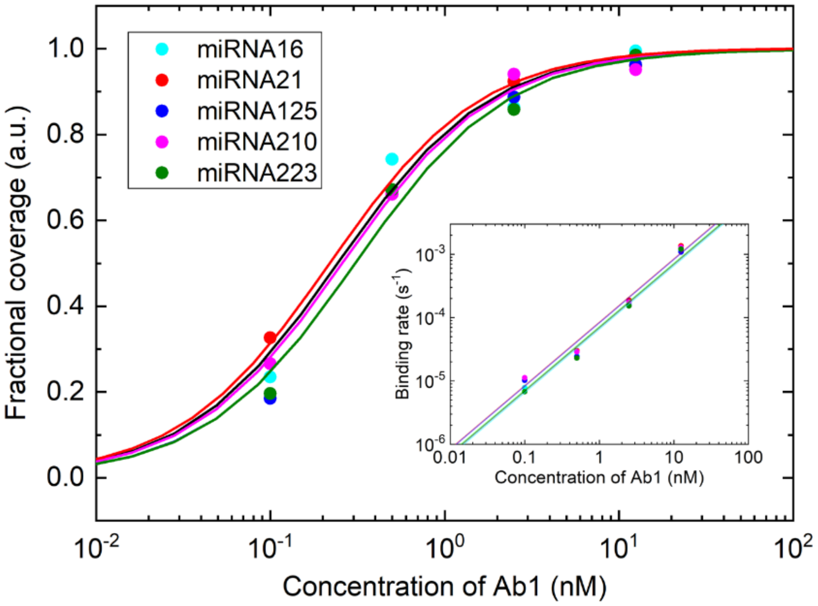

Figure 3.13: Binding curves for Ab1, preceeded by incubation of 12.5 nM miRNA targets for 30 min to form hybrids (probes for Ab1). Ab1 equilibrium and kinetics (inset) are reproducible irrespective of the targeted sequence.

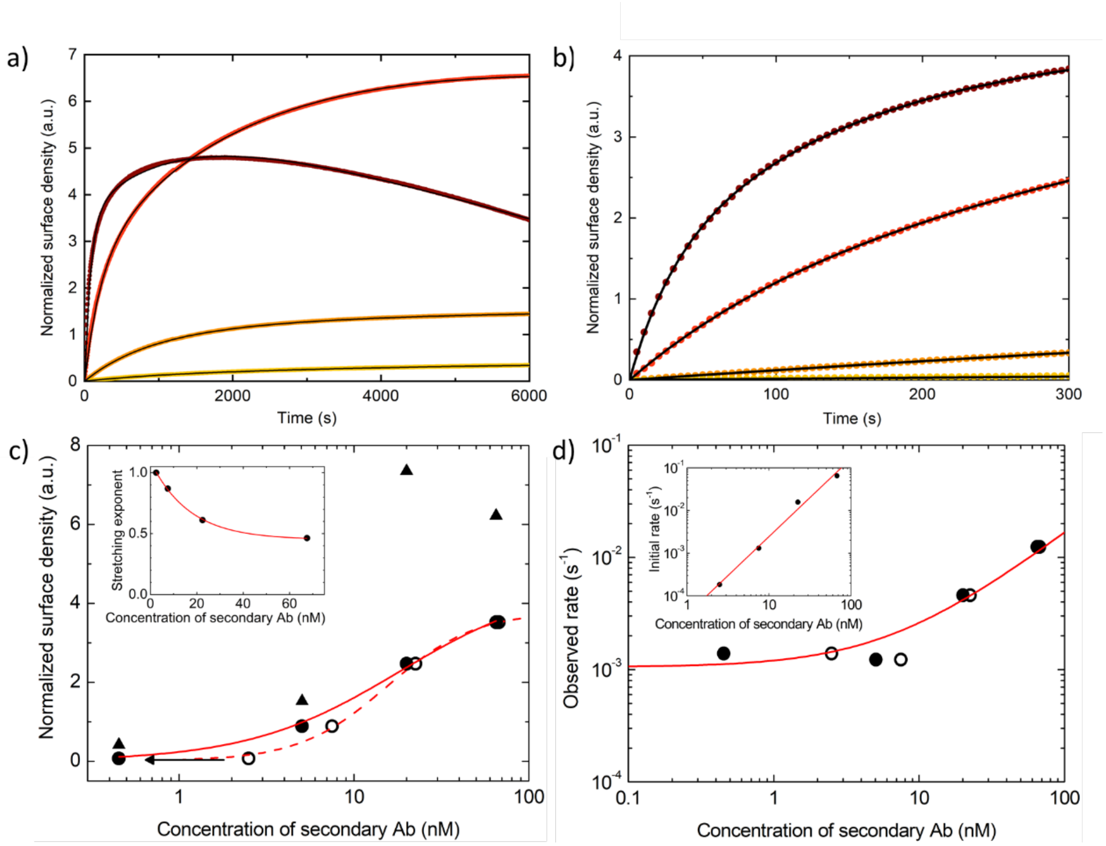

Figure 3.14: (A) Assay response to various concentrations of Ab2. DNA probes were first incubated with 12.5 nM miRNA for 30 min, followed by 45 min long incubation with 2.5 nM of Ab1 to prepare the surface to bind the Ab2. Observed concentrations of Ab2 are 2.5 nM (yellow) 7.5 nM (orange), 22.5 nM (red), 67.5 (brown). Black curves are fits: single exponential for yellow, double exponential (orange), double exponetial with a linear decrease (red and brown). (B) Zoomed in visualization panel (A) in the initial parts of binding. Bindings can be characterized by single exponential if not observed long enough. (C) Equilibrium curves from fits with double exponential growths (triangles), when rapid relaxation contribution (open circles). Dashed line represent the Hill-Langmuir isotherm. When concentration of Ab2 is corrected for Ab1 present in solution, according to Equation 3.20, the reaction can be analyzed by Langmuir isotherm (full circles, full line for isotherm fit). Relaxation exponent from stretch exponential fits to data in panel (A) is shown in inset. (D) Observed binding rate of the rapid relaxation contribution obtained from the fit of panel a curves as a function of the total concentration of Ab2 in solution (open circles) and of the concentration corrected by the competitive effect with Ab1 in solution (full circles). The red curve is a linear fit of full circles data points. Inset: initial slope of the curves of panel a (dots) and power law fit with exponent 1.72.

Target	K_d/nM	$k_{on}/10^{-4}s^{-1}$	k_{off}/s^{-1}	$\Sigma_\infty/ngmm^{-2}$
miRNA-16	11.6	1.2	1.4	1.2
miRNA-21	9.0	9.2	8.3	1.2
miRNA-125	4.8	8.9	4.2	1.5
miRNA-210	2.6	16.5	4.3	1.7
miRNA-223	5.8	2.8	1.6	1.4
Ab1	0.27	7.4	0.2	12.9
Ab2	18.0	15.6	10.5	85.5

Table 3.5: Kinetic paramaters for all miRNA targets and both primary and secondary Ab. Last column shows the saturation surface densities.

Using parameters from Table3.5 we built a simulated amplification factor map, considering miRNA-21 kinetic parameters. Equations 3.10 - 3.12 were solved for maximum amplification factor changing injected concentration of Ab1 and permuting different incubation time distributions for all three injections. Figure 3.11 shows the results of this simulation. From the model solutions, for miRNA-21, amplification factor can be increased above 30, while remaining under 1.5h time limit, by spliting the incubation times in $t_0/t_1/t_2 = 1/74/15$ min, for miRNA, Ab1 and Ab2 respectively. Furthermore, solving for concentration of Ab1 in that time distribution, maximum amplification factor is indeed achieved at $c_1 = 4.5$ nM, instead of 2.5 nM, initially considered. Looking at Figure 3.15 we can see that the assay in principle doesn't favour long incubation times for Ab2, and in principle, the incubation time of Ab1 is the dominating factor when comparing the total assay signal with signal that would be produced solely considering miRNA binding. In fact, Figure 3.14, panel (A), suggests why this might be the case. At larger concentrations of Ab2, we observed a decrease in global assay signal, suggesting that in fact the amplification factor, which scales with global assay signal, might be decreasing also. In order to verify this, we simulated the binding in such a regime, setting the injected concentration of Ab2, $c_{Ab2,0}$ to 67.5 nM.

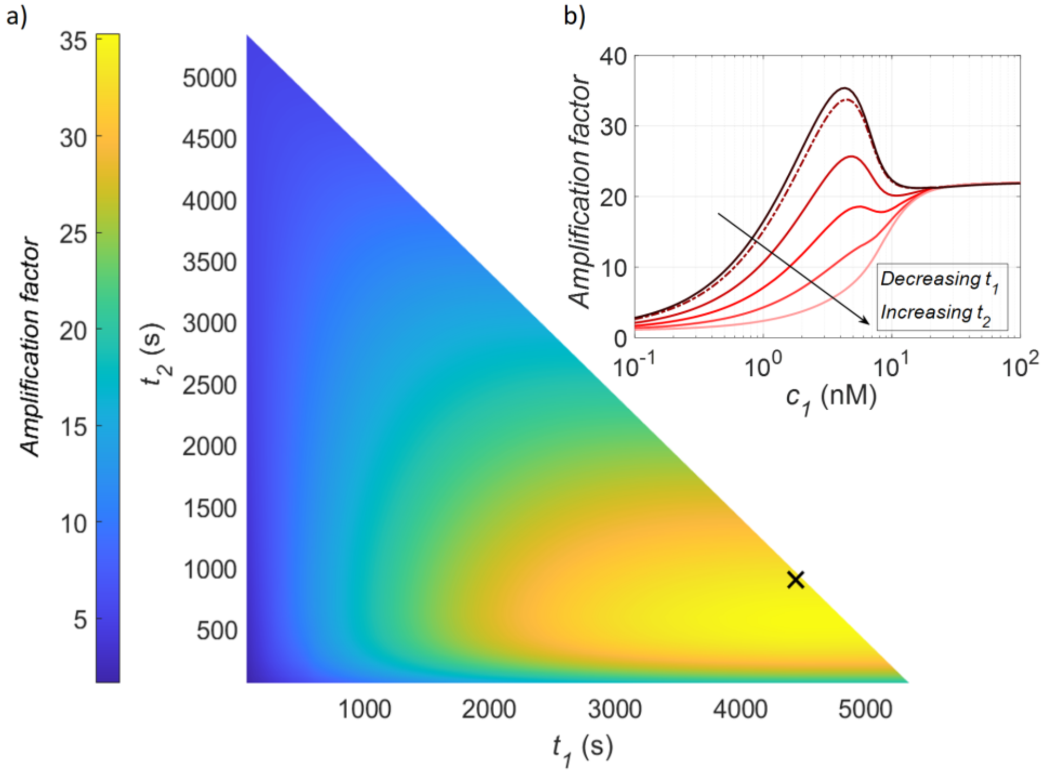

Figure 3.15: (A) Simulated amplification factor map as a function of incubation times of Ab1 (t_1) and Ab2 (t_1). Total time was kept constant at 1.5h, so miRNA incubation time t_0 is calculated in seconds as $t_0 = 5400 - t_1 - t_2$. In general, t_0 is shorter the closer the eyes are to the diagonal. Concentrations considered in this map are $c_0/c_1/c_2 = 0.005/4.5/25$ nM. (B) Amplification factor as a function of Ab1 concetration c_1 for various time distributions. Position of the peak reveals the concentration of Ab1 for which there is maximum amplification.

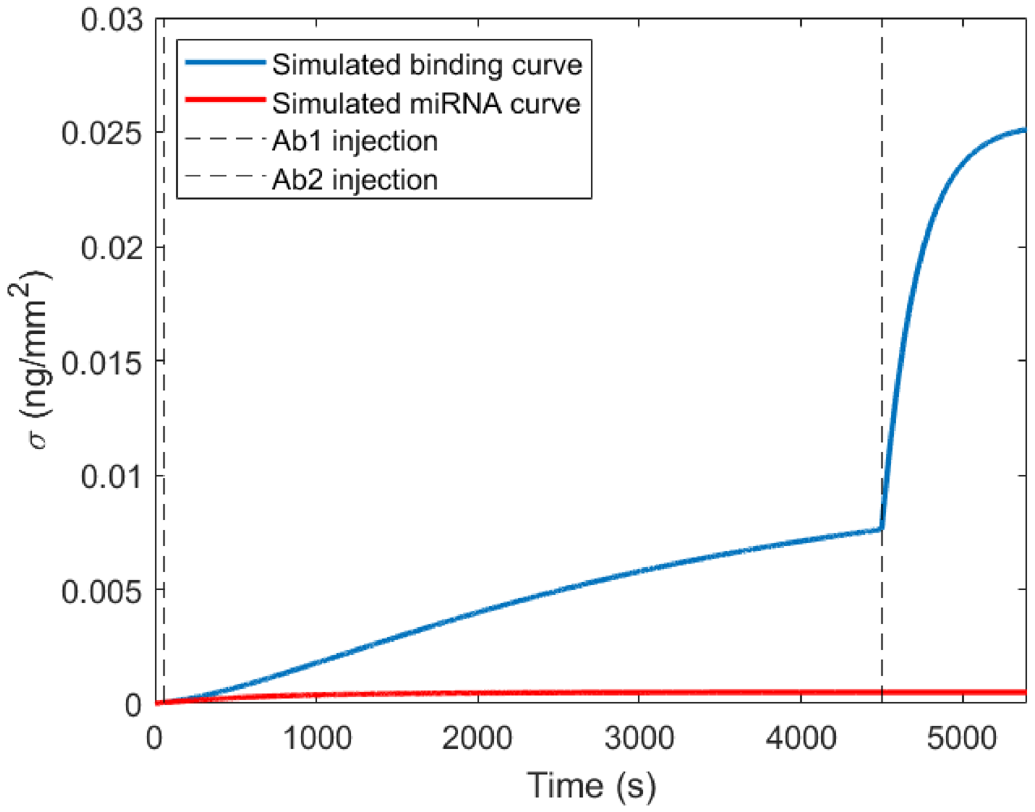

Figure 3.16: Simulated binding curve for settings corresponding to the 'X' position in Figure 3.11. Dashed vertical lines represent the moment of injection of Ab1 and Ab2. Blue line is the simulated complete binding curve. Red line represent the miRNA binding, i.e. the solution to 3.10. Before the addition of the primary Ab, blue and red signal are identical. Amplification factor is obtained by dividing the final value of the blue channel with the final value of the red channel.

3.1.3 DNA as a probe for protein-DNA interactions

Introduction

Protein-DNA interactions present are one of the most vital interactions in cells, whether we are thinking about DNA replication, gene transcription, recombination, DNA repair, etc. All these interactions are in essence DNA-protein interactions. Typically, for the proteins to perform their function, they are required to bind to some specific part of DNA. This requires for a protein to recognize a small part of DNA, from many other possible parts where it can bind. Usually this recognition is achieved by a variety of actions the protein undergoes, from sliding along the DNA molecule, binding and unbinding, diffusion[90][91][92]. Therefore, for the protein to be bound on specific DNA binding site, that binding has to have affinity much larger than binding on any other part of the DNA. Likewise, kinetic rates responsible for the rates of hopping on other DNA molecules, sliding along the DNA molecules, or simple binding and unbinding, of such binding sites must be largely different from any non-specific binding site to allow itself to be distinguished. We studied the binding of Gal4 to DNA. Gal4 is a paradigmatic gene regulator of Saccharomyces cerevisiae [93][94] Figure 3.17 shows the visualization of Gal4 and consensus binding site on DNA, as well as various DNA probes constructed to study the DNA-protein interaction. We constructed DNA hairpin structures both with and without consensus sequence, and regular dsDNA probes were grafted, also with and without consensus sequence, panel (B). Finally, Figure 3.17. (C) shows the free energy profile of the system.

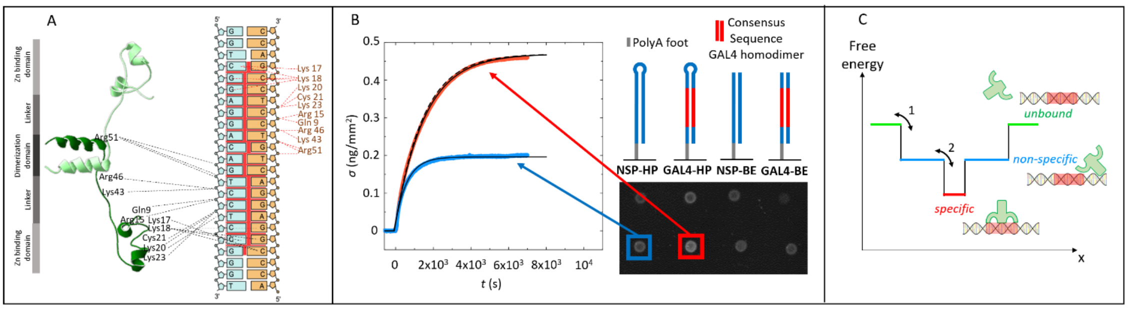

Figure 3.17: (A) Gal4-DNA binding. Gal4 visualization code from PDB: 3COQ. DNA is shown with Gal4 specific binding sequence. Hydrogen bonds between Gal4 amino acids and consensus DNA sequence are shown as dashed lines. (B) Specific (red) and non-specific (blue) binding curve of Gal4 binding on dsDNA probes on RPI. Specific binding is longer and accepts larger amount of bound proteins compared to probes not containing specific sequence. Top right: different DNA probe structures, consensus sequence is shown as red line in blue strand. First two structures are hairpin structures, with and without consensus sequence. Second two strutures are dsDNA sequences, with and without consensus sequence. (C) Free energy landscape for Gal4-DNA binding, generic reaction coordinate is shown on x-axis. Distance along x corresponds to number of conformations accessible to the system.

Results

We performed a systematic investigation of equilibrium and kinetics of Gal4-DNA binding, using different DNA probe structures, specific and non-specific binding sites and under different salt concentrations. The analysis was carried out under a hierarchical two-step process model, which enables extracting the difference in free energy between the two modes of interaction. Gal4 was injected in sequential additions, with increasing concentrations, from 0.08 to 50 nM, and response was observed. Figure 3.18 (A) shows the binding curves for spots containing 10 µM of probes. Observed binding is systematically slower and stronger on spots containing sequence specific probes, compared to spots not containing sequence specific probes. All injections were fitted with:

$$\sigma(t) = \Sigma(c)(1 - e^{-\Gamma(c)t}) \tag{3.22}$$

where $\sigma(t)$ represents the adsorbed mass in time, c is the concentration of Gal4 injected, $\Gamma(c) = k_{on}c + k_{off}$ is the growth rate, and $\Sigma(c)$ can be fitted with a Langmuir curve in the following form:

$$\Sigma(c) = \frac{\Sigma_\infty}{1 + \frac{Kd}{c}} \tag{3.23}$$

where $K_d = k_{off}/k_{on}$ is the equilibrium constant, and Σ_∞ is the saturation mass density at large concentrations. Later was assumed constant for both specific and non-specific probes, since both can theoretically hold the same number of proteins, i.e. specificity controls the kinetics and affinity towards binding, not the overall holding capacity. From Equation 3.23 we were able to obtain the equilibrium values for specific and non-specific spots. As expected, probes containing specific sequences bind Gal4 with much higher affinity, Figure3.18 (D). The association rate constant k_{on} was obtained fitting the initial binding response after each injection with:

$$\sigma'(c) = \Sigma(c)\Gamma(c) = \Sigma_\infty k_{on}c \tag{3.24}$$

This fits are shown in Figure 3.18 (C). Estimated k_{on} wasn't very different between specific and non-specific interactions. Therefore, we ascribed deviations in equilibrium to different dissociation rate constant k_{off}. In fact, fitting initial slopes for both specific and non-specific spots with same k_{on} and recalling $K_d = k_{off}/k_{on}$, we obtained $k_{off,sp} = 2 - 3 \cdot 10^{-3}s^{-1}$ for specific spots, and $k_{off,asp} = 2.6 - 3.2 \cdot 10^{-4}s^{-1}$ for aspecific spots, a detachment time order of magnitude longer. Small dependence of equilibrium constant on probe density was also observed among specific and non specific interactions. This results are shown in Figure 3.19.

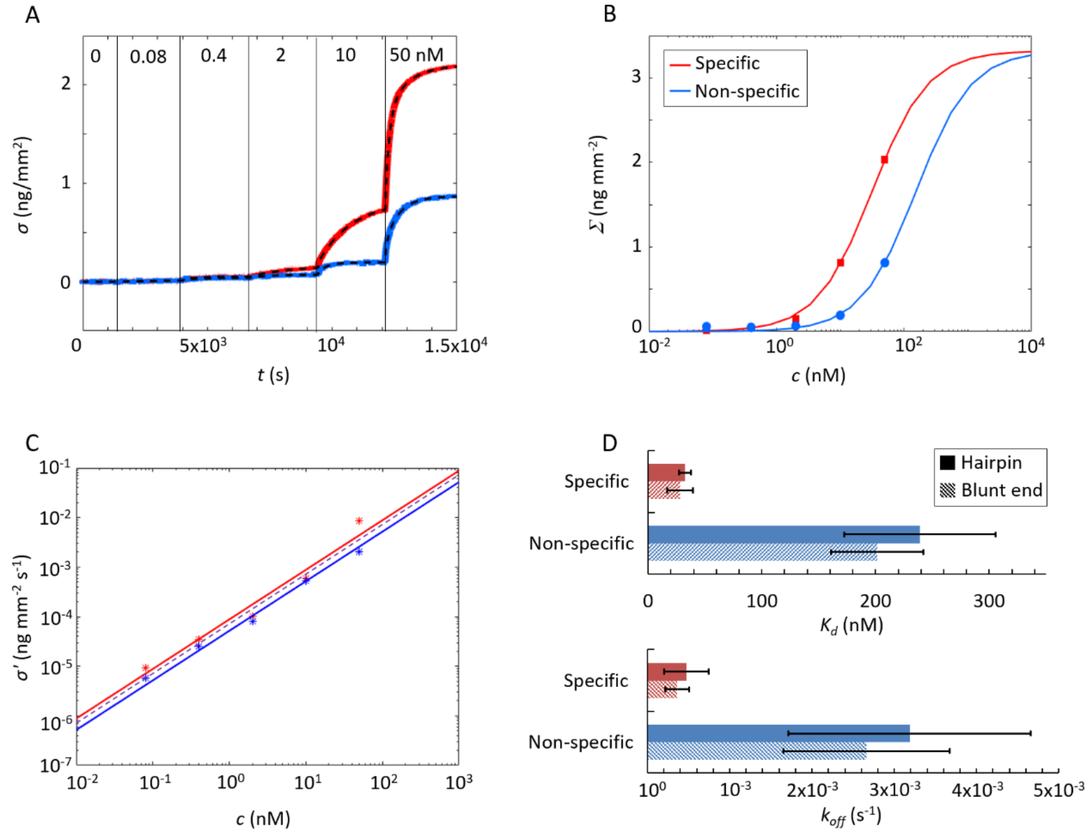

Figure 3.18: (A) Response of specific and non-specific spots to injections of Gal4 at sequentially increasing concentrations. Specific spots systematically show stronger and slower response, compared to spots containing generic DNA sequences. Ionic strength $I_s = 150$ mM, temperature $T = 30$ °C, and $c_{spot} = 10$ µM). Dashed lines are fits from the Equation 3.22. (B) Equilibrium curves for specific and non-specific interactions. Saturation mass density Σ_∞ is assumed constant for both specific and non-specific probes. This allowed the estimation of equilibrium constant K_d. (C) Linear fits of initial slopes, as described by Equation 3.24, allow the estimation k_{off} for both specific and non-specific binding. Continuous lines are linear fits assuming independent association rate constants k_{on} for specific and non-specific binding, dashed line shows the same fit but keeping the value of k_{on} the same for both type of interactions. (D) Values of equilibrium dissociation constant K_d (top) and k_{off} (bottom) of Gal4 on dsDNA (with hairpin or blunt ends) for specific and non-specific sequences. The error bars represent the standard deviation of the average of three values from separate experiments.

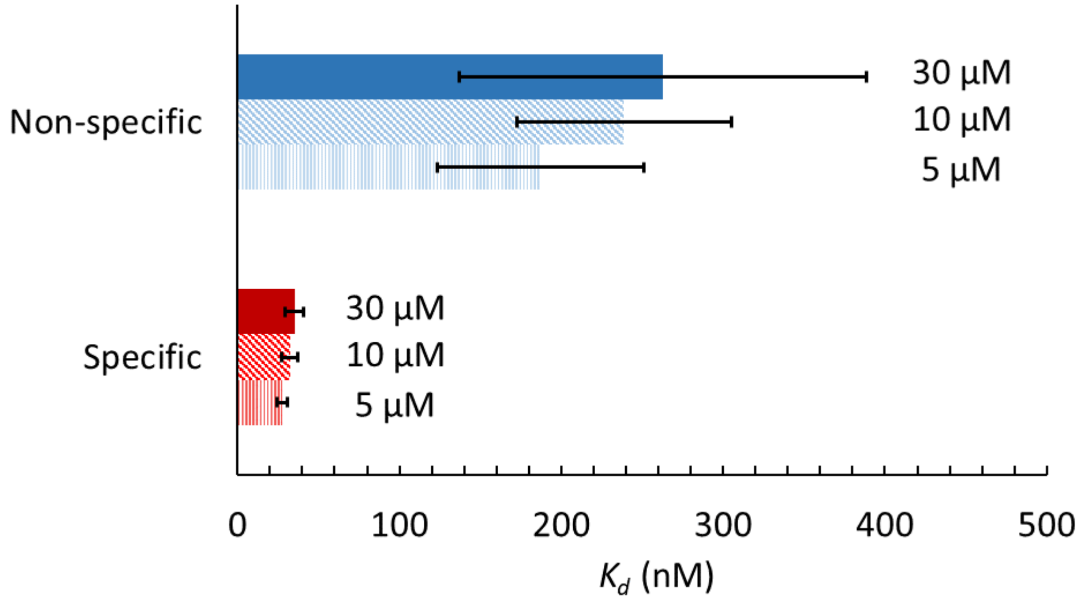

Figure 3.19: Effect of probe surface density on the equilibrium constant for dissociation. Bar graph showing the dissociation constant K_d of GAL4 on specific and non-specific DNA duplexes immobilized with different spotting concentration. The error bars represent the standard deviation of the average of three values from separate experiments.

We then considered the electrostatic contributions with a systematic investigation of binding in various salt concentrations around physiological value of 150 mM monovalent salt (NaCl). Equilibrium and kinetic parameters K_d, k_{off}, k_{on} are shown in Figure 3.20.

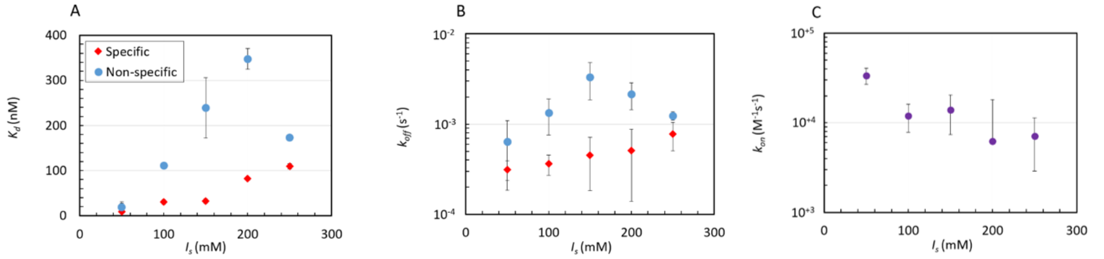

Figure 3.20: Effect of ionic strength on Gal4-DNA interaction. Equilibrium dissociation constant K_d(A) and dissociation rate k_{off} (B) for specific (red) and non-specific (blue) hairpin sequences. (C) Association rate k_{on}, common to specific and non-specific strands.

For specific binding, the affinity tends to increase with salt concentration, as visible in panel (A), red dots, whereas the dependence of non-specific binding on salt concentration is more dramatic, but reaches the maximum at 200 mM salt concentration, panel (A), blue dots. This non-monotonic behaviour leads to a maximum difference between specific and non-specific equilibrium constants, remarkably located around physiological ionic strength of 150 mM. Association rate constant k_{on}

monotonically decreases with salt concentration I_s, as expected since the salt ions reduce the electrostatic "visibility" (Figure 3.20, panel (C)). The escape rate of Gal4 from a generic dsDNA is made easier by increasing salt concentration up to physiological conditions (150 mM NaCl), above which k_{off} sharply drops (Figure 3.20, panel (B)). With spots containing specific sequences, k_{off} is instead monotonic and much milder. We understand this behavior in the following way: the weakening of the electrostatic attraction is more relevant for non-specific interactions, which are less stabilized by hydrogen bonds. However, at large I_s, the value of non-specific k_{off} approaches that of specific interactions, indicating similar stability in the two situations and thus suggesting that the narrowed electrostatic self-repulsion favours the onset of new attractive interactions, possibly additional hydrogen bonds made accessible by previously inaccessible conformations.

3.2 Towards complex structures

3.2.1 Kinetics of hybridization chain reactions

Introduction

DNA Hybridization Chain Reaction (HCR) is a technique based on the ability of two complementary sets of DNA hairpins (so there is also a degree of complementarity there), to recognize and interact with each other causing mutually-triggered cascade reaction that shows great promise as a biosensing amplification technique and a technique for producing triggered self-assembled DNA nanostructures [11][95]. HCR relies on mutually non-interacting, kinetically trapped hairpins. Figure 3.21 shows the toehold exchange, the general principle of HCR. Two kinetically trapped hairpins, H1 and H2, designed with domains labeled with small letters. Domains that are mutually complementing are additionally marked with ”*”. Key features of both hairpins, are the single strand overhangs, a and c*, for H1 and H2 respectively, where c* overhang of H2 carries complementary sequence of the loop part of H1. Without the presence of the trigger sequence, both hairpins are in metastable state. Trigger is shown in panel b, as sequence I. Trigger domain a* is designed to bind on the toehold of H1 and facilitate the opening of the hairpin. Indeed, upon the binding of the trigger sequence to the H1, loop domain c of the H1 gets exposed and is free to bind to the overhang of the H2 and facilitate the opening, i.e. H1 acts as a trigger to H2. This results in the formation of the IxH1xH2 complex. Furthermore, H2, in it’s open state, exposes it’s loop sequence, which is able to open the H1 from the overhang (like the trigger), triggering the new cascade of events. This is the working principle of the hybridization chain reaction.

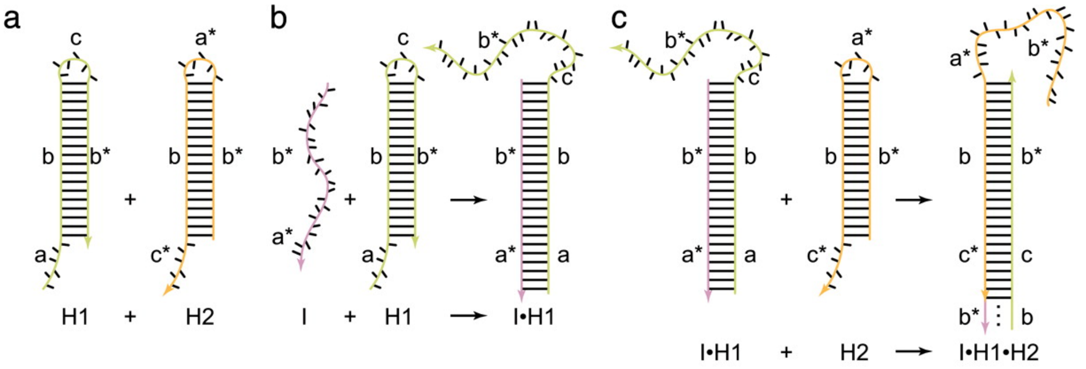

Figure 3.21: Hybridization Chain Reaction mechanism. Two kinetically trapped hairpins, H1 and H2 coexist in solution. Hairpins are designed to share the same stem domains b and b*, while having two overhangs, a and c*, where overhang of the second hairpin H2 can interact with the loop of H1, labelled c, panel (a). Trigger sequence I opens hairpin H1 on its overhang and continues to unzip the hairpin due to the complementarity with the stem sequence of H1, panel (b). Opened hairpin H1, now hybridized with trigger sequence I, binds to the overhang of H2 and continues to unzip the hairpin. H2 can now bind with its loop domain to the overhang of unzipped H1 and the process continues. This ends the 1st iteration of cascade hybridization chain reaction.

It's worth nothing that both hairpins can be designed in such a way to detect any desired sequence, in which case the trigger becomes the targeted sensing molecule. This is the general idea behind biosensing with HCR. We studied the growth of surface bound HCR filaments in real time, with trigger sequence immobilized on the surface, and H1 and H2 injected in different times. Cascade is visualized in Figure 3.22. Trigger sequence "T" is immobilized on surface (red). Following the injection of H1 (purple), we observe a finite adsorbtion of DNA molecules. Injection of H2 in this scenario triggers the cascade, since the presence of H2 allows the adsorbtion of new set of H1. All cascade is controlled by the presence of the trigger sequence on the surface. Indeed, similar strategy was realized here [12], by Spiga et al, with the only difference of another injection prior to H1, which served as detection molecule.

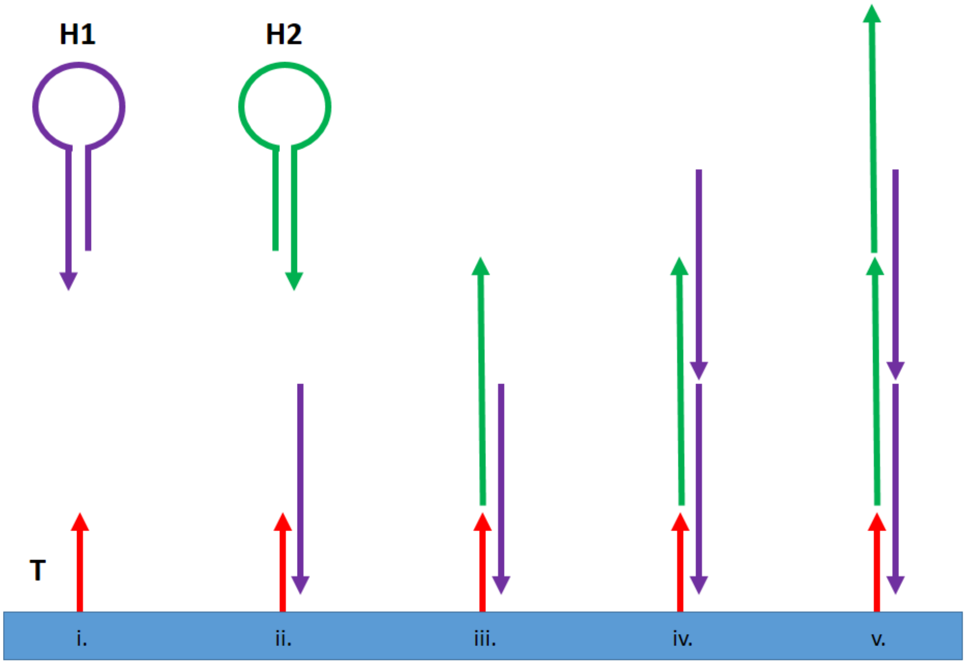

Figure 3.22: Cascade reaction of HCR with immobilized trigger. Trigger sequence (red) is grafted on the surface (shown in blue), H1 (purple) and H2 (green) are dissolved in solution. Cascade steps are shown as Roman numbers on the surface. H1 is able to bind only in the presence of trigger sequence, this binding results in formation of the new probe for H2, via opening of H1. Opening of H2 then creates a new probe for H1 in turn.

Results

RPI allows for the real-time investigation of HCR binding kinetics. The trigger sequence was grafted at different concentrations. Hairpins 1 and 2 were added sequentially at increasing concentrations. Example of HCR cascade experiment is shown in Figure 3.23. Trigger sequences were grafted at three different concentrations, 3 µM (blue), 5 µM (pink) and 10 µM (red). As expected, H1 injection at 125 nM yielded fast, exponential-like response on all probe densities. Furthermore, crowded spots yield higher signal and slower kinetics, which was observed in simple oligo hybridization study, this is an expected results considering the adsorbtion is a finite process in a sense that binding of H1 presents the final step of the process, without the presence of H2. To facilitate the cascade reaction, we injected H2 at the same concentration as H1. We observed a fast response from all spots containing H1 from previous injection. Furthermore, as before, amplitude of spot response correlates with spot probe density, which is in this case the final amplitude of the previous injections (since bound H1 are probes for H2). Unlike the first injection of just one hairpin, the binding curve resulted, generated by the presence of both hairpins, has somewhat complex behaviour and implies multiple processes occuring on the surface. This will be discussed in greater detail later in this chapter. Since the system was close to plateau, after 45 minutes we tried stimulating the cascade further with collective injection of H1 + H2 at 375 nm each, followed by another collective injection 1h after that at 1.125 µM H1+H2 each. Both these injections didn't yield a significant response indicating intrinsic limitations for the growth of such cascade. No response lines, close to zero in the Figure 3.22 correspond to negative controls and background feedbacks. No-response sugegests strong specificity from hairpins towards trigger sequence.

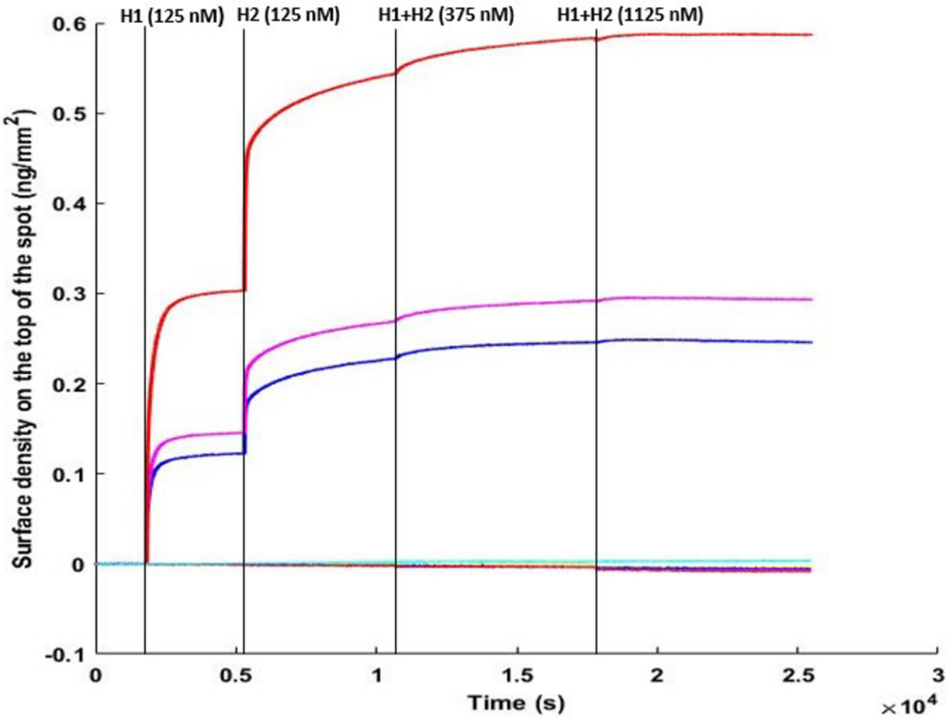

Figure 3.23: HCR growth curves on spots with three different probe densities, 3 µM probe concentration (blue), 5 µM (pink) and 10 µM (red). Control spots and background yield no response, indicating a high selectivity of the reaction. HCR produced filaments might be limited internally, considering the reaction response at higher concetrations.

We analyzed HCR reaction on surface in more detail by sequentially injecting increasing concentrations of H1, from 1 nM to 125 nM. Figure 3.24 shows the binding response to H1. Unlike simple oligo hybridization, we observed a more complex behaviour which cannot be treated by simple exponential growth functions, thus we decided to analyze binding curves with two exponential functions (blue lines):

$$\sigma(t) = A_1[1 - exp(-k_1 t)] + A_2[1 - exp(-k_2 t)] + C \tag{3.25}$$

H1 binding was analyzed using a simple Langmuir model, in order to obtain kinetic parameters and equilibrium characterization of the H1 adsorbtion. Each exponential was treated as a separate Langmuir adsorbtion process. Amplitudes and rates of H1 binding are shown in Figure 3.25. Red lines for amplitude plots represents the Langmuir fits in the form:

$$\sigma_{eq}(c_t) = \frac{Ac_t}{K_D + c_t} \tag{3.26}$$

where A corresponds to the amplitude, and K_D is the equilibrium constant.

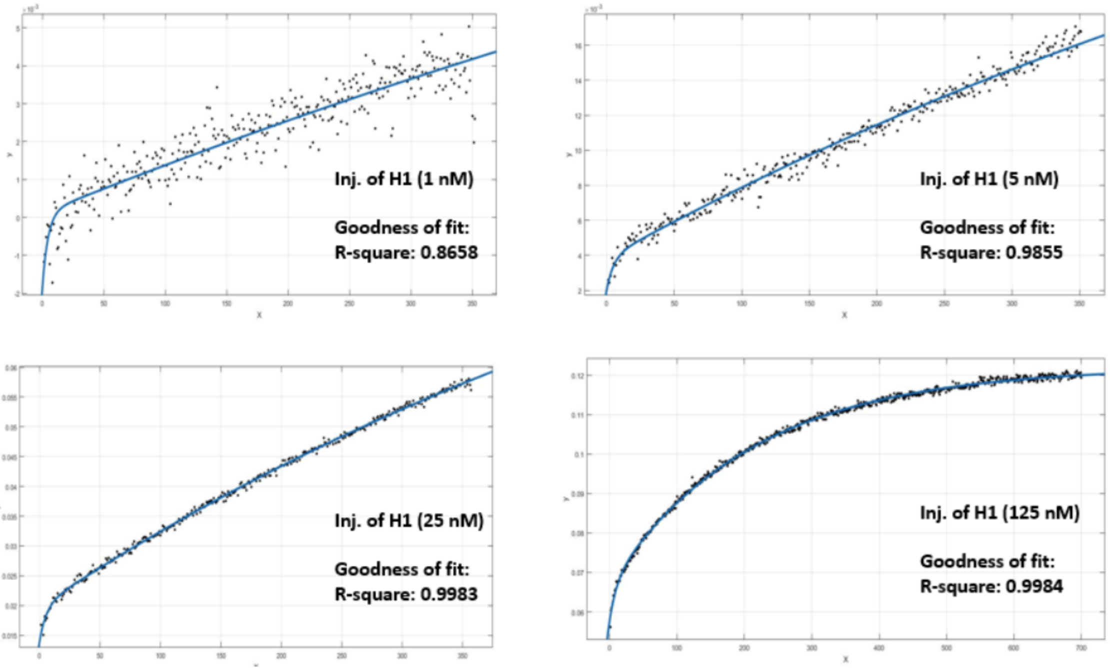

Figure 3.24: Separate plots of H1 injections at increasing concentrations. Blue lines represent the two exponential fits.

Kinetic rates parameters were obtained fitting the exponential rates with linear function in the form:

$$\Gamma(c_t) = k_{on}c_t + k_{off} \tag{3.27}$$

where k_{on} and k_{off} are the association and dissociation rate constant. Same investigation was performed on the combined injection of H1+H2. These results are reported in Figures 3.26. Binding response is qualitatively similar to the response of H1. Two exponential fits are shown with blue lines. Binding curves are qualitatively similar to binding curves for H1. No clear saturation was observed for the reaction in the presence of both hairpins after 40 minutes.

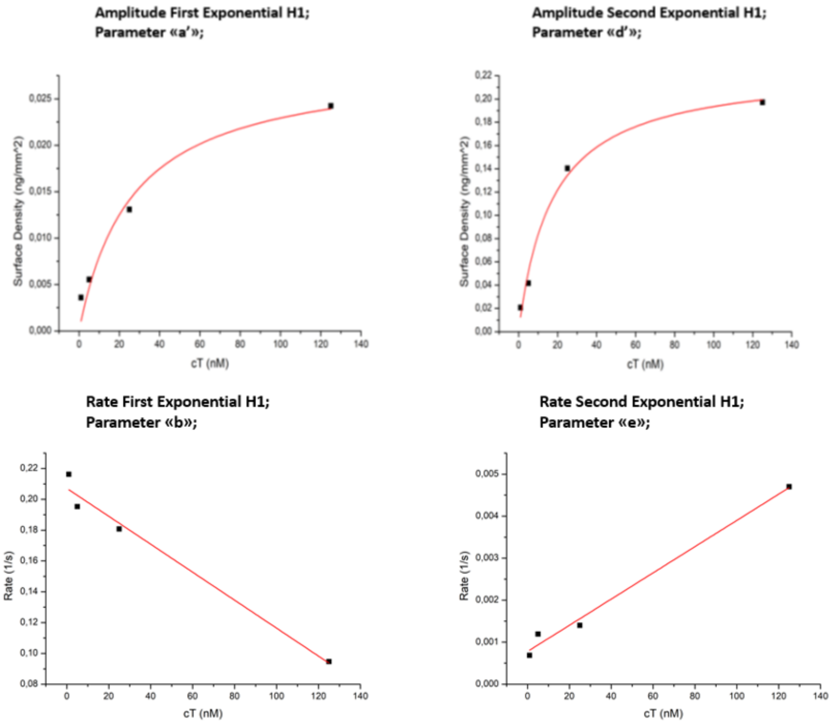

Figure 3.25: H1 equilibrium and kinetics: Top row, equilibrium fits for Exp1 (left) and Exp2 (right). Red lines are Langmuir fits, Equation 3.25. Bottom row, kinetic fits from Equation 3.27 are shown as red lines.

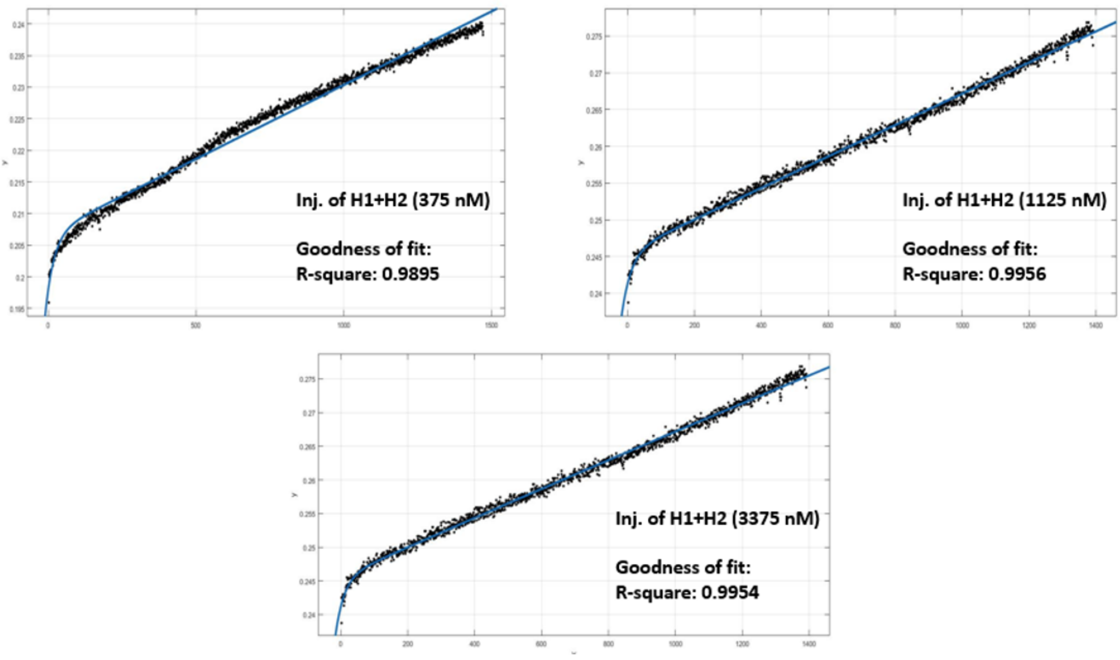

Figure 3.26: HCR growth following an injection of both H1 and H2 at increasing concentrations.

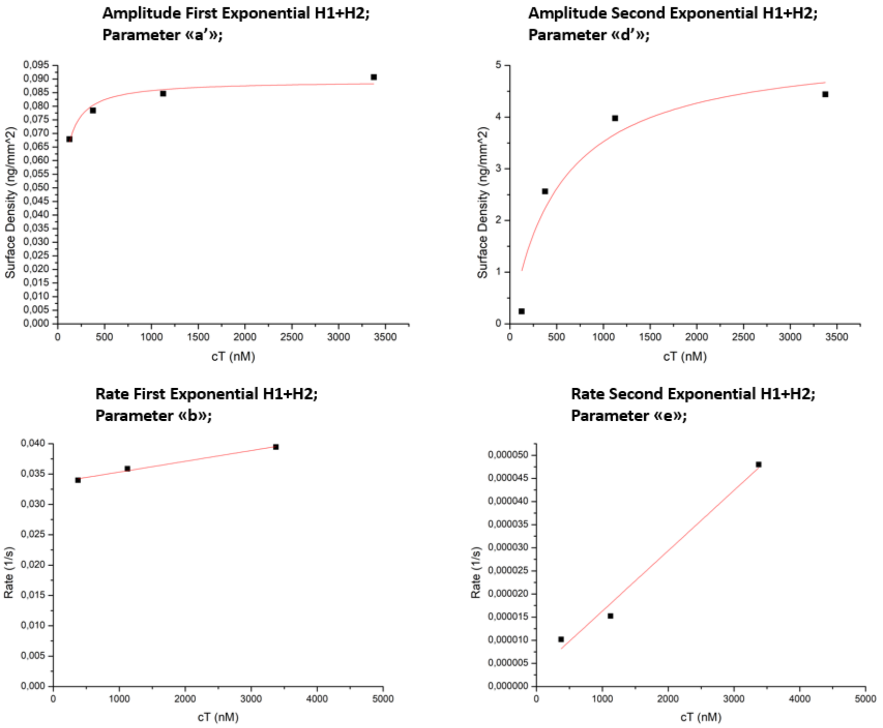

Figure 3.27: H1+H2 equilibrium and kinetics: Top row, equilibrium fits for Exp1 (left) and Exp2 (right). Red lines are Langmuir fits, Equation 3.26. Bottom row, kinetic fits from Equation 3.27 are shown as red lines.

Equation 3.25 suggests binding with two different rates k_1 and k_2, in fact, extracting fitting parameters reveals a large discrepancy between these two rates, indicating two different processes, slow and fast one. Furthermore, besides two different rates, we also distinguish two different amplitudes, A_1 and A_2, these parameters also differ by order of magnitude. Indeed, for each binding strand we can clearly distinguish two radically different processes. In each type of injection we can recognize two reactions with small saturation amplitudes, this indicates that each two exponential fit can be interpreted in means of conformational transition, i.e. of two exponential fits, one is associated with hairpin binding and second with hairpin opening. Furthermore, for H1, negative k_{on} is an artifact of binding rate decreasing with concentration (negative slope in Figure 3.25. Equilibrium and kinetics values are reported in Table 3.6.

Exponential	K_d/nM	$k_{on}/10^{-4}s^{-1}$	k_{off}/s^{-1}	$\Sigma_\infty/ngmm^{-2}$
H1-Exp1	26	-9e-4	0.2	0.03
H1-Exp2	17	3e-5	8e-4	0.2
H1+H2-Exp1	42	0.03	2e-6	0.09
H1+H2-Exp2	533	3e-6	1e-8	5.4

Table 3.6: Kinetic and equilibrium values for H1 and H1+H2 bindings. Both processes occur with similar affinity. Negative k_{on} for Exp1 is an artifact due to binding rate decreasing with target concentration.

Confocal microscopy

We also performed confocal microscopy investigation of post HCR surface. Each hairpin was conjugated with a fluorophore and HCR was performed on three different spotting concentrations, 2.5, 5 and 10 µM. Control was achieved by comparing with monolayer spots at same concentration but conatining just trigger + H1 strands. Figure 3.28 shows the mages obtained from fluorescence confocal microscope.

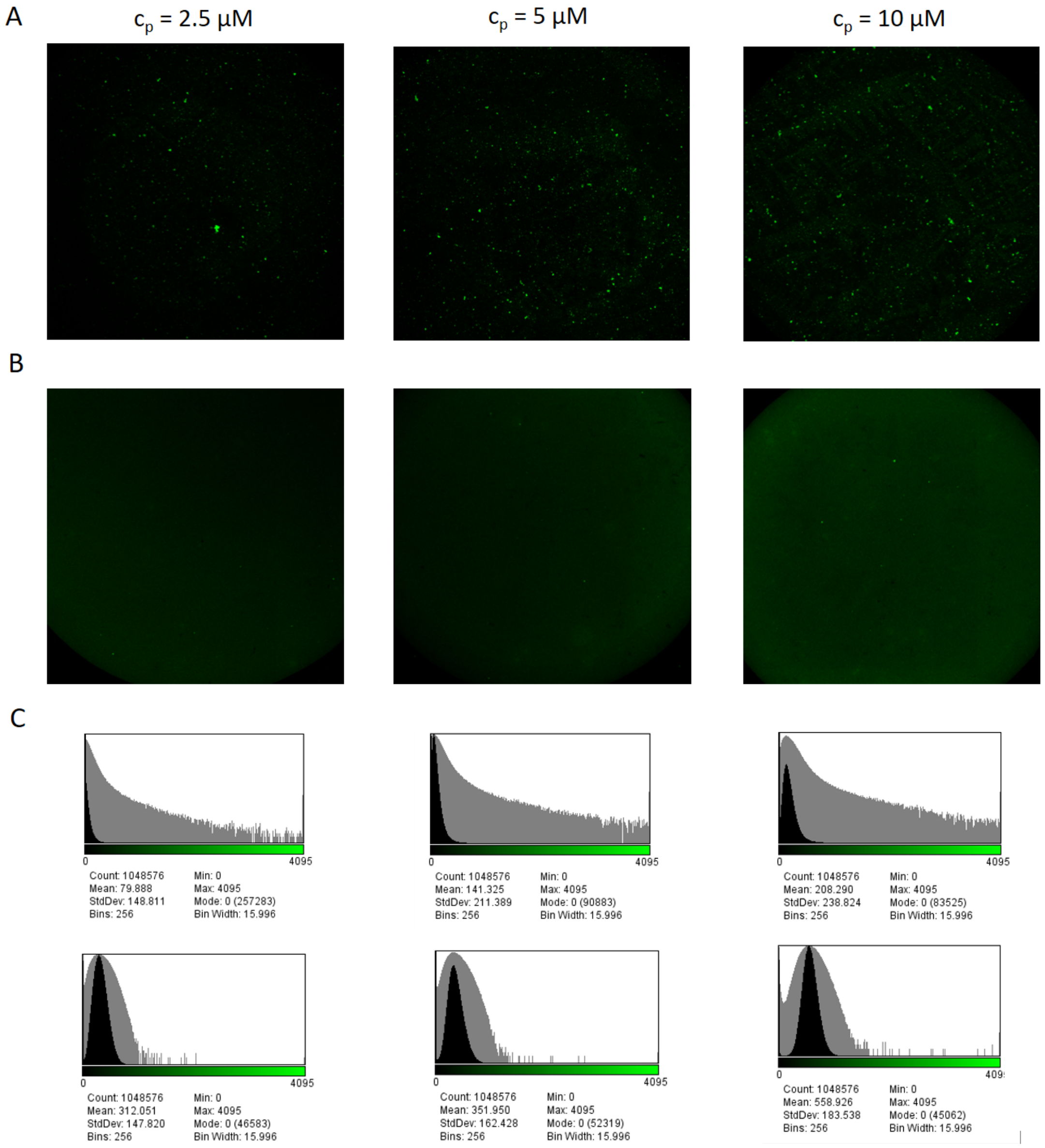

```
Count: 1048576    Min: 0
Mean: 79.888      Max: 4095
StdDev: 148.811   Mode: 0 (257283)
Bins: 256         Bin Width: 15.996

Count: 1048576    Min: 0
Mean: 141.325     Max: 4095
StdDev: 211.389   Mode: 0 (90883)
Bins: 256         Bin Width: 15.996

Count: 1048576    Min: 0
Mean: 208.290     Max: 4095
StdDev: 238.824   Mode: 0 (83525)
Bins: 256         Bin Width: 15.996

Count: 1048576    Min: 0
Mean: 312.051     Max: 4095
StdDev: 147.820   Mode: 0 (46583)
Bins: 256         Bin Width: 15.996

Count: 1048576    Min: 0
Mean: 351.950     Max: 4095
StdDev: 162.428   Mode: 0 (52319)
Bins: 256         Bin Width: 15.996

Count: 1048576    Min: 0
Mean: 558.926     Max: 4095
StdDev: 183.538   Mode: 0 (45062)
Bins: 256         Bin Width: 15.996
```

Figure 3.28: A — post HCR surfaces, each H1 was conjugated with fluorophore, bright dots indicates HCR filaments. Density of filaments, as indicated by number of bright dots per image, seems to correlate with probe density. B — Reference spots, dye conjugated H1 was hybridized to spotted trigger strands, without the presence of H2 - HCR cannot continue, i.e. H1 monolayer is formed on the spot, as indicated by uniform intensity throughout the image. C — Intensity histogram of images in A and B.

List of sequences

Strand	*Sequence*
*Hairpin*1	*GGAATTGGGAGTAAGGGCTGTGATGCCCTTACTCCC*
*Hairpin*2	*GCCCTTACTCCCAATTCCGGGAGTAAGGGCATCACA*
Trigger	*GCCCTTACTCCCAATTCC*

3.2.2 Binding of DNA nanostructures

In all previous experiments, DNA probes were randomly distributed on the sensing area, as there is no way to control the exact coordinates for the attachment of aminated DNA on functionalized surface. DNA origami, on the other hand, allows sub-nm control of probe position. It is however necessary beforehand to immobilize DNA origami nanostructure on the functionalized surface. We designed DNA origami with functionalized staples which enable binding on the DNA grafted surface via the sticky end interaction, i.e. hybridization. This approach to DNA origami immobilization provides additional control of orientation of the strucutre, unlike binding on mica for example via the formation of salt-bridges, we imagined to utilize sticky ends to control the orientation. Imagine a conman flipping a rigged coin, with asymmetric center of mass, it will always land on same side. We used up to 6 sticky ends to *"rig"* the origami, 3.29.

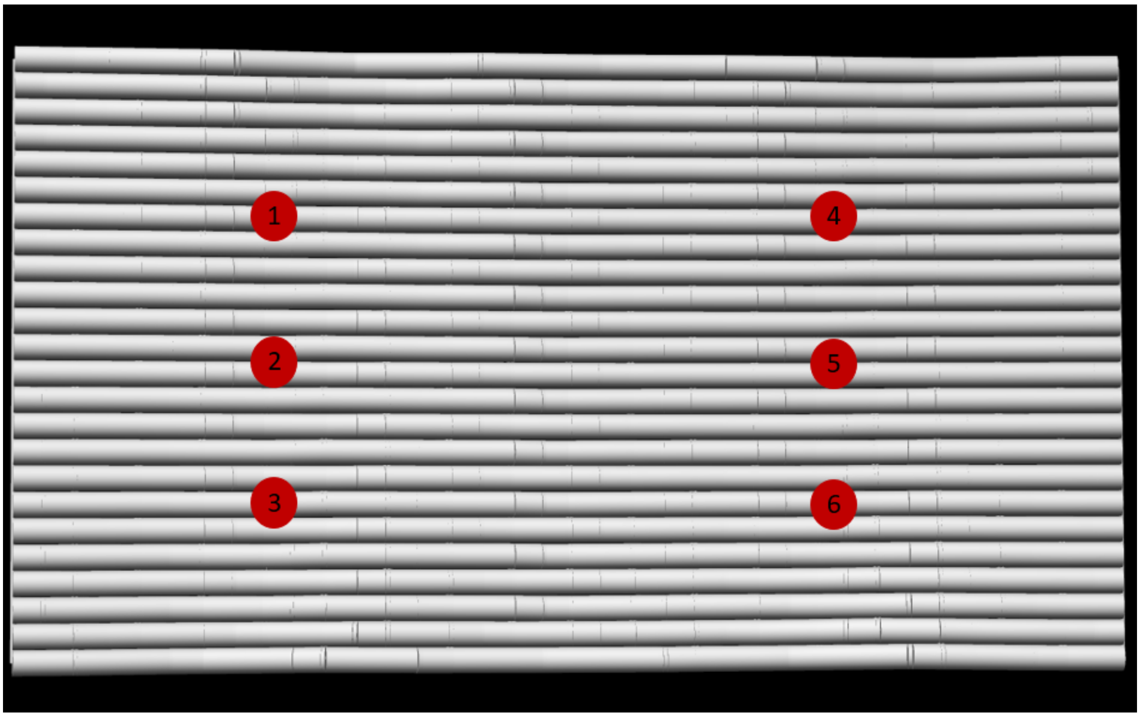

Figure 3.29: CanDo [42] model of DNA origami. Red circles are rough positions of extended staples, i.e. tether positions. Each tether is names with number for easier reading.

Dry AFM images of folded DNA origami, without tethers, are shown in Figure 3.30. Structures showed strong tendency towards stacking induced dimerization, i.e. no passivation.

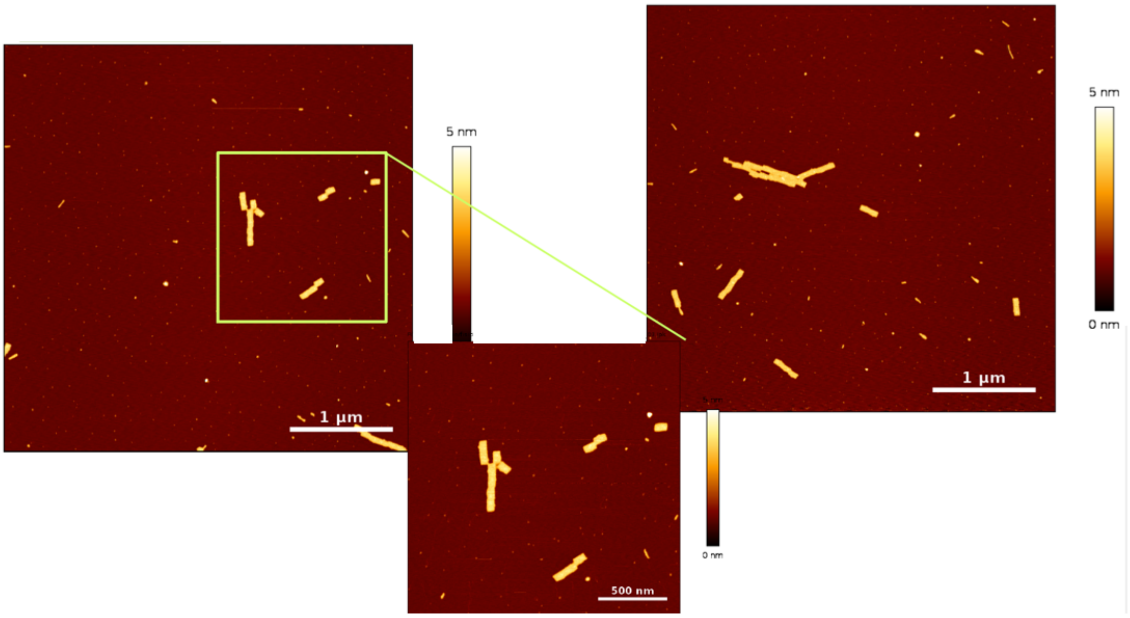

Figure 3.30: Images of DNA origami taken with atomic force microscope. DNA origami was immobilized on mica and imaged in dry conditions. Stacking interactions promote dimer formation, i.e. structures are not passivated.

We studied the binding of such origami structures varying number of tethers, namely 2, 4 and 6 tethers. In order to control any possible noise induced by difference in sequence dependent kinetics, all tethers were designed with same sequence, and just extended from staple strands on 3' end, Chapter 2. DNA origami was injected at increasing concentration, starting from 3 pM and reaching final concentration of 2 nM. Figure 3.31 shows the binding response of origami structures with 2 tetheres, at positions 2-5 (green curve); 4 tethers, at positions 1-3-4-6 (red curve), and binding response of 6 strand tethered DNA origami (blue).

Binding curves indicate that there is some relationship between binding strength and number of tethers. This can be intuitively understood from binding probability related to tether-probe distance, i.e. once the origami is bound with one leg, other legs within 1 origami-distance from the surface, this makes the probability of detachment lower — assuming that for detachment all tethers must be in non-hybridized state with the surface probes. Furthermore, the tethers are 40bp long, yielding in quite strong hybridization. Even though the system is clearly not saturated in both cases, final concentration reached is 2 nM, which is quite low for objects of this size. Indeed, this prevented us from analyzing this binding events with the Langmuir model and reaching higher concentrations could propose a future difficulty due to the relatively high volume required by the sensor. However, some analysis was carried out on the final injection for all three types of structure and assuming that maximum possible surface density does not depend on the number of tethers, but on the number of probes, which was kept constant for all three origami structures. Binding of 2 tethered structure was unreliable up to last injection. Last injection however produced some positive signal from which the saturation amplitude was estimated to be around 0.06ng/mm^2, almost a 7x increase was observed on the origami structure with 4 tethers with a final amplitude of 6.7ng/mm^2, and finally

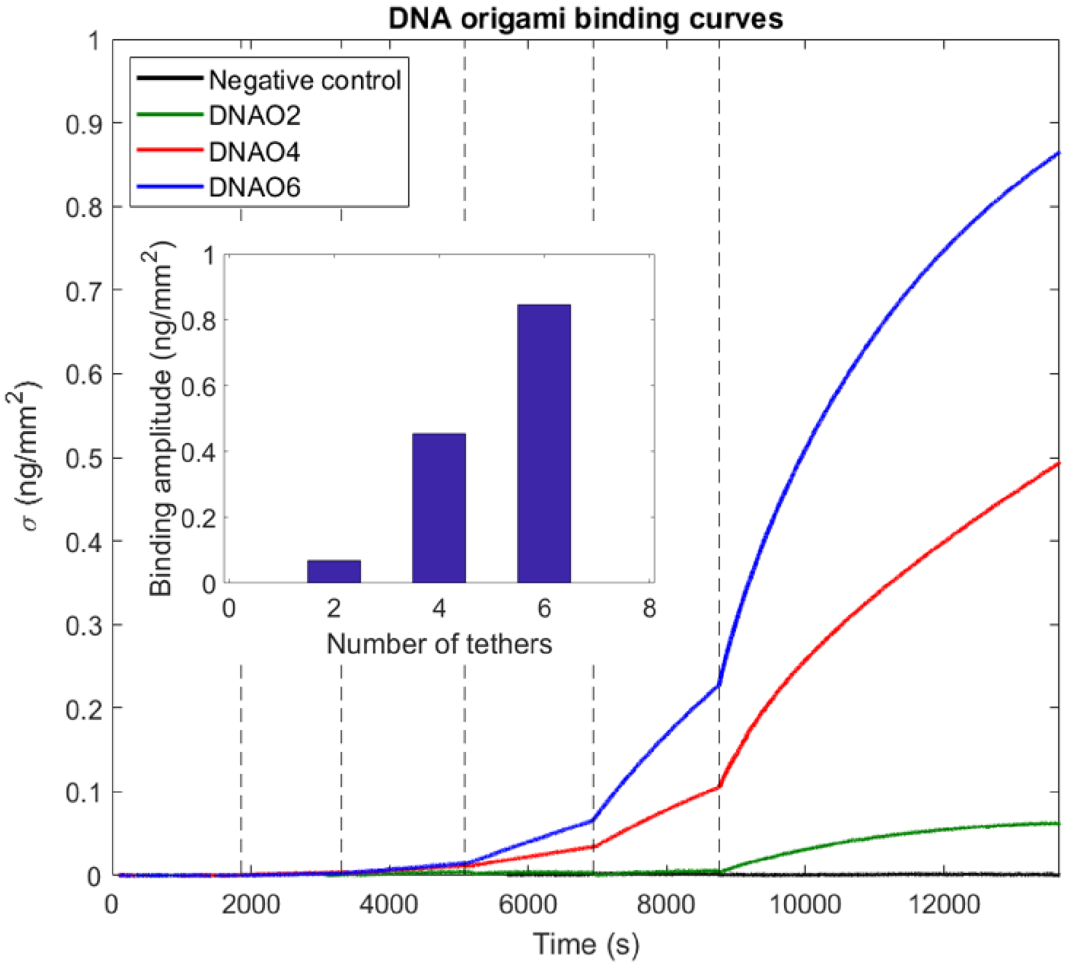

Figure 3.31: Binding curves for DNA origami with different number of tethers at injected concentrations: 3 pM, 16 pM, 0.08 nM, 0.4 nM and 2 nM. 2-legged DNA origami (green) — below 2 nM we observed virtually no binding event; 4-legged DNA origami surface binding is shown in red and 6-legged DNA origami binding in blue. Black line represents spots with non-interacting sequence grafted, and dashed lines represent each injection. Inset — Final surface densities, estimated from exponential growth fits to last injection for all three binding curves, correlate positively with number of tethers.

0.85ng/mm^2 was measured for full tethered origami structure. This correlation between number of tethers and measured amplitude at equal concentration suggests an increase of binding affinity with number of tethers attached. Considering we are well below the K_D values, i.e. within the linear part of the Langmuir isotherm. Since we assumed that the saturation amplitude is constant for all three origami structures, in this regime K_D scales with equilibrium surface density, $\sigma_s at$, estimated from exponential growths, thus, comparison of amplitudes provides some insight into the relative relationships of affinities across all structures. In other words, 6-tethered origami structures have 2x greater affinity then 4-tethered origamis and 12x higher affinity then 2-tethered origamis (Figure 3.31 inset. Estimation of kinetics was also hampered by the lack of real plateauing in the binding curve, thus we relied on the initial slope of each injection for the origami types that allowed such analysis across multiple injected concentrations, namely 4 and 6-tethered structures. Initial slopes of signal growth due to the adsorbtion immediately post injection are related to association kinetics as:

$$\sigma_{eq}\Gamma = k_{on}c_{origami} \tag{3.28}$$

where initial slope $= \sigma_{eq}\Gamma$ is the product of the plateau value and characteristic rate from exponential growth fits, k_{on} is the association rate and c_t is the injected origami concentration. Results plotted in Figure 3.32 suggest that the binding rate of DNA origami is independent on the number of sticky ends adhered to each origami, i.e. k_{on} for both of these structures is the same, and equals $7 \cdot 10^{-4}\text{nM}^{-1}\text{s}^{-1}$. Same binding rate was also assumed for 2-tethered DNA origami structures, which allowed the direct comparison of estimated dissociation rates k_{off} for all three designed structures, based on the observed rate Γ in the last injection.

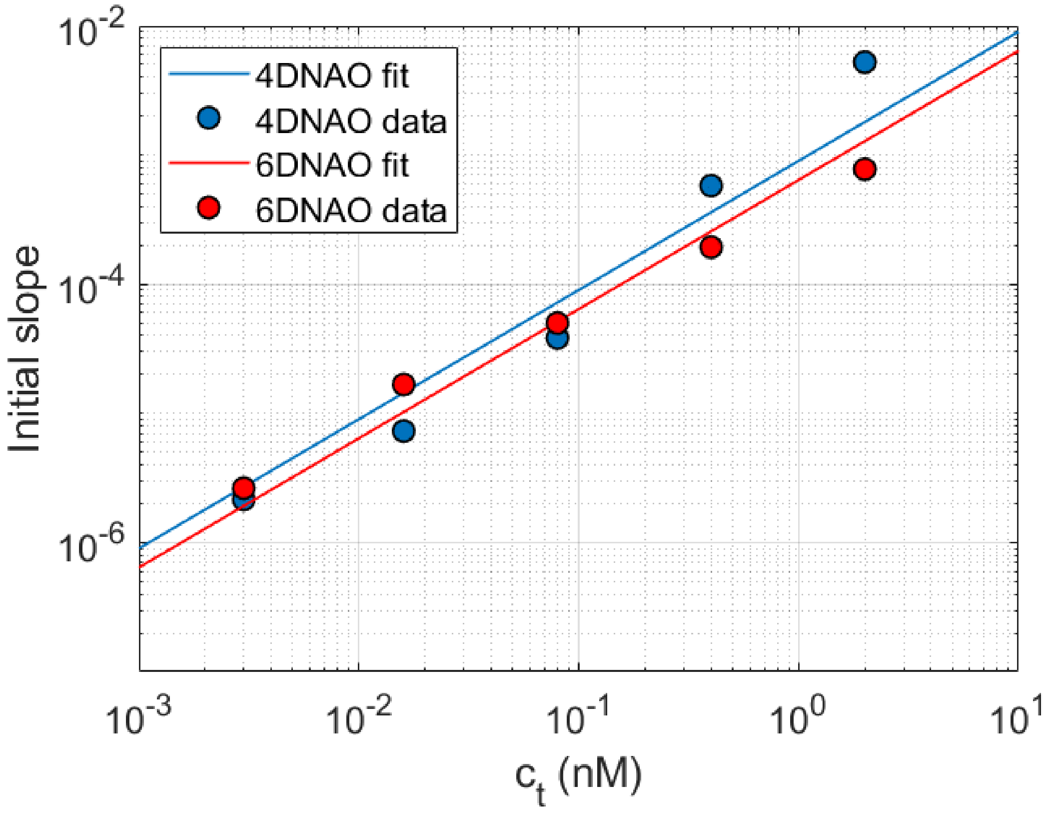

Figure 3.32: Initial slopes fitted with $k_{on}c_{origami}$ to estimate the kinetics of binding for both origami types. Blue points are correspond to blue lines and represent the 4-legged origami structure, likewise, red points and red line represent 6-legged origami structure. $k_{on} = 7 \cdot 10^{-4} nMs^{-1}$.

Chapter 4

Conclusions and future perspectives

Throughout this thesis, DNA was shown to be successfully used as sensing probe for detection of various molecules, from other DNA molecules, to miRNA and proteins both directly and indirectly. Moreover, surface bound DNA was used as a catalyst for functional DNA based device in hybridization chain reaction and it's potential in designing and manipulating large DNA based nanostructures was shown. Some of the reported investigations are already published [44], some are accepted for publication - miRNA assay, and some are in reviewing process, protein-DNA nested well model. Studies on more complex DNA structures are still in different stages of research. The following chapter will address the future work on the research lines addressed in this thesis.

Beyond oligo DNA hybridization and NLER model

In chapter 3.1 I presented our paper on DNA hybridization in which we were able to develop a simple model based on electrostatic interactions between DNA molecules, and used it to interpret DNA microarray data. Furthermore we showed that kinetics of DNA hybridization on a surface is always slower than the same process in solution. However, it can be somewhat regulated by monovalent salt concentration and grafting substrates, i.e. gel versus solid support and presence of stacking interaction.. We investigated hybridization on 12 and 23 bp long probes with and without 11 bp long ds support, where in the presence of ds support, stacking-enhanced stability effectively "locks" the target sequence to the probe, greatly increasing affinity. Indeed, despite the fact that hybridizaton kinetics is poorly understood in general, controlling kinetics of surface tethered DNA hybridization, could in future be crucial for example to development of surface bound autonomous DNA nanodevices. For those purpose specifically, it would be worth exploring the kinetics of surface bound DNA hybridization in the presence of divalent salts and DNA stabilizing buffers present for example in DNA origami. In fact, we showed how stacking interactions on side can significantly affect the dissociation, however, introducing stacking on both sides could stabilize the target strand even further. Additionaly, hairpin structures could find their role in DNA microarrays. Our study was restricted to only two lengths of DNA probes, 11 and 23 bp. Future experiments could try to formulate sequence length dependent DNA hybridization kinetics, bringing DNA hybridization kinetics closer to automated design.

miRNA assay in biological sample

We showed how DNA probe can be at the foundation of rapid, multiplex assay with ultra-low sensitivity. Through careful assay optimization from our simple numeric model, we pushed the sensitivity of this assay to sub-pM values. In addition to this, the model qualitatively explained the decrease of signal following the incubation of both antibodies. In principle, introduction of Ab2 to the cuvette, with Ab1 present, introduces two new competing reactions, Ab pairs in solution and on surface, this effectively reduces the effective concentration of Ab1 resulting in new relaxation process and detachment of Ab1 from surface — thus decrease of signal is observed. This regime is however bypassed when assay is optimized for amplification factor as the optimization is driven by maximum readout signal. Post optimization sensitivity was 0.5 pM miRNA biomarker, and 35x amplification. However, the theoretical maximum amplification factor, obtained with longer incubation time, is about 150. Real miRNA containing samples are often messy, and contain a plethora of different proteins and enzymes that can degrade the probe and inhibit the hybridization. It would be critical therefore to demonstrate the assay functionality in real biological sample, and in general, how the sensitivity and specificity change when more competition is introduced. In addition, the assay model only qualitatively explained the decrease in readout signal, it would be useful for future optimizations to be able to predict and manipulate the decrease, and possibly utilize this decreasing transition as marker in different applications.

Hybridization Chain Reaction

Hybridization Chain Reaction was monitored in real time, and spots were additionally inspected with fluorescence confocal microscopy. We confirmed the growth of HCR filaments, and modelled the kinetics as a two-step model, where in first step, a hairpin is bound to the grafted trigger with it's overhang, this facilitates the second step where hairpin is slowly unzipping until it is completely hybridized to the grafted trigger. Complete model is still missing however, we observed an unintuitive decrease of binding rate with hairpin concentrations for first exponential. From confocal images we see a clear exponential intensity distribution, considering that every hairpin-1 carried a fluorophore, it is safe to assume that dot intensity is in some correlation with the number of hairpin-1 present - this could be used to determine filament size distribution. Even though the amplification potential of HCR is quite high, eliminating this barrier would further enhance this potential. Going even higher in complexity scale, incubating more than two different hairpins could provide a possibility to generate nanoscale aptamer webs with bacteria (or virus) trapping potential.

Surface bound DNA origami

DNA origami was shown to bind on DNA functionalized surface via the sticky-end interaction, DNA hybridization in essence. We showed the binding of origami structures functionalized with 4 and 6 tethers, while 2 tethers were also discussed. In fact, the original design was intended to host up to 6 tethers. In future experiments, we plan to study the binding with 1,3 and 5 tethers in addition to 4 and 6. Preliminary results shown in Chapter 3 are quite encouraging and provide solid support for the continuation of the project. This preliminary study should serve in the future experiments on DNA origami. In fact, our origami design has holders for four additional extensions protruding on the opposite side of the structure. Intention is to use origami as a bind-and-release platform with nanometer-scale control for nanoparticles. Origami can be used to design array of probes equally distanced, in contrast to random distribution currently achieved on DNA microarrays. This offers a plethora of possibilities from designing even more complex structures on the surface, and also as tracks for autonomous or non-autonomous DNA nanomachines.

Figure 4.1: Smile emoji produced with DNA origami [6].

Appendices

Appendix A

DNA origami sequences

Coordinates	*Sequence*
23[192]22[208]	*TTATTTACATTGGCAGATTCACCAGAACGAAC*
22[175]20[176]	*TCAGTATTCAGCAGCAAATGAAAAAACGTTAT*
7[32]9[31]	*AGATTCATTTCATTGAATCCCCCTGACCATAA*
23[256]22[272]	*GAGATAGAACCCTTCTGACCTGAATGAATGGC*
22[239]20[240]	*AAAACATCATATCTGGTCAGTTGGTGAGGATT*
18[47]16[48]	*GTAACGCCGCATCTGCCAGTTTGACGGATTCT*
22[47]20[48]	*GACTCCAAACCAGCGAGACGGGCAGTGCCAGC*
10[79]8[80]	*GGTCATTGCAAAGCGGATTGCAAATGTTTA*
23[8]22[16]	*ATGGCCCACTACGTGAACCGTCTA*
10[15]8[16]	*TAAATATGTTCAGAAAACGAGAATCAAATGCT*
10[143]9[159]	*GACCGGAAATTCGAGCTTCAAAGAATAAGAA*
3[192]5[191]	*TTGACAGGCTCAGAGCCGCCACCCCCATTACC*
23[224]22[240]	*GACCAGTAATAAAAGGGACATTCTATAGCCCT*
9[224]11[223]	*CAGGGAAGTACCAACGCTAACGAAAGCAAA*
10[111]8[112]	*GAGAGTACGAAGCCCGAAAGACTTAAAAGAAG*
20[15]18[16]	*GGCGGTTTCGGCCAGTGCCAAGCTCGACGTTG*
0[175]0[144]	*TACAAACTACAACGCCTGTAGCATTCCACAG*
17[160]18[144]	*GCAGAGGCTTGAATACCAAGTTACCCATTCA*
10[239]8[240]	*CTGAATCTCGCATTAGACGGGAGAAGAAACAA*
9[256]11[255]	*AACACCCTTTTGCACCCAGCTACAATTCTAAG*
19[96]21[95]	*TTTCCTGTTTAATTGCGTTGCGCTAGAGAGTT*
7[128]9[127]	*ATAACCCTAGCGAGAGGCTTTTGCCAAATATC*
7[288]9[287]	*TTTATTTTTCAGAGAGATAACCCATAATTGAG*
20[239]18[240]	*TAGAAGTAATCAATATAATCCTGATCAGGTTT*
0[79]1[63]	*TTTTCTGTATGGGGTTTTGCTAAAGGCTCCA*
5[32]7[31]	*CGCATAGGAAGAAAAATCTACGTTAGGTAGAA*
0[239]1[223]	*CATTTTCAGGGATAGCAAGCCCACAGGCGG*
21[192]23[191]	*CATCACCTGAAGATAAAACAGAGGGAAATGGA*
17[192]19[191]	*GCAAAAGAGGGAGAAACAATAACGGGAGCGGA*
5[256]7[255]	*AGAATCAACAGCGCTAAAGACAAAGGCAACAT*
3[128]5[127]	*TGACCCCCAACGGAGATTTGTATCCAGTGAAT*
7[192]9[191]	*AAGACTCCAAAAGTAAGCAGATAGATGAAAAT*
2[47]0[48]	*ACAGCATCAAATCTCCAAAAAAAAACAACTTT*

Coordinates	*Sequence*
17[288]19[287]	*AATCAATATCAAAATTATTAGCACAATTGAAC*
1[256]3[255]	*AGCCCGGAACAGGAGTGTACTGGTGATCTTCA*
15[32]17[31]	*CCCGGTTGACAAACGGCGGATTGAGGCGCATC*
2[143]1[159]	*AACCATCGTAGTTGCGCCGACAAAAAGTATT*
12[143]11[159]	*AAGGTGGCTTCATTTGGGGCGCGACTCATCG*
13[256]15[255]	*TGTCCAGAAAATAAGAATAAACACTCAAATAT*
11[256]13[255]	*AACGCGAGCCTGAACAAGAAAAATAGTAATTC*
4[239]2[240]	*AAAATCACTATTCACAAACGAATGAATAAGTT*
2[111]0[112]	*TCGCTGAGCGAGGTGAATTTCTTAATCTAAAG*
4[175]2[176]	*GCCACCCTCCACCACCAGAGCCGCGCCTATTT*
15[160]16[144]	*TAACCTCCCATAGGTCTGAGAGACTTTAACC*
17[32]19[31]	*GTAACCGTAGGGTTTTCCCAGTCATGCATGCC*
6[79]4[80]	*TTTTAAGAGAACCGGATATTCACTGCTCCA*
18[15]16[16]	*TAAAACGATACGTTGGTGTAGATGCCGTAATG*
22[111]20[112]	*TAGCCCGACGGTCCACGCTGGTTTAGTGAGCT*
14[271]12[272]	*AAGGCGTTCGACGACAATAAACAATCAACAAT*
3[224]5[223]	*GGCCTTGACGGAACCAGAGCCACAATGAAA*
20[175]18[176]	*TAATTTTAAAAGAAACCACCAGAAGATTCGCC*
19[128]21[127]	*TCCACACACCTGGGGTGCCTAATGGCCCCAGC*
0[47]1[31]	*CAACAGTTTCAGCGGAGTGAGAATAATTTTTT*
7[160]8[144]	*ATAACGGAGAAGGAAACCGAGGAAGATAAAA*
11[64]13[63]	*TGCGAACGAGCAAAATTAAGCAATAAATTTTT*
13[192]15[191]	*GCAGAGGCTACAAATTCTTACCAGTATAACTA*
1[128]3[127]	*GATACCGACCCACGCATAACCGATCTCATCTT*
6[207]4[208]	*TTGACGGAGGCCGGAAACGTCACCCACCGGAA*
14[79]12[80]	*TCTACAACATATATTTTAAATGGCAAGGCA*
5[96]7[95]	*ATCAACGTATCATTGTGAATTACCGCCAAAAG*
16[15]14[16]	*GGATAGGTAACTAGCATGTCAATCTGAACGGT*
8[239]6[240]	*TGAAATAGATACATACATAAAGGTAGGGCGAC*
23[32]22[48]	*CCAAATCAAGTTTTTTGGGGTCGAAGAACGTG*
2[271]0[272]	*TTGATGATATAGGTGTATCACCGTCCGCCACC*
8[111]6[112]	*TTTTGCCAAGGCATAGTAAGAGCATTTAATTT*
19[192]21[191]	*ATTATCATTTAAATCCTTTGCCCGATCTAAAG*
14[239]12[240]	*TAATTACTTACCGACAAAAGGTAAAATATCCC*
0[207]1[191]	*CCATGTACCGTAACACTGAGTTTCAGGATTAG*
16[79]14[80]	*AATGTGAGTATAAGCAAATATTTTGAGAGA*
6[271]4[272]	*TGGTTTACGTTTGCCTTTAGCGTCTCATAGCC*
5[192]7[191]	*ATTAGCAAAATTATTCATTAAAGGGCATGATT*
20[207]18[208]	*AACTCGTACATATTCCTGATTATCCAGTACCT*
19[64]21[63]	*GAGCTCGAAGTCGGGAAACCTGTCACAGCTGA*
3[32]5[31]	*GAAGTTTCAGGGAACCGAACTGACAGACCAGG*
9[160]10[144]	*ACGATTTTTATTTATCCCAATCCACGAACCA*
17[64]19[63]	*CGACCGTATGTGCTGCAAGGCGATCGGGTACC*
15[96]17[95]	*AAACGTTATGTAGCCAGCTTTCATTCGCACTC*

Coordinates	*Sequence*
19[256]21[255]	ATTATACTCAATAGATAATACATTCAAATCAA
11[128]13[127]	GCTATATTATCAATTCTACTAATAAAAGGGTG
21[256]23[255]	CAGTAGAATTTAATGCGCGAACTGGGCCAACA
11[96]13[95]	ATACATTTCCAATAAATCATACAGCAATGCCT
12[271]10[272]	AGATAAGTGCGTTTTAGCGAACCTCAAGATTA
0[271]1[255]	CTCAGAACCGCCACCCTCAGAGCCATAAGTAT
21[160]22[144]	CTGAGAGCAACACCGCCTGCAACAGGTTCCG
1[160]2[144]	AAGAGGCTATTATTCTGAAACATGTGACAAC
10[271]8[272]	GTTGCTATGAACAAAGTCAGAGGGCAAGAATT
5[64]7[63]	TCTTGACAAACTGGCTCATTATACATACCACA
21[64]23[63]	TTGCCCTTAAGAGTCCACTATTAAGGTGCCGT
11[192]13[191]	GGAATCATGCTGTCTTTCCTTATCTAATTTAG
21[96]23[95]	GCAGCAAGGATAGGGTTGAGTGTTAGGGAGCC
12[111]10[112]	ATTAACATCGCAAATGGTCAATAACAGGATTA
8[207]6[208]	TTTTTAAGTTATTACGCAGTATGTGGTAAATA
2[207]0[208]	CCGTATAAGGGTTTTGCTCAGTACATAGGAAC
16[47]14[48]	CCGTGGGAATAATCAGAAAAGCCCGCCTGAGA
22[15]20[16]	TCAGGGCGGCGTATTGGGCGCCAGCGGGGAGA
2[175]0[176]	CGGAACCTGAGACTCCTCAAGAGAGTCACCAG
10[47]8[48]	TGCTGAATTCAGGTCTTTACCCTGGGAATCGT
22[79]20[80]	TTGGAACCACCGCCTGGCCCTGCACTGCCC
22[143]21[159]	AAATCGGCATCCTGTTTGATGGTGTGCCACG
18[79]16[80]	AGGGGGATCGGCCTCAGGAAGACAACATTA
1[32]3[31]	CACGTTGAGGAACGAGGGTAGCAATTCATGAG
12[47]10[48]	AGAGCATACATGTAACAGTTGATTAGCTTAAT
21[32]23[31]	TTCTTTTCCGTCAAAGGGCGAAAAACCATCAC
16[271]14[272]	TGTAAATCTAATTTCATCTTCTGATGATAAAT
15[288]17[287]	TAATGGTTTATGTGAGTGAATAACAGTACATA
14[47]12[48]	GTCTGGAGTTCAACGCAAGGATAAAAAGCCTC
6[175]4[176]	CACCGTCAAAAATCACCAGTAGCATCAGAACC
16[207]14[208]	TTAAGACGTGCTGATGCAAATCCAAGTATCAT
6[47]4[48]	ACGTTGGGCTGGCTGACCTTCATCCAGACGGT
8[143]7[159]	ACCAAAATCGTTTACCAGACGACACGCAATA
13[128]15[127]	AGAAAGGCATTCAACCGTTCTAGCCGCGTTAA
13[160]14[144]	GCCATATTAACAGTAGGGCTTAATCACCATC
1[64]3[63]	AAAGGAGCGATCGTCACCCTCAGCTACGTAAT
5[128]7[127]	AAGGCTTGATTGGGCTTGAGATGGACACTATC
15[224]17[223]	GACAAAGATGAAAACATAGCGATATCAAGA
17[128]19[127]	GAAACCAGAACTGTTGGGAAGGGCCTCACAAT
3[64]5[63]	GCCACTACTAGCCGGAACGAGGCGAAGAGTAA
4[271]2[272]	CCCTTATTAGAATGGAAAGCGCAGCATGGCTT
4[143]3[159]	CAAAGTACAGCGATTATACCAAGAGAGCCGC
20[47]18[48]	TGCATTAAGACTCTAGAGGATCCCTAAGTTGG
14[143]13[159]	AATATGATCGGAGACAGTCAAATTGAGAATC

Coordinates	*Sequence*
21[288]23[295]	*ATATCTTTGCACAGACAATATTTTAGCGTAAGAATACGTG*
7[96]9[95]	*GAATTACGGAGGGGGTAATAGTAATCAAAAAG*
16[143]15[159]	*AATAGGAATAAATCAGCTCATTTTACCTTTT*
1[288]3[287]	*GGTTTAGTTCCAGTAAGCGTCATATCTCTGAA*
9[32]11[31]	*ATCAAAAACTGGTGCTGTAGCTCATCTGGAAG*
19[224]21[223]	*GGCAATTCTTAGACTTTACAAACTCAAACC*
2[79]0[80]	*TTTGCGGCTTTAATTGTATCGGTAAATGAA*
8[15]6[16]	*TTAAACAGGGAACAACATTATTACAATAAAAC*
18[207]16[208]	*TTTACATCAGATGATGAAACAAACAGCTTAGA*
6[111]4[112]	*CAACTTTAAACAAAGCTGCTCATTATCGCCTG*
3[256]5[255]	*TTAAAGCCAGCGTTTGCCATCTTTGTAGCGAC*
0[295]1[287]	*ACCGCCACCCTCAGAAACTCAGGA*
20[271]18[272]	*AGAGCCGTTCTGAATTATGGAAGGGTAAAACA*
18[143]17[159]	*GGCTGCGCGCAAAGCGCCATTCGAAAATCGC*
23[96]22[112]	*CCCGATTTAGAGCTTGACGGGGAACAAAAGAA*
11[160]12[144]	*AGAACAAGTTAAACCAAGTACCGCAGCTGAA*
10[207]8[208]	*CCAGAGCCTTACAGAGAGAATAACCGAAGCCC*
0[143]1[127]	*ACAACCCTCATAGTTAGCGTAACGAACAGCTT*
10[175]8[176]	*AGCCATATTTGTTTAACGTCAAAACCGAACAA*
7[256]9[255]	*ATAAAAGACCCAATAATAAGAGCAATTAACTG*
5[288]7[287]	*GCGCGTTTGTCACAATCAATAGAAGGAATAAG*
4[47]2[48]	*CAATCATACATTAAACGGGTAAAAAGCGAAAG*
4[15]2[16]	*AAAGAGGAGAGGACTAAAGACTTTCGGCTACA*
2[15]0[8]	*GAGGCTTTAGGAATTGCGAATAATAGAAAGGAACAACTAA*
16[175]14[176]	*ATCAAAATGGCTTAGGTTGGGTTATATAAAGC*
3[160]4[144]	*CACCAGAACAGAGCCACCACCCTCCGCGAAA*
7[224]9[223]	*CGTAGAAACAATAGCTATCTTACATAAAAA*
22[207]20[208]	*CACCAGCATGCTGAACCTCAAATAAATTCGAC*
6[15]4[16]	*GAACTAACCAGATGAACGGTGTACCAACTTTG*
18[239]16[240]	*AACGTCAGTTAATTACATTTAACATTTCCCTT*
12[239]10[240]	*ATCCTAATAGAAGGCTTATCCGGTATTTTATC*
5[160]6[144]	*GAGCCAGCCCGACTTGAGCCATTTCAGAACG*
8[47]6[48]	*CATAAATACAGTTGAGATTTAGGACAGTCAGG*
13[288]15[287]	*GCTAATGCTGAAATACCGACCGTGCCTAAATT*
14[207]12[208]	*ATGCGTTAATTTTCGAGCCAGTAAAACCAATC*
17[224]19[223]	*AAACAAAAATGAATATACAGTAAAGATGAT*
20[111]18[112]	*AACTCACAGTGAAATTGTTATCCGGATCGGTG*
6[239]4[240]	*ATTCAACCAGCAGCACCGTAATCATCATAATC*
15[192]17[191]	*TATGTAAACTGAGAAGAGTCAATATTACCTGA*
13[32]15[31]	*GCCTTTATCAAACAAGAGAATCGAATATGTAC*
1[224]3[223]	*ATAAGTGCGTCAGTGCCTTGAGTGACGATT*
12[175]10[176]	*AACGGGTACAAGCCGTTTTTATTTAAATAAAC*
9[288]11[287]	*CGCTAATATTTTGAAGCCTTAAATCCCGACTT*

Coordinates	*Sequence*
12[15]10[16]	*CATTATGACAACTAAAGTACGGTGACATGTTT*
8[79]6[80]	*GACTGGAATGCAGATACATAACTTATGCGA*
9[96]11[95]	*ATTAAGAGCTTTAATTGCTCCTTTACCATTAG*
17[96]19[95]	*CAGCCAGCTTCGCTATTACGCCAGCATAGCTG*
3[96]5[95]	*GAGGCGAATGTCGAAATCCGCGACTTACCCAA*
18[175]16[176]	*TGATTGCTGAATTATTCATTTCAAGTGAATTT*
23[128]23[159]	*AACGTGGCGAGAAAGGAAGGGAAGGAAATAC*
1[192]3[191]	*GATTAGCGACAGTTAATGCCCCCTCGCCAGCA*
9[192]11[191]	*AGCAGCCTTAATTTGCCAGTTACATCATCGTA*
22[271]20[272]	*TATTAGTCAGGAATTGAGGAAGGTAATAGATT*
8[175]6[176]	*AGTTACCAATACCCAAAAGAACTGTGAATTAT*
11[224]13[223]	*TCAGATATTTACGAGCATGTAGATAAGAGA*
23[64]22[80]	*AAAGCACTAAATCGGAACCCTAAGTTCCAGT*
14[175]12[176]	*CAACGCTCTAACAACGCCAACATGATTCCAAG*
6[143]5[159]	*AGTAGTAACCCTGACGAGAACACGGGAATTA*
14[111]12[112]	*TAATGCCGTGTAGGTAAAGATTCAGTAGTAGC*
21[128]23[127]	*AGGCGAAAAAAATCCCTTATAAATAGCCGGCG*
15[256]17[255]	*ATTTTAGTGTCGCTATTAATTAATATTTCATT*
13[96]15[95]	*GAGTAATGGAGAGGGTAGCTATTTTAAATTGT*
15[64]17[63]	*GGAAGATTGCGAGTAACAACCCGTGGGGACGA*
12[207]10[208]	*AATAATCGTACCGCGCCCAATAGCGCGTCTTT*
19[160]20[144]	*TGCGGAACAAAGTTTGAGTAACATGCATAAA*
23[160]22[176]	*CTACATTTTGACGCTCAATCGTCTTGAGGCGG*
2[239]0[240]	*TTAACGGGCGTCGAGAGGGTTGATACCACCCT*
18[271]16[272]	*GAAATAAACTTTTTTAATGGAAACCTTGCTTC*
21[224]23[223]	*CTCAATCAGCCATTAAAAATACCGTCACAC*
0[111]1[95]	*TTTTGTCGTCTTTCCAGACGTTAGTTTATCAG*
4[111]2[112]	*ATAAATTGAGAATACACTAAAACAATATTCGG*
20[79]18[80]	*GCTTTCCATTCGTAATCATGGTCTGGCGAA*
3[288]5[287]	*TTTACCGTTCATCGGCATTTTCGGAGACTGTA*
17[256]19[255]	*TGAATTACGAAATTGCGTAGATTTTTGTTTGG*
11[32]13[31]	*TTTCATTCAAGCTAAATCGGTTGTCGGGAGAA*
13[224]15[223]	*ATATAAAGAGAAAAAGCCTGTTTATCGCAA*
19[32]21[31]	*TGCAGGTCTGAATCGGCCAACGCGGGTGGTTT*
8[271]6[272]	*GAGTTAAGAACGCAAAGACACCACAATTCATA*
11[288]13[287]	*GCGGGAGGAGAACGCGCCTGTTTACATGTTCA*
15[128]17[127]	*ATTTTTGTCGCCATCAAAAATAATTGGTGCCG*
18[111]16[112]	*CGGGCCTCTTTCCGGCACCGCTTCTCGCGTCT*
12[79]10[80]	*AAGAATTAGTAGATTTAGTTTGTGATAAGA*
16[239]14[240]	*AGAATCCTACGCGAGAAAACTTTTCGGAATCA*
4[207]2[208]	*CCGCCTCCAGGTTGAGGCAGGTCAAACAGTGC*
4[79]2[80]	*TGTTACTGAAGGCACCAACCTAAGGCCGCT*
9[128]11[127]	*GCGTTTTAGCAAACTCCAACAGGTCCTGTTTA*

Coordinates	*Sequence*
9[64]11[63]	*AGTCAGAATTTGCGGATGGCTTAGCCCAATTC*
13[64]15[63]	*AGAACCCTAGGCTATCAGGTCATTCAAAAACA*
19[288]21[287]	*CAACCATAAGGTGCACTAACAACTTATCTAAA*
14[15]12[16]	*AATCGTAACCCTGTAATACTTTTGACCAAAAA*
5[224]7[223]	*CCATCGATGATTGAGGGAGGGAATAGCAAA*
20[143]19[159]	*GTGTAAAGACATACGAGCCGGAATATCATTT*
1[96]3[95]	*CTTGCTTTGCTTGCAGGGAGTTAAAAACGAAA*
7[64]9[63]	*TTCAACTATAGCGTCCAATACTGCACTATTAT*
16[111]14[112]	*GGCCTTCCATATTTTGTTAAAATTTGATAAAT*

Bibliography

[1] J. D. WATSON and F. H. C. CRICK, "Molecular structure of nucleic acids: A structure for deoxyribose nucleic acid," *Nature*, vol. 171, pp. 737–738, Apr 1953.

[2] T. Brown, *Genomes 2nd edition*. United Kingdom: BIOS Scientific Publishers Ltd, 2002.

[3] R. E. Franklin and R. G. Gosling, "The structure of sodium thymonucleate fibres. I. The influence of water content," *Acta Crystallographica*, vol. 6, pp. 673–677, Sep 1953.

[4] N. C. Seeman, "Nucleic acid junctions and lattices," *Journal of Theoretical Biology*, vol. 99, no. 2, pp. 237 – 247, 1982.

[5] W. Wang, L. M. Nocka, B. Z. Wiemann, D. M. Hinckley, I. Mukerji, and F. W. Starr, "Holliday junction thermodynamics and structure: Coarse-grained simulations and experiments," *Scientific Reports*, vol. 6, p. 22863, Mar 2016.

[6] P. W. K. Rothemund, "Folding dna to create nanoscale shapes and patterns," *Nature*, vol. 440, pp. 297–302, Mar 2006.

[7] B. Saccà and C. M. Niemeyer, "Dna origami: The art of folding dna," *Angewandte Chemie International Edition*, vol. 51, no. 1, pp. 58–66, 2012.

[8] C. Mao, W. Sun, Z. Shen, and N. C. Seeman, "A nanomechanical device based on the b–z transition of dna," *Nature*, vol. 397, pp. 144–146, Jan 1999.

[9] J. N. Zadeh, C. D. Steenberg, J. S. Bois, B. R. Wolfe, M. B. Pierce, A. R. Khan, R. M. Dirks, and N. A. Pierce, "Nupack: Analysis and design of nucleic acid systems," *Journal of Computational Chemistry*, vol. 32, no. 1, pp. 170–173, 2011.

[10] S. J. Green, D. Lubrich, and A. J. Turberfield, "Dna hairpins: fuel for autonomous dna devices," *Biophysical journal*, vol. 91, pp. 2966–2975, Oct 2006. 16861269[pmid].

[11] R. M. Dirks and N. A. Pierce, "Triggered amplification by hybridization chain reaction," *Proceedings of the National Academy of Sciences*, vol. 101, no. 43, pp. 15275–15278, 2004.

[12] F. M. Spiga, A. Bonyár, B. Ring, M. Onofri, A. Vinelli, H. Sántha, C. Guiducci, and G. Zuccheri, "Hybridization chain reaction performed on a metal surface as a means of signal amplification in spr and electrochemical biosensors," *Biosensors and Bioelectronics*, vol. 54, pp. 102 – 108, 2014.

[13] A. Eshra, S. Shah, T. Song, and J. Reif, "Renewable dna hairpin-based logic circuits," *IEEE Transactions on Nanotechnology*, vol. 18, pp. 252–259, 2019.

[14] H. Lee, A. K. R. Lytton-Jean, Y. Chen, K. T. Love, A. I. Park, E. D. Karagiannis, A. Sehgal, W. Querbes, C. S. Zurenko, M. Jayaraman, C. G. Peng, K. Charisse, A. Borodovsky, M. Manoharan, J. S. Donahoe, J. Truelove, M. Nahrendorf, R. Langer, and D. G. Anderson, "Molecularly self-assembled nucleic acid nanoparticles for targeted in vivo sirna delivery," *Nature Nanotechnology*, vol. 7, pp. 389–393, Jun 2012.

[15] H. de Puig, A. Cifuentes Rius, D. Flemister, S. H. Baxamusa, and K. Hamad-Schifferli, "Selective light-triggered release of dna from gold nanorods switches blood clotting on and off," *PLOS ONE*, vol. 8, pp. 1–6, 07 2013.

[16] B. Yurke, A. J. Turberfield, A. P. Mills, F. C. Simmel, and J. L. Neumann, "A dna-fuelled molecular machine made of dna," *Nature*, vol. 406, pp. 605–608, Aug 2000.

[17] R. Carlson, "Time for new dna synthesis and sequencing cost curves," 2014.

[18] J. P. Gergen, R. H. Stern, and P. C. Wensink, "Filter replicas and permanent collections of recombinant dna plasmids," *Nucleic acids research*, vol. 7, pp. 2115–2136, Dec 1979. 118435[pmid].

[19] G. K. Geiss, R. E. Bumgarner, B. Birditt, T. Dahl, N. Dowidar, D. L. Dunaway, H. P. Fell, S. Ferree, R. D. George, T. Grogan, J. J. James, M. Maysuria, J. D. Mitton, P. Oliveri, J. L. Osborn, T. Peng, A. L. Ratcliffe, P. J. Webster, E. H. Davidson, L. Hood, and K. Dimitrov, "Direct multiplexed measurement of gene expression with color-coded probe pairs," *Nature Biotechnology*, vol. 26, pp. 317–325, Mar 2008.

[20] M. Schena, R. A. Heller, T. P. Theriault, K. Konrad, E. Lachenmeier, and R. W. Davis, "Microarrays: biotechnology's discovery platform for functional genomics," *Trends in Biotechnology*, vol. 16, pp. 301–306, Jul 1998.

[21] M. L. Bulyk, P. L. F. Johnson, and G. M. Church, "Nucleotides of transcription factor binding sites exert interdependent effects on the binding affinities of transcription factors," *Nucleic Acids Research*, vol. 30, pp. 1255–1261, 03 2002.

[22] M. F. Berger, A. A. Philippakis, A. M. Qureshi, F. S. He, P. W. Estep, and M. L. Bulyk, "Compact, universal dna microarrays to comprehensively determine transcription-factor binding site specificities," *Nature Biotechnology*, vol. 24, pp. 1429–1435, Nov 2006.

[23] V. Grimm, S. Ezaki, M. Susa, C. Knabbe, R. D. Schmid, and T. T. Bachmann, "Use of dna microarrays for rapid genotyping of tem beta-lactamases that confer resistance," *Journal of Clinical Microbiology*, vol. 42, no. 8, pp. 3766–3774, 2004.

[24] G. C. Kennedy, H. Matsuzaki, S. Dong, W.-m. Liu, J. Huang, G. Liu, X. Su, M. Cao, W. Chen, J. Zhang, W. Liu, G. Yang, X. Di, T. Ryder, Z. He, U. Surti, M. S. Phillips, M. T. Boyce-Jacino, S. P. Fodor, and K. W. Jones, "Large-scale

genotyping of complex dna," *Nature Biotechnology*, vol. 21, pp. 1233–1237, Oct 2003.

[25] G. Nava, E. Ceccarello, F. Giavazzi, M. Salina, F. Damin, M. Chiari, M. Buscaglia, T. Bellini, and G. Zanchetta, "Label-free detection of dna single-base mismatches using a simple reflectance-based optical technique," *Phys. Chem. Chem. Phys.*, vol. 18, pp. 13395–13402, 2016.

[26] J. Li, S. Chen, and D. H. Evans, "Typing and subtyping influenza virus using dna microarrays and multiplex reverse transcriptase pcr," *Journal of Clinical Microbiology*, vol. 39, no. 2, pp. 696–704, 2001.

[27] N. Kessler, O. Ferraris, K. Palmer, W. Marsh, and A. Steel, "Use of the dna flow-thru chip, a three-dimensional biochip, for typing and subtyping of influenza viruses," *Journal of Clinical Microbiology*, vol. 42, no. 5, pp. 2173–2185, 2004.

[28] K. Qamhieh and B. M. Pettitt, "Controlling microarray dna hybridization efficiency by probe-surface distance and external surface electrostatics," *AIP Conference Proceedings*, vol. 1653, no. 1, p. 020090, 2015.

[29] A. W. Peterson, R. J. Heaton, and R. M. Georgiadis, "The effect of surface probe density on dna hybridization," *Nucleic acids research*, vol. 29, pp. 5163–5168, Dec 2001. 11812850[pmid].

[30] D. S. Dandy, P. Wu, and D. W. Grainger, "Array feature size influences nucleic acid surface capture in dna microarrays," *Proceedings of the National Academy of Sciences*, vol. 104, no. 20, pp. 8223–8228, 2007.

[31] A. Vainrub and B. M. Pettitt, "Coulomb blockage of hybridization in two-dimensional dna arrays," *Phys. Rev. E*, vol. 66, p. 041905, Oct 2002.

[32] A. Halperin, A. Buhot, and E. B. Zhulina, "Sensitivity, specificity, and the hybridization isotherms of dna chips," *Biophysical journal*, vol. 86, pp. 718–730, Feb 2004. 14747310[pmid].

[33] I. Langmuir, "The Adsorption of Gases on Plane Surfaces of Glass, Mica and Pt," Nov. 1917.

[34] A. Halperin, A. Buhot, and E. B. Zhulina, "On the hybridization isotherms of DNA microarrays: the langmuir model and its extensions," *Journal of Physics: Condensed Matter*, vol. 18, pp. S463–S490, apr 2006.

[35] Z. Guo, R. A. Guilfoyle, A. J. Thiel, R. Wang, and L. M. Smith, "Direct fluorescence analysis of genetic polymorphisms by hybridization with oligonucleotide arrays on glass supports," *Nucleic Acids Research*, vol. 22, pp. 5456–5465, 01 1994.

[36] M. I. Volkova-Gugeshashvili, A. G. Volkov, and V. S. Markin, "Adsorption at liquid interfaces: The generalized frumkin isotherm and interfacial structure," *Russian Journal of Electrochemistry*, vol. 42, pp. 1073–1078, Oct 2006.

[37] F. Giavazzi, M. Salina, R. Cerbino, M. Bassi, D. Prosperi, E. Ceccarello, F. Damin, L. Sola, M. Rusnati, M. Chiari, B. Chini, T. Bellini, and M. Buscaglia, "Multispot, label-free biodetection at a phantom plastic–water interface," *Proceedings of the National Academy of Sciences*, vol. 110, no. 23, pp. 9350–9355, 2013.

[38] M. Salina, F. Giavazzi, R. Lanfranco, E. Ceccarello, L. Sola, M. Chiari, B. Chini, R. Cerbino, T. Bellini, and M. Buscaglia, "Multi-spot, label-free immunoassay on reflectionless glass," *Biosensors and Bioelectronics*, vol. 74, pp. 539 – 545, 2015.

[39] J. Vörös, "The density and refractive index of adsorbing protein layers," *Biophysical Journal*, vol. 87, pp. 553–561, Jul 2004.

[40] S. M. Douglas, A. H. Marblestone, S. Teerapittayanon, A. Vazquez, G. M. Church, and W. M. Shih, "Rapid prototyping of 3D DNA-origami shapes with caDNAno," *Nucleic Acids Research*, vol. 37, pp. 5001–5006, 06 2009.

[41] M. A. B. Baker, A. J. Tuckwell, J. F. Berengut, J. Bath, F. Benn, A. P. Duff, A. E. Whitten, K. E. Dunn, R. M. Hynson, A. J. Turberfield, and L. K. Lee, "Dimensions and global twist of single-layer dna origami measured by small-angle x-ray scattering," *ACS Nano*, vol. 12, pp. 5791–5799, Jun 2018.

[42] D.-N. Kim, F. Kilchherr, H. Dietz, and M. Bathe, "Quantitative prediction of 3D solution shape and flexibility of nucleic acid nanostructures," *Nucleic Acids Research*, vol. 40, pp. 2862–2868, 12 2011.

[43] E. Stahl, T. G. Martin, F. Praetorius, and H. Dietz, "Facile and scalable preparation of pure and dense dna origami solutions," *Angewandte Chemie (International ed. in English)*, vol. 53, pp. 12735–12740, Nov 2014. 25346175[pmid].

[44] L. Vanjur, T. Carzaniga, L. Casiraghi, M. Chiari, G. Zanchetta, and M. Buscaglia, "Non-langmuir kinetics of dna surface hybridization," *Biophysical Journal*, vol. 119, no. 5, pp. 989 – 1001, 2020.

[45] R. Bumgarner, "Overview of dna microarrays: Types, applications, and their future," *Current Protocols in Molecular Biology*, vol. 101, no. 1, pp. 22.1.1–22.1.11, 2013.

[46] N. C. Seeman, *DNA Nanotechnology: From the Pub to Information-Based Chemistry*, pp. 1–9. New York, NY: Springer New York, 2018.

[47] A. Relógio, C. Schwager, A. Richter, W. Ansorge, and J. Valcárcel, "Optimization of oligonucleotide-based dna microarrays," *Nucleic acids research*, vol. 30, pp. e51–e51, Jun 2002. 12034852[pmid].

[48] A. S. S. Vasan, "Point-of-care biosensor system," *Frontiers in Bioscience*, vol. S5, no. 1, pp. 39–71, 2013.

[49] G. Zanchetta, R. Lanfranco, F. Giavazzi, T. Bellini, and M. Buscaglia, "Emerging applications of label-free optical biosensors," *Nanophotonics*, vol. 6, no. 4, pp. 627 – 645, 01 Jul. 2017.

[50] J. Chao, D. Zhu, Y. Zhang, L. Wang, and C. Fan, “DNA nanotechnology-enabled biosensors,” *Biosensors and Bioelectronics*, vol. 76, pp. 68–79, Feb. 2016.

[51] G. Oliviero, S. Federici, P. Colombi, and P. Bergese, “On the difference of equilibrium constants of DNA hybridization in bulk solution and at the solid-solution interface,” *Journal of Molecular Recognition*, vol. 24, pp. 182–187, Feb. 2011.

[52] W. Qiao, H.-C. Chiang, H. Xie, and R. Levicky, “Surface vs. solution hybridization: effects of salt, temperature, and probe type,” *Chemical Communications*, vol. 51, no. 97, pp. 17245–17248, 2015.

[53] A. Vainrub and B. M. Pettitt, “Accurate prediction of binding thermodynamics for DNA on surfaces,” *The Journal of Physical Chemistry B*, vol. 115, pp. 13300–13303, Nov. 2011.

[54] D. Irving, P. Gong, and R. Levicky, “DNA surface hybridization: Comparison of theory and experiment,” *The Journal of Physical Chemistry B*, vol. 114, pp. 7631–7640, June 2010.

[55] P. Gong and R. Levicky, “DNA surface hybridization regimes,” *Proceedings of the National Academy of Sciences*, vol. 105, pp. 5301–5306, Apr. 2008.

[56] D. Erickson, D. Li, and U. J. Krull, “Modeling of DNA hybridization kinetics for spatially resolved biochips,” *Analytical Biochemistry*, vol. 317, pp. 186–200, June 2003.

[57] Y. Gao, “Secondary structure effects on DNA hybridization kinetics: a solution versus surface comparison,” *Nucleic Acids Research*, vol. 34, pp. 3370–3377, June 2006.

[58] I. Y. Wong and N. A. Melosh, “An electrostatic model for DNA surface hybridization,” *Biophysical Journal*, vol. 98, pp. 2954–2963, June 2010.

[59] J. Zhang, Y. An, A. Borrion, W. He, N. Wang, Y. Chen, and G. Li, “Process characteristics for microwave assisted hydrothermal carbonization of cellulose,” *Bioresource Technology*, vol. 259, pp. 91–98, July 2018.

[60] A. W. Peterson, L. K. Wolf, and R. M. Georgiadis, “Hybridization of mismatched or partially matched DNA at surfaces,” *Journal of the American Chemical Society*, vol. 124, pp. 14601–14607, Dec. 2002.

[61] A. W. Peterson, R. J. Heaton, and R. Georgiadis, “Kinetic control of hybridization in surface immobilized DNA monolayer films,” *Journal of the American Chemical Society*, vol. 122, pp. 7837–7838, Aug. 2000.

[62] T. E. Ouldridge, P. Šulc, F. Romano, J. P. K. Doye, and A. A. Louis, “DNA hybridization kinetics: zippering, internal displacement and sequence dependence,” *Nucleic Acids Research*, vol. 41, pp. 8886–8895, Aug. 2013.

[63] R. WANG, “Immobilisation of DNA probes for the development of SPR-based sensing,” *Biosensors and Bioelectronics*, vol. 20, pp. 967–974, Nov. 2004.

[64] Z. Li, Y. Chen, X. Li, T. I. Kamins, K. Nauka, and R. S. Williams, "Sequence-specific label-free DNA sensors based on silicon nanowires," *Nano Letters*, vol. 4, pp. 245–247, Feb. 2004.

[65] A. Star, E. Tu, J. Niemann, J.-C. P. Gabriel, C. S. Joiner, and C. Valcke, "Label-free detection of DNA hybridization using carbon nanotube network field-effect transistors," *Proceedings of the National Academy of Sciences*, vol. 103, pp. 921–926, Jan. 2006.

[66] R. McKendry, J. Zhang, Y. Arntz, T. Strunz, M. Hegner, H. P. Lang, M. K. Baller, U. Certa, E. Meyer, H.-J. Guntherodt, and C. Gerber, "Multiple label-free biodetection and quantitative DNA-binding assays on a nanomechanical cantilever array," *Proceedings of the National Academy of Sciences*, vol. 99, pp. 9783–9788, July 2002.

[67] M. Brucherseifer, M. Nagel, P. H. Bolivar, H. Kurz, A. Bosserhoff, and R. Büttner, "Label-free probing of the binding state of DNA by time-domain terahertz sensing," *Applied Physics Letters*, vol. 77, pp. 4049–4051, Dec. 2000.

[68] M. Cretich, G. Pirri, F. Damin, I. Solinas, and M. Chiari, "A new polymeric coating for protein microarrays," *Analytical biochemistry*, vol. 332, p. 67—74, September 2004.

[69] R. Karlsson and A. Fält, "Experimental design for kinetic analysis of protein-protein interactions with surface plasmon resonance biosensors," *Journal of Immunological Methods*, vol. 200, pp. 121–133, Jan. 1997.

[70] H. Zhao, I. I. Gorshkova, G. L. Fu, and P. Schuck, "A comparison of binding surfaces for SPR biosensing using an antibody–antigen system and affinity distribution analysis," *Methods*, vol. 59, pp. 328–335, Mar. 2013.

[71] M. F. Hagan and A. K. Chakraborty, "Hybridization dynamics of surface immobilized DNA," *The Journal of Chemical Physics*, vol. 120, pp. 4958–4968, Mar. 2004.

[72] M. F. Hagan and A. K. Chakraborty, "Hybridization dynamics of surface immobilized DNA," *The Journal of Chemical Physics*, vol. 120, pp. 4958–4968, Mar. 2004.

[73] J. SantaLucia and D. Hicks, "The thermodynamics of DNA structural motifs," *Annual Review of Biophysics and Biomolecular Structure*, vol. 33, pp. 415–440, June 2004.

[74] P. Yakovchuk, "Base-stacking and base-pairing contributions into thermal stability of the DNA double helix," *Nucleic Acids Research*, vol. 34, pp. 564–574, Jan. 2006.

[75] A. Vainrub and B. M. Pettitt, "Sensitive quantitative nucleic acid detection using oligonucleotide microarrays," *Journal of the American Chemical Society*, vol. 125, pp. 7798–7799, July 2003.

[76] R. Sips, "On the structure of a catalyst surface," *The Journal of Chemical Physics*, vol. 16, pp. 490–495, May 1948.

[77] I. I. Cisse, H. Kim, and T. Ha, "A rule of seven in watson-crick base-pairing of mismatched sequences," *Nature Structural & Molecular Biology*, vol. 19, pp. 623–627, May 2012.

[78] N. F. Dupuis, E. D. Holmstrom, and D. J. Nesbitt, "Single-molecule kinetics reveal cation-promoted DNA duplex formation through ordering of single-stranded helices," *Biophysical Journal*, vol. 105, pp. 756–766, Aug. 2013.

[79] P. Atkins and J. de Paula, *Atkins' Physical Chemistry*. OUP Oxford, 2010.

[80] A. Yalcin, F. Damin, E. Ozkumur, G. di Carlo, B. B. Goldberg, M. Chiari, and M. S. Unlu, "Direct observation of conformation of a polymeric coating with implications in microarray applications," *Analytical Chemistry*, vol. 81, pp. 625–630, Jan. 2009.

[81] M. Murphy, I. Rasnik, W. Cheng, T. M. Lohman, and T. Ha, "Probing single-stranded DNA conformational flexibility using fluorescence spectroscopy," *Biophysical Journal*, vol. 86, pp. 2530–2537, Apr. 2004.

[82] J. SantaLucia, "A unified view of polymer, dumbbell, and oligonucleotide DNA nearest-neighbor thermodynamics," *Proceedings of the National Academy of Sciences*, vol. 95, pp. 1460–1465, Feb. 1998.

[83] N. R. Markham and M. Zuker, "DINAMelt web server for nucleic acid melting prediction," *Nucleic Acids Research*, vol. 33, pp. W577–W581, July 2005.

[84] X. Zhang, G. G. Daaboul, P. S. Spuhler, P. Droge, and M. S. Unlu, "Quantitative characterization of conformational-specific protein–DNA binding using a dual-spectral interferometric imaging biosensor," *Nanoscale*, vol. 8, no. 10, pp. 5587–5598, 2016.

[85] B. L. Sprague, F. Muller, R. L. Pego, P. M. Bungay, D. A. Stavreva, and J. G. McNally, "Analysis of binding at a single spatially localized cluster of binding sites by fluorescence recovery after photobleaching," *Biophysical Journal*, vol. 91, pp. 1169–1191, Aug. 2006.

[86] A. Egatz-Gomez, C. Wang, F. Klacsmann, Z. Pan, S. Marczak, Y. Wang, G. Sun, S. Senapati, and H.-C. Chang, "Future microfluidic and nanofluidic modular platforms for nucleic acid liquid biopsy in precision medicine," *Biomicrofluidics*, vol. 10, pp. 032902–032902, May 2016. 27190565[pmid].

[87] C. E. Condrat, D. C. Thompson, M. G. Barbu, O. L. Bugnar, A. Boboc, D. Cretoiu, N. Suciu, S. M. Cretoiu, and S. C. Voinea, "mirnas as biomarkers in disease: Latest findings regarding their role in diagnosis and prognosis," *Cells*, vol. 9, p. 276, Jan 2020. 31979244[pmid].

[88] J. Alles, T. Fehlmann, U. Fischer, C. Backes, V. Galata, M. Minet, M. Hart, M. Abu-Halima, F. A. Grässer, H.-P. Lenhof, A. Keller, and E. Meese, "An estimate of the total number of true human miRNAs," *Nucleic Acids Research*, vol. 47, pp. 3353–3364, 03 2019.

[89] Y. Cheng, N. Tan, J. Yang, X. Liu, X. Cao, P. He, X. Dong, S. Qin, and C. Zhang, "A translational study of circulating cell-free microrna-1 in acute myocardial infarction," *Clinical science (London, England : 1979)*, vol. 119, pp. 87–95, Apr 2010. 20218970[pmid].

[90] J. E. Coats, Y. Lin, E. Rueter, I. Maher, L. James, and I. Rasnik, "Single-molecule FRET analysis of DNA binding and bending by yeast HMGB protein Nhp6A," *Nucleic Acids Research*, vol. 41, pp. 1372–1381, 12 2012.

[91] K. Zakrzewska and R. Lavery, "Towards a molecular view of transcriptional control," *Current opinion in structural biology*, vol. 22, p. 160—167, April 2012.

[92] M. Slutsky and L. A. Mirny, "Kinetics of protein-dna interaction: Facilitated target location in sequence-dependent potential," *Biophysical Journal*, vol. 87, no. 6, pp. 4021 – 4035, 2004.

[93] R. Marmorstein, M. Carey, M. Ptashne, and S. C. Harrison, "Dna recognition by gal4: structure of a protein-dna complex," *Nature*, vol. 356, pp. 408–414, Apr 1992.

[94] M. Hong, M. X. Fitzgerald, S. Harper, C. Luo, D. W. Speicher, and R. Marmorstein, "Structural basis for dimerization in dna recognition by gal4," *Structure (London, England : 1993)*, vol. 16, pp. 1019–1026, Jul 2008. 18611375[pmid].

[95] D. Evanko, "Hybridization chain reaction," *Nature Methods*, vol. 1, pp. 186–186, Dec 2004.